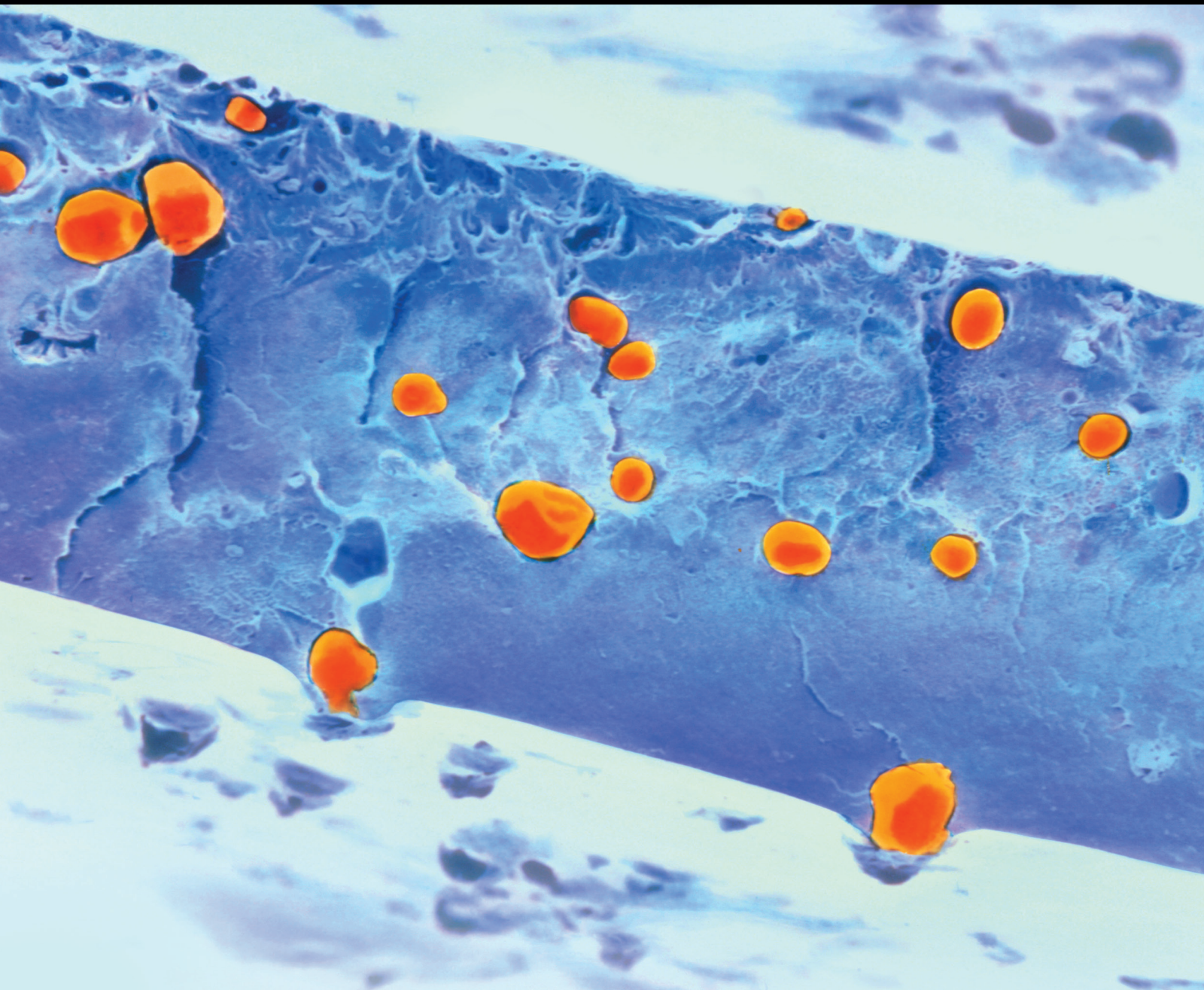


International Journal of Polymer Science

# Polymer-Based Construction Materials for Civil Engineering

Lead Guest Editor: Doo-Yeol Yoo

Guest Editors: Nemkumar Banthia, Rishi Gupta, Young Hoon Kim,  
and Amer Bhutta





---

# **Polymer-Based Construction Materials for Civil Engineering**

International Journal of Polymer Science

---

## **Polymer-Based Construction Materials for Civil Engineering**

Lead Guest Editor: Doo-Yeol Yoo

Guest Editors: Nemkumar Banthia, Rishi Gupta,  
Young Hoon Kim, and Aamer Bhutta



---

Copyright © 2019 Hindawi. All rights reserved.

This is a special issue published in "International Journal of Polymer Science." All articles are open access articles distributed under the Creative Commons Attribution License, which permits unrestricted use, distribution, and reproduction in any medium, provided the original work is properly cited.

## Editorial Board

Domenico Acierno, Italy

Luc Averous, France

Christopher Batich, USA

Marc Behl, Germany

Laurent Billon, France

Antonio Caggiano, Germany

Andrea Camposeo, Italy

Wen Shyang Chow, Malaysia

Angel Concheiro, Spain

Cedric Delattre, France

Yulin Deng, USA

Maria Laura Di Lorenzo, Italy

Eliane Espuche, France

Antonio Facchetti, USA

Gianluca M. Farinola, Italy

Marta Fernández-García, Spain

Peter Foot, UK

Benny Dean Freeman, USA

Peng He, USA

Jan-Chan Huang, USA

Wei Huang, China

Nabil Ibrahim, Egypt

Patric Jannasch, Sweden

Nobuhiro Kawatsuki, Japan

J.M. Kenny, Italy

Saad Khan, USA

Jui-Yang Lai, Taiwan

Ulrich Maschke, France

Subrata Mondal, India

Toribio F. Otero, Spain

Alessandro Pegoretti, Italy

Önder Pekcan, Turkey

Zhonghua Peng, USA

Victor H. Perez, Brazil

Debora Puglia, Italy

Miriam H. Rafailovich, USA

Arthur J. Ragauskas, USA

Anjanapura V. Raghu, India

Subramaniam Ramesh, Malaysia

Bernabé L. Rivas, Chile

Juan Rodriguez-Hernandez, Spain

Hossein Roghani-Mamaqani, Iran

Mehdi Salami-Kalajahi, Iran

Markus Schmid, Germany

Matthias Schnabelrauch, Germany

Shu Seki, Japan

Robert A. Shanks, Australia

Vito Speranza, Italy

Atsushi Sudo, Japan

Hideto Tsuji, Japan

Stefano Turri, Italy

Hiroshi Uyama, Japan

Cornelia Vasile, Romania

Alenka Vesel, Slovenia

De-Yi Wang, Spain

Qinglin Wu, USA

Huining Xiao, Canada

Yiqi Yang, USA

Michele Zappalorto, Italy

# Contents

## **Polymer-Based Construction Materials for Civil Engineering**

Doo-Yeol Yoo , Nemkumar Banthia , Rishi Gupta , Young Hoon Kim , and Aamer Bhutta  
Editorial (2 pages), Article ID 8914073, Volume 2019 (2019)

## **Experimental Investigation on Mechanical Properties of Hybrid Steel and Polyethylene Fiber-Reinforced No-Slump High-Strength Concrete**

Tian-Feng Yuan, Jin-Young Lee , Kyung-Hwan Min, and Young-Soo Yoon   
Research Article (11 pages), Article ID 4737384, Volume 2019 (2019)

## **Proposition of Thin-Layer Repairing Methods Using Low-Elasticity Polymer Portland Cement Materials and Glue and Study on the Fatigue Resistance of Reinforced Concrete Slab**

Tadashi Abe , Kiyoshi Ito, Noriyuki Kozakai, and Takayoshi Kodama  
Research Article (8 pages), Article ID 6545097, Volume 2018 (2019)

## **Crack Width and Load-Carrying Capacity of RC Elements Strengthened with FRP**

Justas Slaitas , Mykolas Daugevičius, Juozas Valivonis, and Tatjana Grigorjeva  
Research Article (14 pages), Article ID 6274287, Volume 2018 (2019)

## **Experimental and Numerical Study on the Compression Behavior of Square Concrete-Filled Steel Tube Stub Columns with Steel Fiber-Reinforced High-Strength Concrete**

Hyung-Suk Jung , Baek-Il Bae , Hyun-Ki Choi , Joo-Hong Chung, Chang-Sik Choi,  
and Yun-Cheul Choi   
Research Article (13 pages), Article ID 2385725, Volume 2018 (2019)

## **Flexural Assessment of Blast-Damaged RC Beams Retrofitted with CFRP Sheet and Steel Fiber**

Jin-Young Lee , Hyun-Oh Shin, Kyung-Hwan Min, and Young-Soo Yoon   
Research Article (9 pages), Article ID 2036436, Volume 2018 (2019)

## **Bond Behavior of Wet-Bonded Carbon Fiber-Reinforced Polymer-Concrete Interface Subjected to Moisture**

Yiyan Lu , Tao Zhu , Shan Li , and Zhenzhen Liu  
Research Article (11 pages), Article ID 3120545, Volume 2018 (2019)

## Editorial

# Polymer-Based Construction Materials for Civil Engineering

**Doo-Yeol Yoo** <sup>1</sup>, **Nemkumar Banthia** <sup>2</sup>, **Rishi Gupta** <sup>3</sup>, **Young Hoon Kim** <sup>4</sup>,  
**and Aamer Bhutta**<sup>2</sup>

<sup>1</sup>Department of Architectural Engineering, Hanyang University, 222 Wangsimni-ro, Seongdong-gu, Seoul 04763, Republic of Korea

<sup>2</sup>Department of Civil Engineering, The University of British Columbia, 6250 Applied Science Lane, Vancouver, BC, Canada V6T 1Z4

<sup>3</sup>Department of Civil Engineering, University of Victoria, 3800 Finnerty Road, Victoria, BC, Canada V8W 2Y2

<sup>4</sup>Department of Civil and Environmental Engineering, University of Louisville, Louisville, KY 40292, USA

Correspondence should be addressed to Doo-Yeol Yoo; [dyyoo@hanyang.ac.kr](mailto:dyyoo@hanyang.ac.kr)

Received 26 February 2019; Accepted 26 February 2019; Published 31 March 2019

Copyright © 2019 Doo-Yeol Yoo et al. This is an open access article distributed under the Creative Commons Attribution License, which permits unrestricted use, distribution, and reproduction in any medium, provided the original work is properly cited.

For several decades, numerous studies on the development of polymer-based construction materials for civil engineering applications have been conducted. In recent years, the polymer-based materials are mainly classified into three groups: (1) synthetic fiber-reinforced (cement) composites (FRC), (2) fiber-reinforced polymer (FRP), and (3) polymer concrete. The FRC includes several types of discontinuous fibers made of polypropylene, polyethylene, polyvinyl alcohol, polyester, and so on. It can be effectively adopted for civil structures and buildings to improve postcracking tensile performance, plastic shrinkage crack resistance, fire resistance (preventing spalling), and durability of concrete. In addition, several types of FRPs, that is, FRP reinforcing bar, FRP sheet, and sprayed FRP, have been studied for reinforcing and strengthening civil structures. In spite of their many advantages such as a noncorrosive nature, high specific strength, and electromagnetic neutrality, due to some drawbacks of FRPs, such as high brittleness, poor fire resistance, weak bond characteristics, and excessive creep, their wider practical applications have not occurred. Lastly, a polymer concrete has recently gained attention from engineers to achieve excellent mechanical properties and durability.

Several numbers of experimental and numerical papers addressed new research findings with regard to FRP strengthening systems. Y. Lu et al. investigated the effects of moisture on the initial and long-term bond behavior between a carbon fiber-reinforced polymer (CFRP) and a wet concrete with a water content of 4.73%. They found an important finding that the CFRP and concrete interface under moisture

condition increased during the first few months and then decreased or fluctuated over time in terms of the shear strength and slip capacity. The models suggested by the authors well predicted the interfacial fracture energy and ultimate load of specimens. J.-Y. Lee et al. evaluated the effects of CFRP sheet, steel fiber content, and amount of shear reinforcement on the blast resistance and residual flexural performance of blast-damaged reinforced concrete beams. Using small-diameter steel bars for stirrups with small spacing could decrease the local damages more effectively than the large-diameter steel reinforcement. CFRP retrofitting showed insignificant enhancement in ductility of damaged specimens, but it distributed the blast load and protected debris scattering. Steel fibers resulted in increased ductility and enhanced blast resistance against local damages. Therefore, it can be concluded that replacing a damaged concrete cover with steel fiber-reinforced cement composites is adequate for repairing the blast-damaged RC members. J. Slaitas et al. studied a prediction model of crack width and load-carrying capacity of RC beams strengthened with FRP, based on fracture mechanics of solids. Since, at the ultimate stage of crack propagation, the load-carrying capacity of the element is achieved, the load capacity could also be estimated according to the ultimate crack depth. Based on a comparison of experimental and numerical results, the proposed analytical crack model can be considered to be used for more precise predictions of flexural crack propagation and load-carrying capacity.

A novel polymer-based repairing system for RC structures has been developed by T. Abe et al. They particularly

adopted a novel polymer repairing system for enhancing fatigue resistance of RC slabs. In the repair method, two types of adhesives, i.e., a penetrable adhesive and a high-durability adhesive, were applied, and the fatigue resistance of repaired RC slabs was evaluated using wheel load running tests. The repair method proposed provided significantly better fatigue resistance than the conventional construction method, and this study thus proposed two wet repair cycles and one dry repair cycle with reinforcement measures to improve the load-bearing performance.

Discontinuous polymeric fibers were also considered for enhancing the mechanical properties of concrete by T.-F. Yuan et al. They investigated the effects of polyethylene (PE) and steel fibers on the compressive and flexural performance of no-slump high-strength concrete (HSC) and reported that the hybrid use of steel and short PE fibers in the no-slump HSC was most effective in improving the compressive and flexural strengths, energy absorption capacity, and fiber synergy.

Lastly, H.-S. Jung et al. have conducted experimental and numerical studies on evaluating the feasibility of using concrete-filled steel tube (CFT) columns from Korean Building Code (KBC2016). They adopted a high-strength steel with a yield strength of 800 MPa and a steel fiber-reinforced high-strength concrete and reported that due to the relatively large contribution of steel to strength, a filled concrete did not bring any significant changes of strength and strain. In addition, the maximum strain of a core concrete increased and became larger than that of the steel tube as 100 MPa concrete and steel fibers were used. The maximum permissible width-to-thickness ratio of CFT was found to decrease as the concrete strength increased and increased after steel fiber reinforcement.

We hope that readers of this special issue can obtain useful experimental and numerical results and discover recent research trends with regard to polymer-based construction materials for civil engineering. Hopefully, their academic curiosities and difficulties can also be solved by the valuable research results in this special issue.

## **Conflicts of Interest**

The editors declare that they have no conflicts of interest regarding the publication of this special issue.

## **Acknowledgments**

We would like to thank all authors who contributed to this special issue. This publication would not be possible without the participation of our expert reviewers, who provided vital constructive feedback and criticism throughout the review process.

*Doo-Yeol Yoo  
Nemkumar Banthia  
Rishi Gupta  
Young Hoon Kim  
Aamer Bhutta*

## Research Article

# Experimental Investigation on Mechanical Properties of Hybrid Steel and Polyethylene Fiber-Reinforced No-Slump High-Strength Concrete

Tian-Feng Yuan,<sup>1</sup> Jin-Young Lee ,<sup>2</sup> Kyung-Hwan Min,<sup>3</sup> and Young-Soo Yoon <sup>1</sup>

<sup>1</sup>School of Civil, Environmental and Architectural Engineering, Korea University, 145 Anam-ro, Seongbuk-gu, Seoul 02841, Republic of Korea

<sup>2</sup>Department of Civil Engineering and Applied Mechanics, McGill University, 817 Sherbrooke Street West, Montreal, Quebec, Canada H3A0C3

<sup>3</sup>Rail Research Institute, Chungnam National University, 99 Daehak-ro Yuseong-gu, Daejeon 34134, Republic of Korea

Correspondence should be addressed to Young-Soo Yoon; [ysyoon@korea.ac.kr](mailto:ysyoon@korea.ac.kr)

Received 4 April 2018; Accepted 29 January 2019; Published 20 March 2019

Guest Editor: Aamer Bhutta

Copyright © 2019 Tian-Feng Yuan et al. This is an open access article distributed under the Creative Commons Attribution License, which permits unrestricted use, distribution, and reproduction in any medium, provided the original work is properly cited.

This paper presents experimental investigations on the mechanical properties of no-slump high-strength concrete (NSHSC), such as the compressive and flexural strength. First, to determine the proper NSHSC mixtures, the compressive and flexural strength of three different water-to-binder ratios (w/b) of specimens with and without polyethylene (PE) fiber was tested at test ages. Then, the effect of hybrid combinations of PE fiber and steel fiber (SF) on the compressive strength, flexural strength, flexural toughness, and flexural energy dissipation capacity was experimentally investigated. Furthermore, the various hybrid fiber-reinforced NSHSCs were evaluated, and their synergy was calculated, after deriving the benefits from each of the individual fibers to exhibit a synergetic response. The test results indicate that a w/b of 16.8% with or without fibers had lower strength and flexural strength (toughness) than those of other mixtures (w/b of 16.4% and 17.2%). Specimens with a hybrid of SF and short PE fibers exhibited a higher compressive and flexural strength, flexural toughness, energy dissipation capacity, and fiber synergy in all considered instances.

## 1. Introduction

No-slump concrete, also known as zero-slump concrete, is defined as concrete with 0-25 mm slump by the American Concrete Institute (ACI 211.3) [1]. It is widely used for the production of paving blocks, masonry blocks, concrete slabs, and prestressed concrete (PC) elements. To achieve adequate internal cohesion of the granular matrix, the water-to-binder ratio (w/b) must be low [2, 3]. The inclusion of the properties of self-compacting concrete (SCC) in no-slump to create self-compacting no-slump concrete (SCNSC) has been widely researched [4]. There are cases of no-slump concrete fabricated and used in structures, such as a no-slump mixture used at Alpe Gere dam in Italy and at Manicougan-I in Canada with the aid of large internal vibrators mounted on backhoes or bulldozers [3, 5]. However, all of those

no-slump concrete mixtures are low or normal-strength concrete (20-60 MPa) and do not exceed 100 MPa of compressive strength. There has also been a lack of research on no-slump high-strength concrete with a compressive strength of over 120 MPa at 28 days.

The design method of no-slump high-strength concrete was based on that of ultra-high-performance cementitious materials, which have a very low water-to-binder ratio and can achieve good mechanical properties through controlling the packing density of the solid. However, cementitious composites are brittle, with a low tensile strength (flexural strength) and strain capacity. Hence, reinforcing concrete with randomly discontinuous fibers can improve ductility, toughness, and resistance to crack growth, and two or more types of fibers can be included to exploit their complementary and maximize the improvement [6]. Most of the

conventional fiber-reinforced cementitious materials involve the use of individual fiber types or hybrid single fiber types with different sizes. The individual fiber reinforcement method is effective in an only limited range of strain and crack opening and improved strength or ductility [7]. To improve strength and ductility, hybrid single fiber types with different sizes are generally used for ultra-high-performance cementitious materials [8, 9]. The hybrid fiber-reinforced composites have benefited from each of the individual fibers and exhibit a synergetic response. The various methods of hybridization include hybrids with different aspect ratios (lengths, diameters) and fiber types (tensile strength, modulus). The hybrid based on fiber aspect ratios results in a higher strength and improved fracture toughness of the composites, which control their microcracks and macrocracks, respectively. Hybrids based on fiber types use different properties of flexibility, in which a stiffer fiber provides the strength (first-crack strength, postcrack strength) and the other improves the toughness and strain capacity [10–14].

To date, there has been a lack of research on the combination of different fiber hybridizations in no-slump high-strength concrete. In this study, in order to filter out the effects on compressive strength, three different water-to-binder ratio (w/b) values with a fiber volume fraction of 0.0%, and 1.5% were fabricated and evaluated. In order to improve the tensile strength and strain capacity of NSHSC, the mixtures are hybrid polyethylene (PE) fibers and/or steel fibers (SF), and the compressive strength and flexural strength at test ages were evaluated. Additionally, the flexural toughness and the synergy of hybridization were evaluated. Therefore, this study is provided and used as a basic data to fiber-reinforced no-slump high-strength concrete.

## 2. Experimental Program

In this study, concrete with three values of water-to-binder ratios was prepared using no-slump high-strength concrete (NSHSC) hybrid polyethylene or/and steel fibers. The variable specimens were used with a fiber volume fraction of 0.0%, and 1.5%, with which two different lengths or types of fibers for suitable hybridization (0.0, 0.5, and 1.0) were adopted. All the variable specimens were tested for compressive strength according to test ages and flexural strength under four-point flexural loads. Furthermore, the absorbed flexure energy and synergy in the flexure of NSHSC by adding hybrid fibers were investigated. The detailed mixture proportions, materials, and mechanical test setup performed in this study are as follows.

**2.1. Mixture Proportions and Materials.** The cementitious materials of NSHSC in this study were Type I Portland cement (specific surface area of  $3,492 \text{ cm}^2/\text{g}$ , density of  $3.15 \text{ g/cm}^3$ ) and silica fume produced in Norway (specific surface area of  $200,000 \text{ cm}^2/\text{g}$ , density of  $2.20 \text{ g/cm}^3$ ). The sand grain size was smaller than 0.5 mm, and  $10 \mu\text{m}$  diameter filler (specific surface area of  $2.65 \text{ cm}^2/\text{g}$ , density of  $0.75 \text{ g/cm}^3$ ) including 99%  $\text{SiO}_2$  was used in the mixture. To provide suitable workability, liquid polycarboxylate superplasticizer (SP) was used. Three different water-to-

TABLE 1: The proportion of materials in the NSHSC mixture by cement weight ratio.

Cement	Silica fume	Filler	Sand	Water	Fiber	w/b
1.00	0.25	0.30	1.10	0.20-0.22		Table 2

binder ratio (w/b) values and two different fiber lengths and types with several volume fractions were adopted in the mixture, as described in Tables 1 and 2. Table 3 shows the chemical and physical properties of these materials. The high-strength polyethylene fibers and high-strength straight steel fibers were used to prevent fiber fracture before the fiber slip occurred between the fiber and the matrix. Two different lengths of PE fibers were adopted, and the fiber exhibited the following characteristics: an equivalent diameter of  $31 \mu\text{m}$ , a length of 12 or 18 mm, and a nominal tensile strength of 2,900 MPa. The SF used had an equivalent diameter of 0.2 mm, a length of 19.5 mm, and a nominal tensile strength of 2,650 MPa. The physical and geometric properties of the fibers are separately listed in Table 4. All variable specimens were designed based on the relative density method [15] and mixing procedure as shown in Figure 1. Furthermore, the specimens were cured after casting and demolding for 24 hours in a room with steady temperature and humidity until the testing date (28 days), at a temperature of  $20 \pm 1^\circ\text{C}$  and a relative humidity of  $60 \pm 5\%$ .

### 2.2. Details of the Mechanical Test and Setup

**2.2.1. Slump and Compressive Strength Test.** The slump tests were carried out according to ASTM C1437 [16]. Each variable specimen was tested after adding SP to obtain the target slump which was 0 mm of slump according to trial and error (Figure 1), then compacted by the exertion of pressure after pouring the concrete into test molds, and surface finishing was performed. This method is according to the previously published researches [17, 18], the use of a modified steel plate to compact the concrete into molds to produce specimens of the same density.

The compressive strength tests were carried out according to ASTM C39 [19], and the test setup is shown in Figure 2(a). Six cylindrical specimens for each variable were fabricated and used in the compressive strength tests. The cylindrical specimens with a diameter of 100 mm and height of 200 mm were used and tested at 7 and 28 days after casting. The test used a universal testing machine (UTM) with a maximum capacity of 250 tons under the monotonic rate of 0.2 mm/min.

**2.2.2. Flexural Strength Test.** Three prismatic specimens for each variable were fabricated and tested under four-point flexure according to ASTM C1609 [20]. The prismatic specimens used for measuring flexural strength had a width of 100 mm, height of 100 mm, and length of 400 mm. Each prism specimen was turned  $90^\circ$  from the casting surface and then failed completely at midspan. To eliminate the midspan deflection capacity of the prismatic specimens, a specialized steel frame with two linearly variable differential transformers (LVDTs) were attached to the side of the

TABLE 2: Details of various w/b of specimens and fiber hybridization.

	w/b (%)	w/c (%)	PE fibers (12 mm/%)	PE fibers (18 mm/%)	Steel fibers (19.5 mm/%)
U16.4-NF	16.4	0.20	—	—	—
U16.8-NF	16.8	0.21	—	—	—
U17.2-NF	17.2	0.22	—	—	—
U16.4-18PE1.5	16.4	0.20	—	1.5	—
U16.8-18PE1.5	16.8	0.21	—	1.5	—
U17.2-18PE1.5	17.2	0.22	—	1.5	—
U16.4-PP1.5	16.4	0.20	0.5	1.0	—
U17.2-PP1.5	17.2	0.22	0.5	1.0	—
U16.4-12SP0.5	16.4	0.20	0.5	—	1.0
U17.2-12SP0.5	17.2	0.22	0.5	—	1.0
U16.4-18SP1.0	16.4	0.20	—	1.0	0.5
U17.2-18SP1.0	17.2	0.22	—	1.0	0.5

TABLE 3: Chemical compositions and physical properties of cementitious materials.

	Surface area (cm <sup>2</sup> /g)	Density (g/cm <sup>3</sup> )	Chemical composition (%)							
			SiO <sub>2</sub>	Al <sub>2</sub> O <sub>3</sub>	Fe <sub>2</sub> O <sub>3</sub>	CaO	MgO	SO <sub>3</sub>	Na <sub>2</sub> O	K <sub>2</sub> O
Cement	3,492	3.15	21.16	4.65	3.14	62.79	2.81	2.13	—	—
Silica fume	200,000	2.20	96.00	0.25	0.12	0.38	0.10	<0.2	—	—
Filler	2.65	0.75	99.60	0.31	0.025	0.010	0.006	—	0.009	0.004

TABLE 4: Properties of polyethylene and steel fiber.

	Diameter, $d_f$	Length, $l_f$ (mm)	Aspect ratio ( $l_f/d_f$ )	Density (g/cm <sup>3</sup> )	Tensile strength (MPa)	Elastic modulus (GPa)
Polyethylene fiber	31 $\mu$ m	12 18	387 580	0.97	2,900	100
Steel fiber	0.2 mm	19.5	97.5	7.8	2,650	200



FIGURE 1: Mixing, curing, and test method of NSHSC.

prismatic specimens. The tests were performed using the UTM described above, switched to displacement control at a rate of 0.3 mm/min (Figure 2(b)). The curing conditions were the same as those of the cylindrical specimens in the compressive strength test.

According to ASTM C1609, a load versus deflection curve was obtained, which can be calculated based on

different toughness indices  $I_5$ ,  $I_{10}$ , and  $I_{30}$ . The toughness index defined by ASTM C1018 [21] is calculated from the area under the flexural load-deflection curve up to a given deflection divided by the first cracking in the area under the same curve. Furthermore, the energy absorbed and toughness factor of the various fiber-reinforced specimens can be further analyzed. The calculation method for the flexural

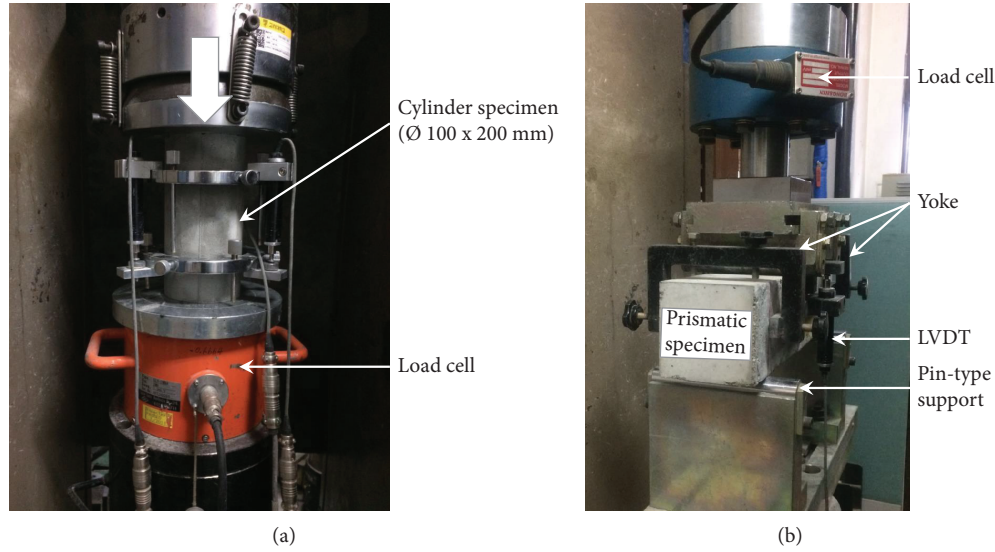


FIGURE 2: Mechanical test setup: (a) compressive test (ASTM C39) and (b) flexural test (ASTM C1609).

TABLE 5: Test results of compressive and flexural strength.

	Compressive strength						Flexural strength						Toughness index		
	7 days (MPa)			28 days (MPa)			28 days (MPa)						$I_5$	$I_{10}$	$I_{30}$
	Mean	COV	Test results	Mean	COV	Test results	Mean	COV	Test results	Mean	COV	Test results			
U16.4-NF	90.9	4.0%	92.9 85.9 94.1	120.9	4.3%	126.8 114.3 121.5	6.0	29.0%	8.3 5.6 4.1	—	—	—	—	—	—
U16.8-NF	89.1	2.3%	90.9 86.2 90.2	109.1	2.3%	109.2 105.9 112.1	3.6	18.6%	4.3 3.7 2.7	—	—	—	—	—	—
U17.2-NF	91.9	0.6%	92.1 91.2 92.4	122.0	1.8%	125.0 119.7 121.3	5.7	15.7%	5.3 4.9 6.9	—	—	—	—	—	—
U16.4-18PE1.5	80.9	4.7%	80.3 76.6 85.7	121.9	4.5%	120.1 129.4 116.2	15.3	4.0%	15.8 15.5 14.4	4.9	11.0	43.3	—	—	—
U16.8-18PE1.5	79.0	4.2%	83.3 75.2 78.5	120.8	3.1%	125.0 116.0 121.4	15.2	15.4%	18.2 14.7 12.6	5.2	11.2	41.9	—	—	—
U17.2-18PE1.5	81.0	1.5%	82.3 81.3 79.4	124.9	0.1%	125.0 124.7 125.0	23.1	19.3%	23.1 28.6 17.7	5.3	12.2	62.2	—	—	—
U16.4-PP1.5	81.2	1.7%	80.9 79.7 83.1	116.2	3.1%	118.9 111.1 118.4	19.6	17.0%	13.4 20.5 16.8	4.9	10.4	32.4	—	—	—
U17.2-PP1.5	81.9	1.6%	80.2 83.3 82.1	117.3	1.6%	119.5 117.2 115.0	22.1	11.6%	19.2 24.3 22.8	5.5	11.8	48.4	—	—	—
U16.4-12SP0.5	86.0	3.9%	82.5 85.0 90.6	123.2	0.7%	122.9 124.5 122.3	19.0	8.6%	20.3 28.1 19.5	5.5	17.1	71.1	—	—	—
U17.2-12SP0.5	86.3	5.0%	82.6 92.3 84.0	123.4	0.3%	123.9 123.1 123.1	21.9	8.5%	24.1 19.6 22.1	5.4	12.2	58.8	—	—	—
U16.4-18SP1.0	85.9	1.5%	80.9 79.7 83.1	123.3	0.7%	122.0 123.9 123.9	14.7	5.1%	13.9 14.3 15.8	4.8	11.2	51.5	—	—	—
U17.2-18SP1.0	86.0	1.6%	80.2 83.3 82.1	122.9	3.5%	128.4 122.2 118.1	18.5	10.5%	21.0 18.3 16.3	5.3	15.7	59.3	—	—	—

Note: mean = mean value of test strength; COV = coefficient of variation.

toughness factor ( $FT_\delta$ ) was defined by the Japan Society of Civil Engineers (JSCE) [22] and the details of the equation is as follows:

$$FT_\delta = \frac{T_{b,\delta}L}{\delta b d^2}, \quad (1)$$

where  $T_{b,\delta}$  denotes the area under the curve to a flexural specimen displacement of  $\delta$ ,  $L$  denotes the span of the specimen, and  $b$  and  $d$  denote the width and depth of the specimen.

### 3. Experimental Results and Discussion

**3.1. Compressive Strength.** Table 5 summarizes the average strength and coefficient of variation at test ages based on

the compressive strength test. A minimum of three concrete cylinders were prepared and tested at 7 and 28 days after curing conditions.

The NSHSC specimen with a w/b of 17.2% and without fibers had slightly higher compressive strength with a small coefficient of variation among the specimens. The exhibited values of compressive strength (and coefficient of variation) were 91.9 (0.6%) and 122.0 (1.80%) MPa at 7 and 28 days, respectively. The NSHSC specimens with a fiber volume fraction of 1.5% of 18 mm PE fibers showed similar behavior and strength at 28 days to NSHSC without fibers, and specimen U17.2-18PE1.5 demonstrated a slightly high strength with a small value of the coefficient of variation as well. Furthermore, the addition of PE fibers improved the energy dissipation capacity, which inhibits crack propagation and development in the concrete matrix, and ensured that the

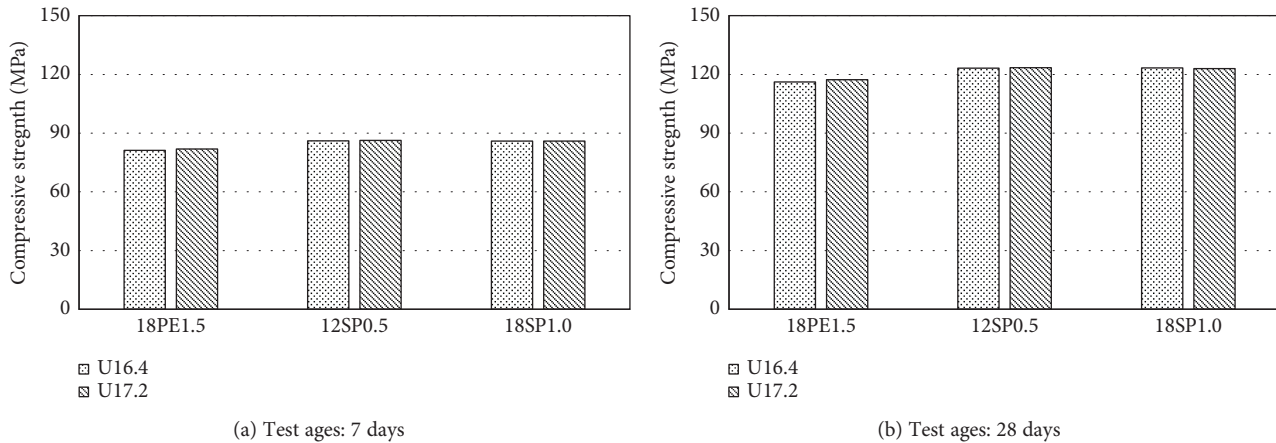


FIGURE 3: Compressive strength of hybrid fibers reinforced NSHSC.

PE fiber-reinforced specimens were not completely crushed [23]. A w/b of 16.8% with or without fibers resulted in low-strength behavior; hence, it was eliminated from the evaluation of the mechanical performance of fiber hybridization.

The compressive properties of hybrid PE fibers and SF-reinforced NSHSC at 7 and 28 days are shown in Figure 3. The specimens included PE fibers with an aspect ratio of 387 and 580 (U16.4-PP1.5, U17.2-PP1.5), respectively, and exhibited low compressive strength, approximately 4.8-6.1% lower than that of specimens with different fiber types. The specimens with different lengths of the PE fibers and SF were found to have similar compressive strengths of over 85 and 123 MPa at 7 and 28 days, respectively.

### 3.2. Flexural Properties of Specimens with Combined Fibers

**3.2.1. Flexural Behavior.** In the flexural strength test, the specimens without PE fibers had a sudden load drop immediately after the first crack occurred. This means that the values of the first-cracking strength and postcracking strength were the same in the specimens without fibers, as the load-carrying capacity of those specimens decreased to almost zero immediately after matrix cracking. Specimen U16.8-NF exhibited lower flexural strength, in a manner similar to compressive strength. Because of the fiber bridging with the matrix and the propagation of cracks in the loading process, specimens reinforced by 1.5 vol.% of PE fibers (18 mm) were found to have an increased load-carrying capacity after matrix cracking, which was approximately 1.5-3.1 times the postcracking strength of the specimens without fibers. Otherwise, midspan deflection increased continuously during the loading the process, and eventually, a localized crack occurred due to the sharply decreasing load in the prismatic specimens. Of those, specimen U17.2-18PE1.5 showed the most enhanced postcracking strength among the specimens with PE fibers.

Based on the load-deflection curve, the different toughness indices  $I_5$ ,  $I_{10}$ , and  $I_{30}$  of the fiber-reinforced NSHSC specimens were calculated. Specimens with w/b of 16.4% and 16.8% using 1.5 vol.% of PE fibers had similar toughness indices values at the same deflection. Toughness index values as high as 62.2 were measured with a w/b of 17.2% containing

1.5 vol.% PE fibers. According to recent studies [24], the fiber-reinforced cementitious composites with toughness indices  $I_5 > 5$ ,  $I_{10} > 10$ , and  $I_{30} > 30$  can be defined as strain-hardening composites. Specimens with PE fibers studied in this investigation were based on the above criteria and can, therefore, be defined as strain-hardening materials, as shown in Table 5. In addition, NSHSC with 1.5 vol.% PE fibers exhibited high ductility along with high toughness indices; thus, the average midspan deflection was over 6 mm, which was about 2% of the specimen's span length. This is because the PE fibers induced a delay in localized cracking and ensured the formation of multiple cracks due to the increased energy absorption capacity [25].

#### 3.2.2. Flexural Behavior of Hybrid Fiber-Reinforced NSHSC.

Figure 4 shows the flexural load versus midspan deflection curve of hybrid fiber-reinforced NSHSC. Because the combination of two or more fibers provides different responses to the cracking process during different stages of loading, the flexural strength was increased by specimens containing a composite with hybrid fibers, rather than single fiber reinforcement. Moreover, all of the specimens show strain-hardening behavior based on the above criteria, and the values are noted in Table 5. The hybrid PE fibers with different lengths (U16.4-PP1.5, U17.2-PP1.5) exhibited a somewhat low flexural strength but similar strain capacities (high strain capacities) to those of the specimens with hybrid PE fibers and SF. This is due to the low modulus of the PE fibers, which leads to low strength and the high strain capacity, and the high strength is due to the high modulus of the SF [26, 27]. Furthermore, in the hybrid SF and PE fiber specimens, the hybrid method with long SF and short PE fibers exhibited higher flexural strength, toughness, and strain capacity than those of the combined long SF and long PE fibers (Figure 4). For example, specimen U16.4-12SP0.5 exhibited a high postcracking strength and toughness index at  $15.5\delta$ , which were approximately 29.3%, and 37.9% higher than those of specimen U16.4-18SP1.0, respectively. In terms of the different sizes of the fibers, the short fibers bridge microcracks and control their coalescence into macrocracks, whereas the long fibers

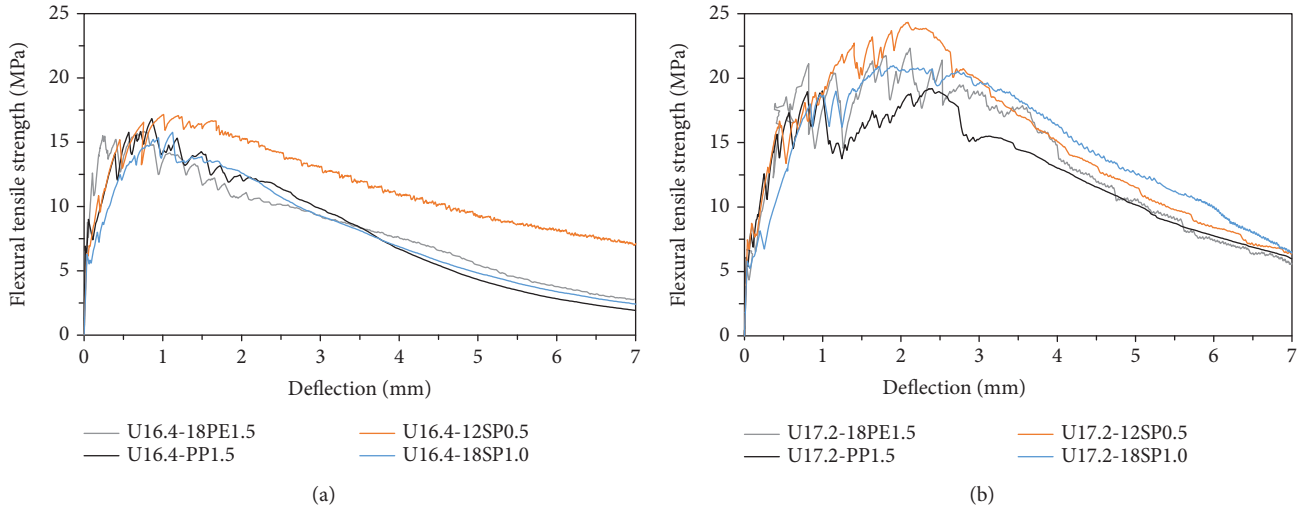


FIGURE 4: Flexural load-deflection curves: (a) w/b of 16.4% and (b) w/b of 17.2%.

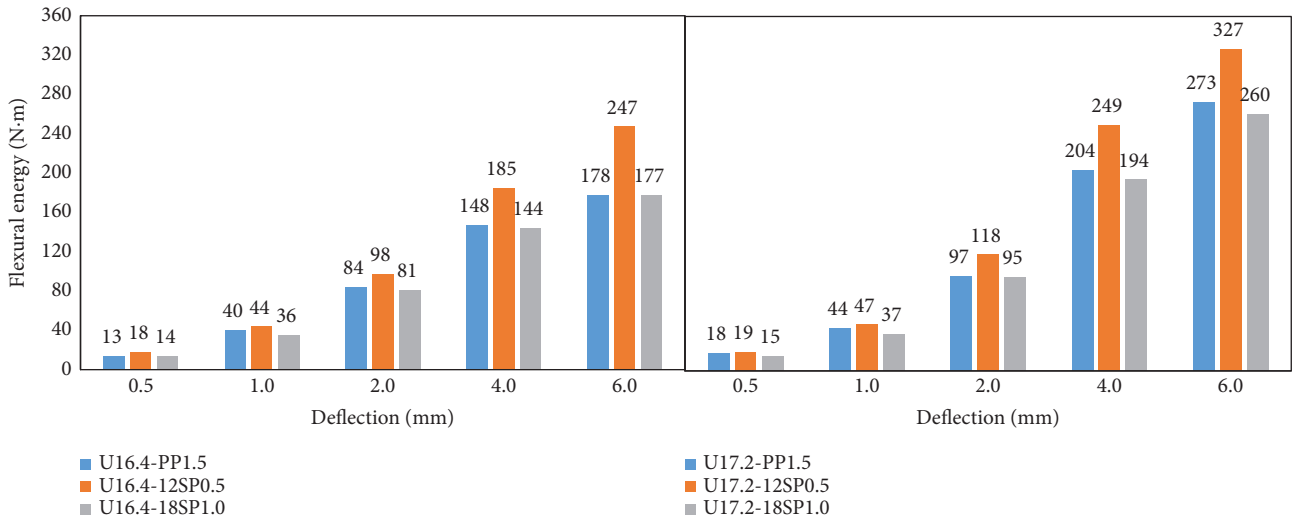


FIGURE 5: Flexural energy absorption values calculated according to the curve in Figure 4.

contribute to arrest and prohibit the propagation of macrocracks [28, 29]. Hence, specimens achieved high strength, toughness, and strain capacity according to the control of micro- and macrocracks.

The flexural strength versus w/b of hybrid fiber-reinforced NSHSC is shown in Figure 4 and Table 5. Specimens with w/b of 17.2% and hybridization fibers PP1.5, 12SP0.5, and 18SP1.0 had the average postcracking strength of 22, 22, and 19 MPa, respectively. These values are approximately 29.4%, 15.8%, and 58.3% higher than specimens with a w/b of 16.4% and hybridization fibers, respectively. However, specimens with a w/b of 16.4% and hybridization fibers exhibited high toughness and over 2% of the specimen’s span length in the deflection. Because specimen U17.2 had slightly higher compressive strength than specimen U16.4, the postcracking strength increased with the increasing interfacial bond strength between the fiber and the matrix and was

strongly influenced by the fiber orientation and dispersion in the specimens [30, 31].

**3.2.3. Flexural Energy Absorption and Toughness Factor.** The energy absorption was calculated for flexural deflections of 0.5, 1.0, 2.0, 4.0, and 6.0 mm in order to evaluate the effect of fiber hybridization, especially for the energy dissipated under four-point flexure and plotted in Figure 5. All of the specimens with hybrid fibers exhibited multiple growths during 0.5 mm to 2.0 mm in the flexural energy absorption, and then, the amount of absorbed flexural energy decreased from 4.0 mm. Among these specimens, the hybrid short PE fiber and SF exhibited higher energy absorption values at all the considered deflection levels. The energy absorption capacity of two w/b values was shown to be similar before 2.0 mm of midspan deflection, and the U17.2 specimens distinctly enhanced the energy absorption capacity to

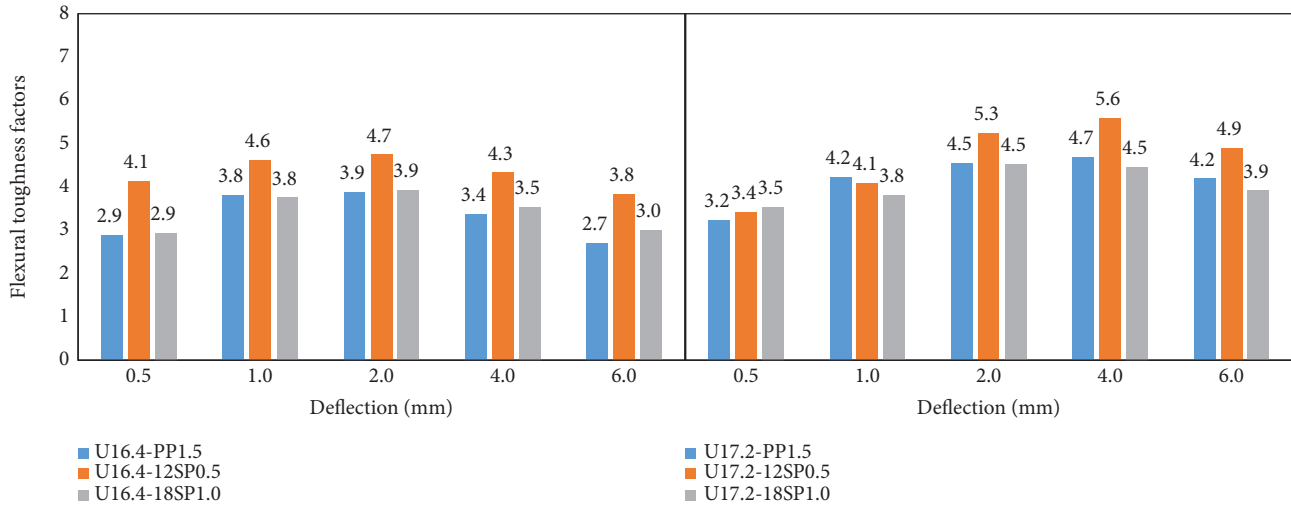


FIGURE 6: Flexural toughness factors calculated according to the curve in Figure 4 ( $FT_{\delta}$  in MPa).

more than that of the U16.4 specimens from 4.0 mm of mid-span deflection, as shown in Figure 5. It can be concluded that the different type and different lengths of hybridization fibers can significantly improve the flexural strength, toughness, and energy absorption capacity.

In order to evaluate the synergy in flexure and the effect of fiber hybridization, the flexural toughness factor ( $FT_{\delta}$ ) was calculated at flexural deflections of 0.5, 1.0, 2.0, 4.0, and 6.0 mm according to equation (1). The behavior was similar to flexural energy absorption, for which the NSHSC hybrid with a short PE fiber and SF exhibited a higher toughening ability at each deflection (Figure 6).

**3.3. Synergy in Flexure according to the Various Hybrid Fiber-Reinforced NSHSC.** The hybrid fiber-reinforced cementitious composite derives the benefits from each of the single fibers and exhibits a synergetic response [30–33]. Therefore, the various hybrid fibers of NSHSC were evaluated and the synergy was calculated in this study, based on equation (2). Because the materials were nonuniform, a simplistic method was used to evaluate the effect of hybridization on toughness, fracture mechanisms, and the interplay between each fiber within the matrix [33, 34].

$$\text{Synergy} = \frac{FT_{\text{hybrid},a+b}}{(FT_a + FT_b)} - 1, \quad (2)$$

where  $FT_{\text{hybrid},a+b}$  denotes the flexural toughness factor to a deflection of various hybridizations and  $FT_a$  and  $FT_b$  denote the flexural toughness factor to a deflection of individual fiber-reinforced composites.

The method for the synergy analysis was defined based on the concepts of positive synergy, negative synergy, and zero synergy. The positive synergy (synergy > 0) denotes that properties of hybrid fiber-reinforced composite were numerically greater than the sum of the properties produced by the single fiber types, and the negative synergy (synergy < 0) denotes that the properties of the hybrid fiber-reinforced composite were poorer than the sum of the properties

produced by the single fiber types, and the zero synergy indicates no synergy in hybridization.

**3.3.1. Flexural Behavior of Individual Fiber-Reinforced NSHSC.** In order to further evaluate the synergy for the various hybrid fiber-reinforced NSHSCs, specimens with two w/b and a single fiber type (fiber volume fraction according to hybridization) were fabricated and evaluated. The average flexural load-deflection is shown in Figure 7. In the specimens with a fiber volume fraction of 0.5%, NSHSC with SF showed higher postcracking strength and toughness compared with specimens using PE fibers, where the length of the SF was longer than that of the PE fibers. Due to the effect of the PE fiber on multiple-cracking behavior, in the specimens with similar length fibers of 1.0 vol.%, specimens with PE fibers exhibited higher postcracking strength and strain capacity at peak load than those using SF. The flexural behavior of individual fiber-reinforced NSHSC exhibited similar flexural strength to that of fiber hybridization, for which w/b of 17.2% showed more improvement in the properties than a w/b of 16.4% for all of the specimens considered.

**3.3.2. Synergy of Hybrid Fiber-Reinforced NSHSC.** As previously stated, synergy associated with various NSHSCs has been evaluated. For the striking contrast between specimens hybrid fiber-reinforced and individual fiber-reinforced NSHSCs, the average flexural load-deflection curve by various conditions was shown in Figures 8 and 9, respectively. Furthermore, the synergy of various hybrid fiber-reinforced NSHSCs was calculated and shown in Figure 10.

In the w/b of 16.4%, the specimen hybrid with SF and short PE fibers had positive synergy in all instances (in this study), and the synergy significantly increased with increasing deflection. The toughness of the specimen with 0.5 vol.% exhibited a low value and decreased rapidly from 2.0 mm of deflection, as shown in Figure 8(b). Short PE fibers with low modulus bridged microcracks and improved microcracks in the matrix, whereas long SF arrested the propagation of macrocracks. In contrast, specimen hybrid with

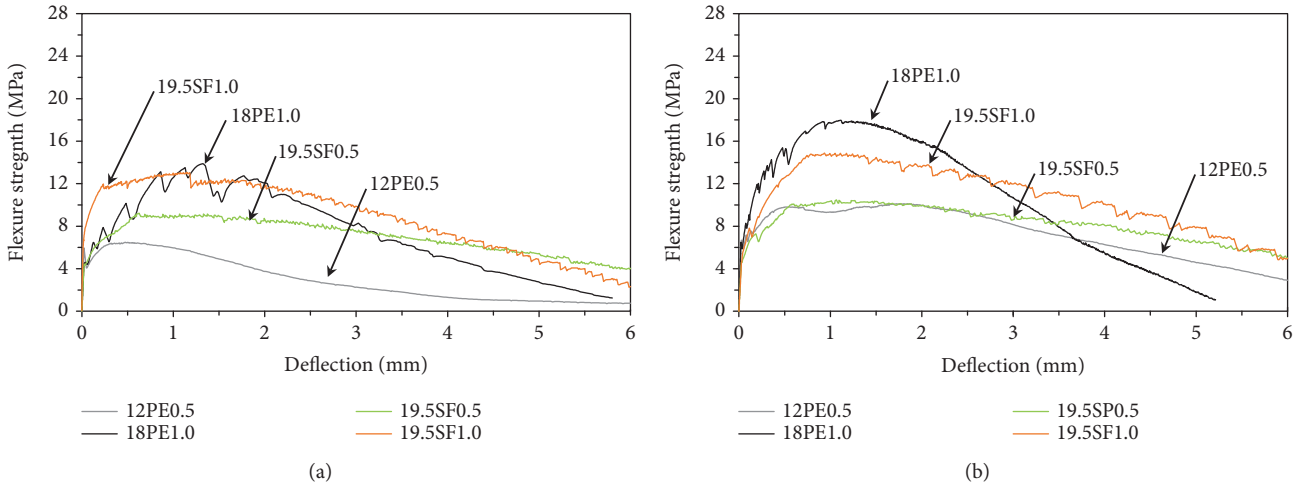


FIGURE 7: Average flexure load-deflection behavior by individual fibers: (a) various specimens of U16.4 and (b) various specimens of U17.2.

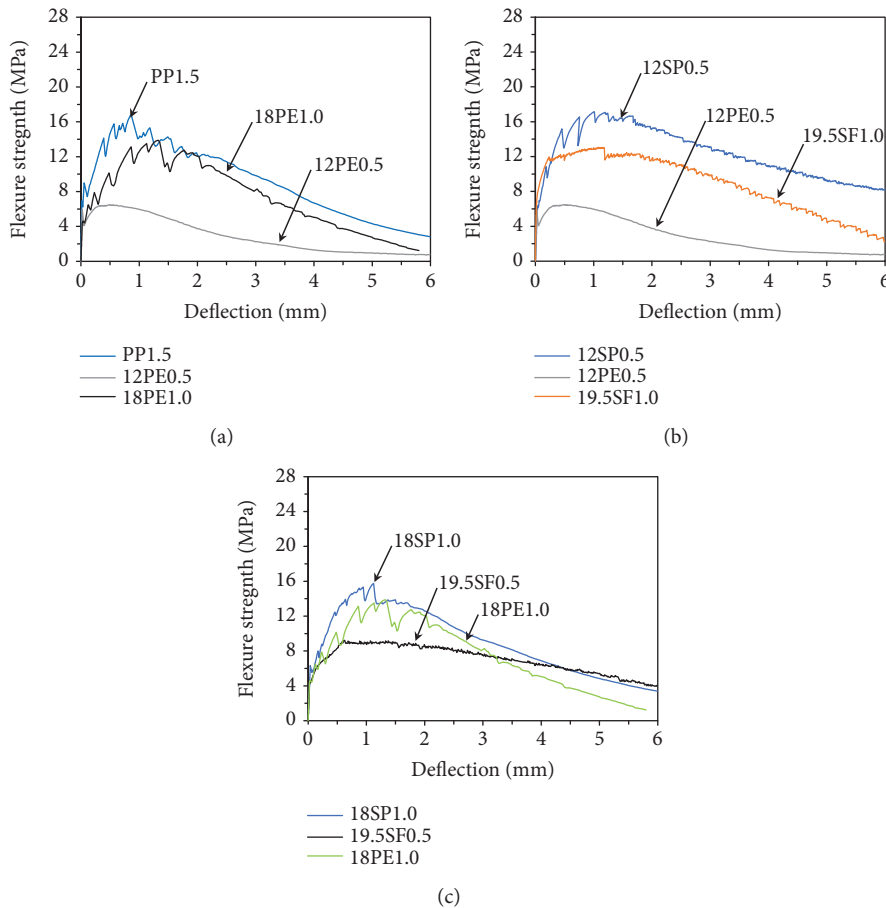


FIGURE 8: Average flexural load-deflection behavior by various conditions of w/b of 16.4%: (a) U16.4 based on PE fibers with different lengths, (b) U16.4 based on steel fibers with short PE fibers, and (c) U16.4 based on steel fibers with long PE fibers.

different lengths of PE fiber had negative synergy in all cases, and there was almost no variation from 0.5 mm to 6.0 mm. The specimen hybrid with SF and long PE fiber exhibited the negative synergy between 0.5 mm and 4.0 mm, and the synergy gradually approached zero synergy with increasing deflection, before exhibiting positive synergy at

6.0 mm of deflection. Zero synergy occurred in specimens U16.4-12SP0.5 at 0.5 mm of deflection.

In samples with a w/b of 17.2%, there is an indication of the negative synergy before 1.0 mm of deflection in all instances (in this study). The specimen hybrid with SF and short PE fibers indicated positive synergy after 2.0 mm of

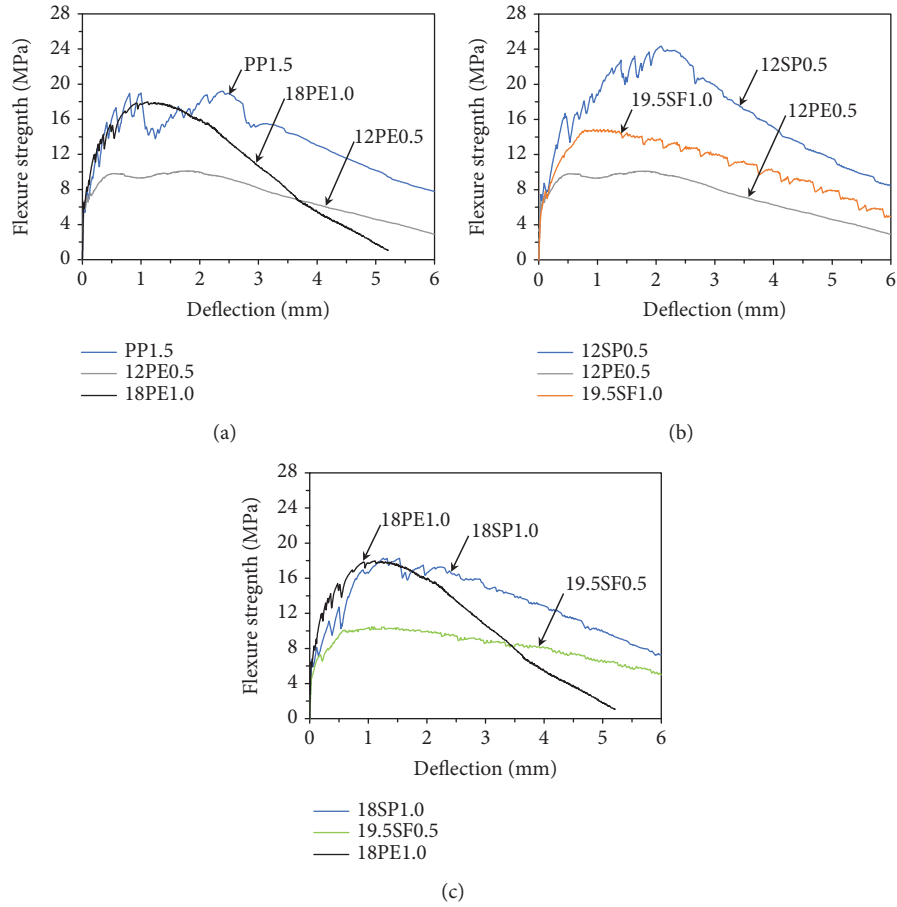


FIGURE 9: Average flexural load-deflection behavior by various conditions of w/b of 17.2%: (a) U17.2 based on PE fibers with different lengths, (b) U17.2 based on steel fibers with short PE fibers, and (c) U17.2 based on steel fibers with long PE fibers.

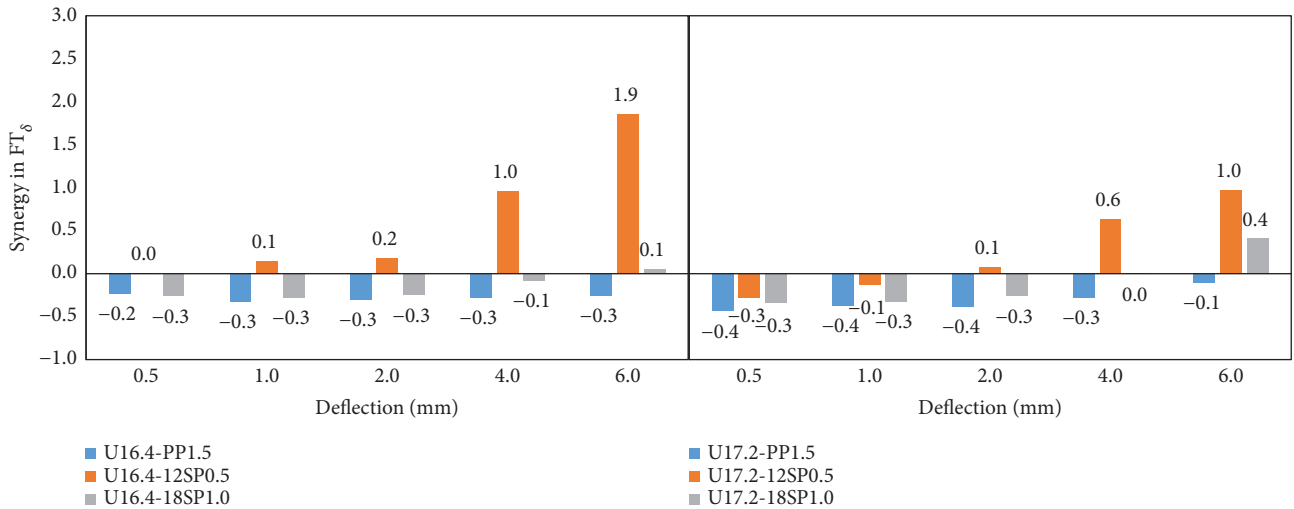


FIGURE 10: Synergy in flexural properties based on a four-point flexural load-deflection curve.

deflection, and the synergy significantly increased with increasing deflection. The specimen hybrid with steel fiber and long fibers showed positive synergy at 6.0 mm of deflection, and the hybrid with different lengths of PE fiber

exhibited negative synergy in all instances, which was a similar behavior to the specimen with a w/b of 16.4%. From the above, the result can be inferred according to the flexural load-deflection curves shown in Figures 8 and 9.

An attempt is made here to identify the hybrid fiber combinations with which NSHSC displayed positive synergy using SF and PE fibers, compared with different lengths of PE fibers based on the flexural toughness. This may be a consequence of hybridizing with PE fibers, whose fiber length and type were weak in the bridging of microcracks. The fiber bridging effect of fiber-reinforced composites was influenced by fiber size (length, diameter), fiber type (modulus), and the bond strength between the fiber and the matrix. However, among those influence factors, the bond strength between the fiber and the matrix should be sufficient to fracture the fiber, which leads to the fiber-reinforced composite exhibiting great ductile behavior. Thus, an increase in the strength of matrix may strengthen the bond between the fiber and the matrix and, in turn, provide increased reinforcement efficiency and toughness. It is possible that, for this reason, NSHSC with SF and PE fiber exhibited better synergy in this study than the hybrid with different lengths of PE fiber-reinforced composite, which had significantly higher compressive strength than the hybrid with different lengths of PE fiber-reinforced composite (Table 5).

#### 4. Conclusions

An experimental investigation was performed to evaluate the mechanical properties of no-slump high-strength concrete with various fiber hybridizations. The three different water-to-binder ratios of various specimens with steel fiber and PE fiber using a fiber volume fraction of 0.0, 1.5% were fabricated and tested compressive strength and under four-point flexure loading at plan age. Furthermore, the flexural toughness and the synergy based on the fiber hybridization were evaluated.

Based on the results of this investigation, the following concluding remarks are obtained:

- (1) The specimens with a water-to-binder ratio of 17.2% exhibited a higher compressive strength and low coefficient of variation in all instances. In contrast, the water-to-binder ratio of 16.8% exhibited low properties and not only compressive but also flexural strength, which used 18 mm of polyethylene fibers; hence, it was eliminated at the evaluated mechanical performance of fiber hybridization under study
- (2) Flexural strength of hybridization in specimens with fibers had improved over 1.5 times higher postcracking strength than that in specimens without fibers. Due to the PE fibers having low modulus that leads to low strength and high strain capacity and high strength due to high modulus of steel fibers, the specimen hybrid PE fibers with different lengths exhibit a slightly low flexural strength but similar strain capacities (high strain capacities) compared with the specimen hybrid PE fibers and steel fibers. And the water-to-binder ratio of 17.4% of specimens showed a higher flexural strength compare with that of specimens at the same fiber volume fraction

- (3) And the exhibited strain hardening based on evaluated toughness, with toughness indices  $I_5 > 5$ ,  $I_{10} > 10$ , and  $I_{30} > 30$ , can be defined as a strain-hardening-type composite. However, specimen hybrid with steel fiber and short PE fibers exhibited a higher flexural strength and toughness than that of other various hybridizations, which based on the short fibers that bridge microcracks and control its coalescence to macrocracks; in contrast, the long fibers are aimed at arresting and prohibiting the propagation of macrocracks
- (4) A specimen hybrid with steel fiber and short PE fiber indicates positive synergy, and a hybrid with different lengths of PE fiber exhibited the negative synergy in all instances. This may be the consequence of PE fiber length, and the type was weak in the bridged macrocracks due to hybridization with different lengths of PE fibers

#### Data Availability

The data used to support the findings of this study are available from the corresponding author upon request.

#### Conflicts of Interest

The authors declare that they have no conflicts of interest.

#### Acknowledgments

This work was supported by the National Research Foundation of Korea (NRF) grant funded by the Korea government (MEST) (NRF-2016R1A2B3011392).

#### References

- [1] ACI 211.3, *Guide for Selecting Proportions for No-Slump Concrete*, American Concrete Institute, Farmington Hills (MI), 2002.
- [2] J. Sobhani, M. Najimi, A. R. Pourkhorshidi, and T. Parhizkar, "Prediction of the compressive strength of no-slump concrete: a comparative study of regression, neural network and ANFIS models," *Construction and Building Materials*, vol. 24, no. 5, pp. 709–718, 2010.
- [3] M. Najimi, J. Sobhani, and A. R. Pourkhorshidi, "A comprehensive study on no-slump concrete: from laboratory towards manufactory," *Construction and Building Materials*, vol. 30, pp. 529–536, 2012.
- [4] H. Hoornahad, "Toward development of self-compacting no-slump concrete mixtures," Doctoral thesis, Delft University of Technology, 2014.
- [5] ACI 207.5, *Roller-Compacted Mass Concrete*. American Concrete Institute, American Concrete Institute, Farmington Hills (MI), 1999.
- [6] V. C. Li, "On engineered cementitious composites (ECC): a review of the material and its applications," *Journal of Advanced Concrete Technology*, vol. 1, no. 3, pp. 215–230, 2003.

- [7] N. Banthia and R. Gupta, "Hybrid fiber reinforced concrete (HyFRC): fiber synergy in high strength matrices," *Materials and Structures*, vol. 37, no. 10, pp. 707–716, 2004.
- [8] S. H. Park, D. J. Kim, G. S. Ryu, and K. T. Koh, "Tensile behavior of ultra high performance hybrid fiber reinforced concrete," *Cement and Concrete Composites*, vol. 34, no. 2, pp. 172–184, 2012.
- [9] D. J. Kim, S. H. Park, G. S. Ryu, and K. T. Koh, "Comparative flexural behavior of hybrid ultra high performance fiber reinforced concrete with different macro fibers," *Construction and Building Materials*, vol. 25, no. 11, pp. 4144–4155, 2011.
- [10] H. R. Pakravan, M. Latifi, and M. Jamshidi, "Hybrid short fiber reinforcement system in concrete: a review," *Construction and Building Materials*, vol. 142, pp. 280–294, 2017.
- [11] N. Banthia and M. Sappakittipakorn, "Toughness enhancement in steel fiber reinforced concrete through fiber hybridization," *Cement and Concrete Research*, vol. 37, no. 9, pp. 1366–1372, 2007.
- [12] J. S. Lawler, T. Wilhelm, D. Zampini, and S. P. Shah, "Fracture processes of hybrid fiber-reinforced mortar," *Materials and Structures*, vol. 36, no. 3, pp. 197–208, 2003.
- [13] D. L. Nguyen, D. J. Kim, G. S. Ryu, and K. T. Koh, "Size effect on flexural behavior of ultra-high-performance hybrid fiber-reinforced concrete," *Composites Part B: Engineering*, vol. 45, no. 1, pp. 1104–1116, 2013.
- [14] S. F. U. Ahmed and H. Mihashi, "Strain hardening behavior of lightweight hybrid polyvinyl alcohol (PVA) fiber reinforced cement composites," *Materials and Structures*, vol. 44, no. 6, pp. 1179–1191, 2011.
- [15] P. Richard and M. Cheyrez, "Composition of reactive powder concretes," *Cement and Concrete Research*, vol. 25, no. 7, pp. 1501–1511, 1995.
- [16] ASTM C1437, *Standard Test Method for Flow of Hydraulic Cement Mortar*, ASTM International, West Conshohocken, PA, 2007.
- [17] A. Olar, N. Hearn, and D. Wannamaker, "Implementation of the maturity method for zero-slump concrete products," *PCI Journal*, vol. 49, no. 2, pp. 86–97, 2004.
- [18] Sørensen and O. Christian, "The stability of fresh zero-slump concrete," *Concrete Research*, vol. 4, no. 3, pp. 656–667, 2013.
- [19] ASTM C39/C39M, *Standard Test Method for Compressive Strength of Cylindrical Concrete Specimens*, ASTM International, West Conshohocken, PA, 2014.
- [20] ASTM, *C1609/C1609M, Standard Test Method for Flexural Performance of Fiber-Reinforced Concrete (Using Beam with Third-Point Loading)*, ASTM International, West Conshohocken, PA, 2012.
- [21] ASTM C1018, *Standard Test Method for Flexural Toughness and First Crack Strength of Fiber Reinforced Concrete (Using Beam with Third-Point Loading)*, ASTM International, West Conshohocken, PA, 1997.
- [22] JSCE-G 552-1999, "Test method for bending strength and bending toughness of steel fiber reinforced concrete," in *Standard Specification for Concrete Structures, Test Methods and Specifications*, p. 365, JSCE, 2005.
- [23] S. T. Kang, J. I. Choi, K. T. Koh, K. S. Lee, and B. Y. Lee, "Hybrid effects of steel fiber and microfiber on the tensile behavior of ultra-high performance concrete," *Composite Structures*, vol. 145, pp. 37–42, 2016.
- [24] A. E. Naaman and H. W. Reinhardt, "Characterization of high-performance fiber reinforced cement composites," in *Proceedings of the Second International RILEM Workshop*, pp. 1–24, USA, June 1995.
- [25] K. Q. Yu, J. T. Yu, J. G. Dai, Z. D. Lu, and S. P. Shah, "Development of ultra-high performance engineered cementitious composites using polyethylene (PE) fibers," *Construction and Building Materials*, vol. 158, pp. 217–227, 2018.
- [26] S. F. U. Ahmed and M. U. F. Maalej, "Tensile strain hardening behaviour of hybrid steel-polyethylene fibre reinforced cementitious composites," *Construction and Building Materials*, vol. 23, no. 1, pp. 96–106, 2009.
- [27] S. F. Ahmed, M. Maalej, and P. Paramasivam, "Analytical model for tensile strain hardening and multiple cracking behavior of hybrid fiber-engineered cementitious composites," *Journal of Materials in Civil Engineering*, vol. 19, no. 7, pp. 527–539, 2007.
- [28] I. Markovic, "High-performance hybrid-fiber concrete – development and utilization," Ph. D Thesis T.U.Delft, 2006.
- [29] N. Banthia, A. Moncef, K. Chokri, and J. Sheng, "Uniaxial tensile response of microfibre reinforced cement composites," *Materials and Structures*, vol. 28, no. 9, pp. 507–517, 1995.
- [30] L. Ferrara, N. Ozyurt, and M. di Prisco, "High mechanical performance of fibre reinforced cementitious composites: the role of "casting-flow induced" fibre orientation," *Materials and Structures*, vol. 44, no. 1, pp. 109–128, 2011.
- [31] D. Y. Yoo, N. Banthia, S. T. Kang, and Y. S. Yoon, "Effect of fiber orientation on the rate-dependent flexural behavior of ultra-high-performance fiber-reinforced concrete," *Composite Structures*, vol. 157, no. 6, pp. 62–70, 2016.
- [32] N. Banthia and S. M. Soleimani, "Flexural response of hybrid fiber-reinforced cementitious composites," *ACI Materials Journal*, vol. 102, no. 6, pp. 382–389, 2005.
- [33] N. Banthia, F. Majdzadeh, J. Wu, and V. Bindiganavile, "Fiber synergy in hybrid fiber reinforced concrete (HyFRC) in flexure and direct shear," *Cement and Concrete Composites*, vol. 48, pp. 91–97, 2014.
- [34] Y. W. Mai, R. Andonian, and B. Cotterell, "On polypropylene-cellulose fibre-cement hybrid composites," in *Advances in Composite Materials*, pp. 1687–1699, Proceedings of the Third International Conference on Composite Materials, Pairs, 1980.

## Research Article

# Proposition of Thin-Layer Repairing Methods Using Low-Elasticity Polymer Portland Cement Materials and Glue and Study on the Fatigue Resistance of Reinforced Concrete Slab

Tadashi Abe <sup>1</sup>, Kiyoshi Ito,<sup>2</sup> Noriyuki Kozakai,<sup>3</sup> and Takayoshi Kodama<sup>4</sup>

<sup>1</sup>College of Industrial Technology, Nihon University, Narashino City, Chiba 275-8575, Japan

<sup>2</sup>Nihon University Graduate School of Engineering, Nihon University, Narashino City, Chiba 275-8575, Japan

<sup>3</sup>Construction Materials Division, Sumitomo Osaka Cement Co., Ltd, Chiyoda-ku, Tokyo 102-8465, Japan

<sup>4</sup>Technical Sales Division, Kajima Road Co., Ltd, Bunkyo-ku, Tokyo 112-8566, Japan

Correspondence should be addressed to Tadashi Abe; [abe.tadashi@nihon-u.ac.jp](mailto:abe.tadashi@nihon-u.ac.jp)

Received 3 March 2018; Revised 2 September 2018; Accepted 13 September 2018; Published 29 November 2018

Guest Editor: Rishi Gupta

Copyright © 2018 Tadashi Abe et al. This is an open access article distributed under the Creative Commons Attribution License, which permits unrestricted use, distribution, and reproduction in any medium, provided the original work is properly cited.

In this repair method, two types of adhesives, such as a penetrable adhesive and a high-durability adhesive, were applied to the adhesion interface of the materials to be repaired, and then cast. The repair method was then evaluated for fatigue resistance using wheel load running tests. It was developed to ensure the long-term integrity of the repair material and RC slabs. The results of the experiments confirmed that this repair method provides significantly better fatigue resistance than the conventional construction method. Moreover, this study proposes two wet repair cycles and one dry repair cycle with reinforcement measures to improve the load-bearing performance.

## 1. Introduction

Most of the Japanese road bridges were built between 1950 and 1970. By 2026, 46% of these bridges will be 50 years old or older, making the maintenance and management of aging bridges an important issue [1, 2]. Furthermore, implementation of waterproofing for the RC slabs was delayed. In fact, waterproofing in the design and during maintenance was required for expressways in 1988, but it was required for general national roads only after the road bridge specification was revised in 2002 [3]. For this reason, the upper surface of RC slabs covered with about 80 mm of asphalt pavement gets wet from rainwater and the damage from traffic load is accelerated. It was left untouched, and the damage due to cracks and potholes in the asphalt pavement has been left unrepaired. Japan is an elongated archipelago surrounded by water and has a varied climate with cold and temperate regions. As a result, bridges are affected by airborne salt near the coastline and by damage by salt attack. Bridges are also affected by freezing damage from the snow-melting and antifreezing agents that are used in snowy

areas. Particularly in snowy cold regions, reinforcing bars become corroded, and the spraying of snow-melting agents and antifreezing agents causes daily freeze-thawing action. These factors accelerate damage to the concrete. As a result, the top surface concrete of RC slabs has been degraded into aggregate due to corrosion of the reinforcement caused by salt damage and due to freeze-thaw damage, and some of them have been removed after about 30 years of service. Moreover, a repair site can be redamaged and the damage can spread, resulting in the need to replace the RC slabs. The method for repairing a part of an RC slab when cracking has occurred or limestone has exuded from the asphalt is to remove the asphalt paving, and the part of the concrete that has degraded into aggregate is removed using a paving breaker. After removing the concrete, repair of the damaged part is carried out using a cementitious material such as an ultrarapid hardening nonshrink polymer cement mortar or ultrarapid hardening concrete. Finally, curing and waterproofing are carried out, and the asphalt paving is replaced. However, RC slabs are repaired with a thin layer of thickness of about 30 mm, so cracking is quickly caused by wheel loads

TABLE 1: Composition of repair materials.

			Unit content of water (kg/m <sup>3</sup> )	Water bonding ratio (%)
U-M-36	Mixed material	Ultrarapid hardening cement	925	36
		Calcium hydrate	13	
	Premix powder	Water reducer	2	
		Other	Acrylic polymer powder	
		Silica sand	937	
		Fiber	—	
	Water	338		
U-FM-45	Mixed material	Ultrarapid hardening cement	581	48
		Calcium hydrate	37	
	Premix powder	Water reducer	1	
		Other	Acrylic polymer	
		Silica sand	1225	
		Fiber	5	
	Water	296		

due to the difference in elastic coefficients of the RC slab concrete and the repair material. Also, there have been many examples where peeling or cracking has occurred at the boundary between the existing RC slab and the repair layer, so repair was carried out again. Therefore, there is an urgent need to develop repair materials suitable for top surface damage of RC slabs and repair techniques capable of ensuring durability, because there is a concern that new cracks may occur due to the impact of a breaker used for cutting concrete in repair work. In this study, we examined the soundness of the adhesion interface of the existing RC slabs, the adhesion strength between repair materials and existing RC slabs, and the measures to be taken with attention to the repair materials. Wheel load running tests were conducted to evaluate the fatigue resistance of the repair material used in the conventional repair method and in the repair method proposed in this research. The repair technique using repair material developed exclusively for repairing RC slabs (fiber-reinforced, ultrahard, nonshrink, and polymer cement mortar) and the two types of adhesive (penetrable primer and highly durable epoxy resin adhesive) can reinforce the fine cracks in the RC slabs and integrate the repair material and the RC slabs. The repair technique ensures long-term durability and extends the repair cycle, thereby extending the service life of the bridge.

## 2. Materials and Methods

### 2.1. Material Properties of Repair Materials

**2.1.1. Ultrarapid, Hardening, Nonshrink Polymer Cement Mortar.** In Japan, road maintenance and repair work is restricted to about 8 hours. Rapid construction is required to demolish and remove road materials, repair the road, and release traffic from regulation within 8 hours. For this reason, an ultrarapid, hardening, nonshrink polymer cement mortar is used for the partial repair of conventional RC slabs. The materials of this cementitious mixture were mainly ultrarapid hardening cement and calcium hydrate, but in

addition silica sand and water reducer were used. The curing characteristics of this repair material are as follows: initial setting time, 17 minutes; initial strength development, 45.2 N/mm<sup>2</sup> after 3 hours of aging; and static elastic modulus, 43.7 kN/mm<sup>2</sup> after 28 days of aging. Since this pot life is 30 minutes or less, prompt work is required. Note that this repair material is described as U-M-36 and is a conventional construction material. The compounding conditions are listed in Table 1. The expression intensity of U-M-36 is shown in Table 2.

### 2.1.2. Ultrahard, Fiber-Reinforced Polymer Cement Mortar.

The ultrahard, fiber-reinforced polymer cement mortar is a new repair material. The materials of this cementitious mixture were mainly ultrarapid hardening cement and calcium hydrate, but in addition silica sand, water reducer, and acrylic polymer powder were used. This repair material is called U-FM-45. The compounding conditions are listed in Table 1. This repair material was premixed with high-strength vinylon fiber (fiber length: 12 mm). By setting the elastic coefficient to about the same as that of the existing RC slabs, resistance to cracking was improved. The material properties are as follows: curing, 45 minutes at setting completion time; compressive strength at 3 hours, 24.5 N/mm<sup>2</sup>; and static elastic modulus at 28 days, 23.8 kN/mm<sup>2</sup>. Therefore, compared with the ultrafast, hard, nonshrink mortar, adequate construction time is secured and cracking of thin-layer repairs is reduced. Table 2 shows the strength development of U-FM-45, and Figure 1 shows the relationship between compressive strength and static elastic modulus.

**2.1.3. High-Durability Epoxy Resin Adhesive.** A highly durable epoxy resin adhesive (hereinafter referred to as “bonding agent for placing”) is applied to a penetrable adhesive that strengthens the adhering surface after damage. This firmly fixes the repairing material to the slab. This adhesive for adhesion was developed to help prevent fatigue in the steel deck [4, 5]. As reinforcement of the RC slab, it has been evaluated for its reinforcing effect by the bonding agent for

TABLE 2: Characteristic values of repair materials.

Test items		U-M-36	U-FM-45
Setting time	Initial setting	17 min	35 min
	Final setting	25 min	45 min
Compressive strength	2 hours	25.1 N/mm <sup>2</sup>	19.1 N/mm <sup>2</sup>
	3 hours	45.2 N/mm <sup>2</sup>	24.5 N/mm <sup>2</sup>
	4 hours	52.3 N/mm <sup>2</sup>	27.1 N/mm <sup>2</sup>
	28th	62.3 N/mm <sup>2</sup>	49.9 N/mm <sup>2</sup>
Young's modulus	28th	43.7 kN/mm <sup>2</sup>	23.8 kN/mm <sup>2</sup>

Concrete's age (Days)	Compressive strength (N/mm <sup>2</sup> )	Static elastic modulus (kN/mm <sup>2</sup> )
0.125	29	23.8
1	36.4	24.1
7	51.4	26
28	52.7	26.4

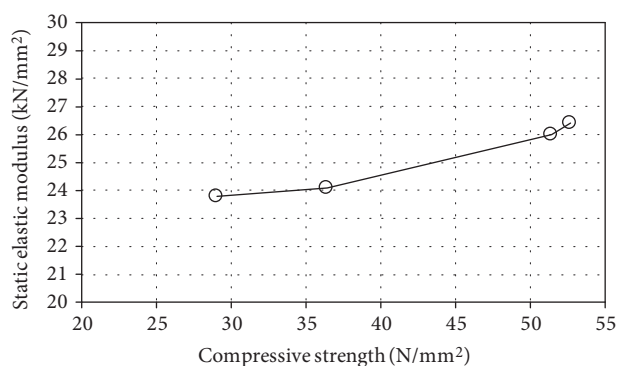


FIGURE 1: Relationship between compressive strength and static elastic modulus.

placing technique [6, 7]. An epoxy resin is a general term for a compound that contains two or more epoxides (oxiranes) in one molecule, and epoxy resin adhesives are epoxy resins in which denatured hardening agents and subsidiary materials are added and adjusted. The main features of the hardening agents used for epoxy resin adhesives and examples of typical subsidiary materials are summarized in Tables 3 and 4, respectively.

In the civil engineering field, bonding technologies using epoxy resin adhesives are applied in the precast concrete block method, in construction joints, in the steel plate bonding method, and in the CFRP bonding method. Also, the hardening agent used in these cases is almost always a polyamine type or a polyamine type combined with a polythiol (mercaptan) type. Table 5 lists the material property values of the adhesive for joining.

**2.1.4. Penetrable Adhesive.** When repairing the RC slab, a breaker is used to remove the damaged and associated fragile areas. The periphery becomes fragile due to fine cracks generated by the impact vibration of this breaker. A permeable adhesive has been developed and applied in order to reinforce the fine cracks generated by the shock vibration of this breaker [8]. This permeable adhesive was newly developed specially for the repair of RC slabs, with the viscosity adjusted so as to permeate fine cracks without using

special equipment. The penetrative adhesive was compounded using as the main component a highly durable epoxy resin adhesive developed for fresh concrete construction joints, and adjusted so that the viscosity is lowered. The material properties of the permeable adhesive are listed in Figure 1. Figure 2 shows the status of the penetration in the test specimen U-M-36 that was coated with a permeable adhesive, after destruction.

**2.2. Specification of Slab Specimen.** A 3/5-scale model of the actual bridge has the following slab dimensions: length, 1600 mm; spacing, 1400 mm; and slab thickness, 150 mm. Based on the road bridge specifications for 2002 issued by the Japan Road Association, the reinforcing bars were made of SD 295A D13 as a double reinforcing bar arrangement. Then, D13 was arranged at 120 mm intervals in the direction perpendicular to the axis of the tensile side and in the axial direction, and 1/2 of the amount of tensile reinforcement was placed on the compression side. Figure 3 shows the dimensions of the slab, the rebar arrangement map, and the wheel load running fatigue testing machine. The concrete consisted of ordinary Portland cement, crushed sand (5 mm or less), and crushed stone (5 mm to 20 mm). The compressive strength of the concrete is 35 N/mm<sup>2</sup>, the yield strength of the reinforcing bar is 377 N/mm<sup>2</sup>, and the tensile strength is 511 N/mm<sup>2</sup>.

### 2.3. Wheel Load Running Tests

**2.3.1. Wheel Load Running Test Method.** For the evaluation of fatigue resistance, the equivalent number of wheel loading cycles in a fatigue testing machine is used. In the wheel load running tests, a wheel load is repeatedly applied to the upper surface of the RC slabs and the repaired RC deck plate within a width of 300 mm for 1000 m in the axial direction. The wheel load starts traveling with an initial load of 100 kN. Loads are then added in increments of 20 kN every 20,000 runs. Deflection is measured for every 5000 runs when wheel loading runs are once, 10 times, 100 times, 1000 times, 5000 times, and more. A frame 600 mm in width and 1200 mm in length was placed around the wheel's traveling position to be filled with water. Wheel loading is performed under wet conditions after the first and second repairs. Holes 9 mm in diameter were drilled in several repair interfaces in order to observe fluctuations in the water level and check for

TABLE 3: Classification of hardening agents used for epoxy resin adhesives.

Classification	Features
Polyamine type hardening agents	Aliphatic polyamine: the reaction is fast and heat generation is remarkable. Durable to water and organic solvent. Good adhesion.
	Aliphatic polyamine: the reaction is fast and heat generation is remarkable. Durable to water and organic solvent. Good adhesion.
	Polyamide: long pot life and low cost
	Epoxy-adducted polyamine: high viscosity (useful to viscosity control).
	Mannich-modified polyamine: good to low-temperature hardening.
Catalysts	Polythiol: good to low-temperature hardening polymer network structures are looser than those of polyamine. High water adsorption. Low durability to water.
	Tertiary amine: catalyst of polyamine and as catalysts of polyamine and polyamide amine. Imidazole: reacts as hardening agents and as catalysts of anhydride hardening agents.

TABLE 4: Typical submaterials for epoxy resin adhesive.

	Classification
Additives to give functions	Aliphatic polyamine: the reaction is fast and heat generation is remarkable. Durable to water and organic solvent. Good adhesion.
Others	Pigments, dyestuff

TABLE 5: Material characteristic value of adhesive.

Test items		Penetrable adhesive	High-durability adhesive
Appearance	Base compound	Transparent liquid	White paste
	Curing agent	Transparent liquid	Blue liquid
Mixing ratio (main agent: curing agent)		10 : 3	5 : 1
Specific gravity of cured product		1.2	1.42
Compressive strength		104.4 N/mm <sup>2</sup>	102.9 N/mm <sup>2</sup>
Compressive modulus of elasticity		3172 N/mm <sup>2</sup>	3976 N/mm <sup>2</sup>
Flexural strength		92.8 N/mm <sup>2</sup>	41.6 N/mm <sup>2</sup>
Tensile shear strength		58.2 N/mm <sup>2</sup>	14.9 N/mm <sup>2</sup>
Concrete adhesion strength		2.6 N/mm <sup>2</sup>	3.7 N/mm <sup>2</sup> or more of destruction in the base material

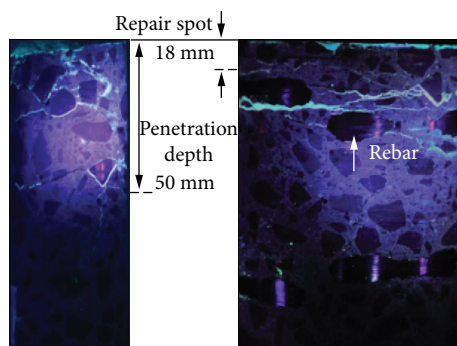


FIGURE 2: Result of permeation verification after specimen RC-U-36 destruction. (1) Diameter 50 mm. (2) Diameter 100 mm.

delamination. The specifications for the water filling is shown in Figure 4.

2.3.2. *Repair Method and Repair Cycle.* The specimen used in this experiment reproduced the damaged state in the actual

RC slab. In the place where damage such as potholes repeatedly occurred on the asphalt pavement of the RC slab, when the asphalt pavement is removed, the concrete is separated into aggregate and sand (Figure 5(a)) and is in a fragile state. This weakened area was scraped off with a breaker accompanied by striking and vibration (Figure 5(b)) and was finished into a healthy and strong surface (Figure 5(c)). This area was then repaired with an ultrarapid hardening nonshrink polymer cement mortar or ultrarapid hardening concrete agent (Figure 5(d)), and water proofing was carried out. In order to reproduce such a state, the initial loading of the slab specimen was added to reproduce the condition requiring repair. From the previous research, it was determined that repair is required when a deflection corresponding to 1/400 of the span length occurs and two-way cracking is developed on the lower surface of the slab [9–11]. The repair method was verified using a slab surface test specimen subjected to this initial loading. The experimental situation is shown in Figure 6. Using the repair material U-M-36 of the conventional construction method, a breaker was used to break the

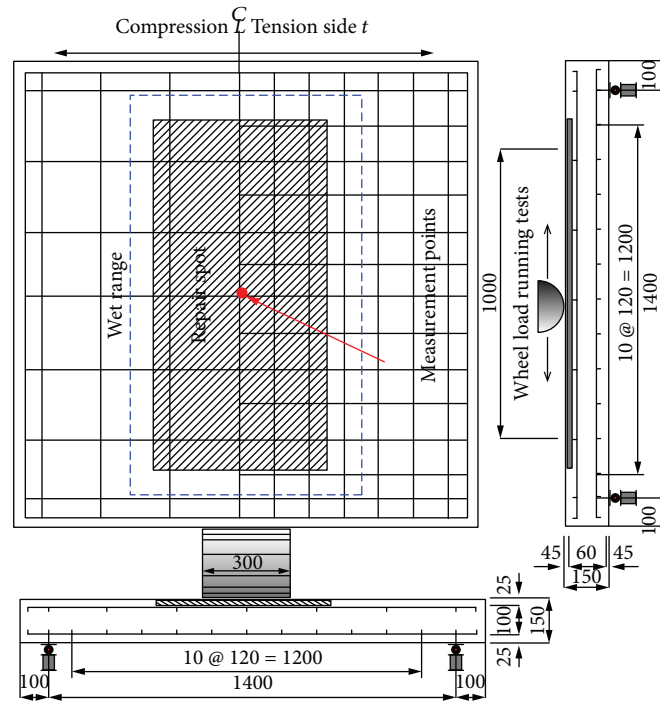


FIGURE 3: Dimensions of test specimen and plumbing diagram.

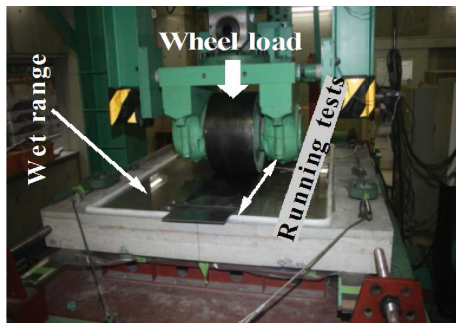


FIGURE 4: Appearance of running load fatigue testing machine and the specifications for the water filling.

repair area (Figures 6(a) and 6(b)), clean the surface, apply the repair material U-M-36, and then finish the surface. Next, in the work procedure of the repair method using the repair material U-FM-45 proposed in this research, a permeable adhesive is applied first to the adhesion interface which was scratched and cleaned, and the bonding agent for joining is repeatedly painted (Figures 6(c) and 6(d)). Then, the repair material U-FM-45 was poured onto the surface and the finish was the applied (Figure 6(e)). The cycle of repair and running wheel load tests was conducted twice under wet conditions and once under dry conditions. In the two wet-condition cycles, repair was performed when the wheel load caused unevenness or scaling or when the deflection reached  $1/400$  of the slab span  $L$ . The dry-condition cycle was performed until punching shear fracture occurred. Fatigue resistance is determined from the cumulative number of equivalent cycles obtained from these three tests.

**2.3.3. Number of Equivalent Cycles in Running Fatigue Test.** The wheel load running fatigue test uses a step load that increases every twenty thousand runs, and the equivalent running number is calculated to evaluate fatigue resistance. Assuming that the Miner's rule is applicable to the number of equivalent cycles, it is given by (1) [12]. Reference load  $P$  in (1) is set at 72 kN, which takes into consideration a safety factor of 1.2 based on  $3/5$  of the design active load, to calculate the equivalent traveling number. The value of 12.7, as proposed by Matsui, is applied to the absolute value of the reciprocal  $m$  of the slope of the SN curve.

$$N_{eq} = \sum_{i=1}^n (P_i/P)^m \times n_i. \quad (1)$$

The equation is expressed as follows:  $P_i$  is the loaded load (kN),  $P$  is the reference load (=72 kN),  $n_i$  is the number of experiment runs (times), and  $m$  is the reciprocal of the slope of the SN curve.

### 3. Results

**3.1. Number of Equivalent Cycles.** Table 6 lists the number of equivalent cycles and the reinforced equivalent running number used in this study.

**3.1.1. Specimen RC-U-36 Using Conventional Repair Material U-M-36.** The number of equivalent cycles of the initial loading is  $7.865 \times 10^6$ . With the repair material U-M-36 with wheel loading under wet conditions in the first cycle, the number of equivalent cycles in the running wheel load running tests is  $1.685 \times 10^6$ . Similarly, the number of equivalent cycles of the 2nd repair cycle is  $1.621 \times 10^6$ . The number

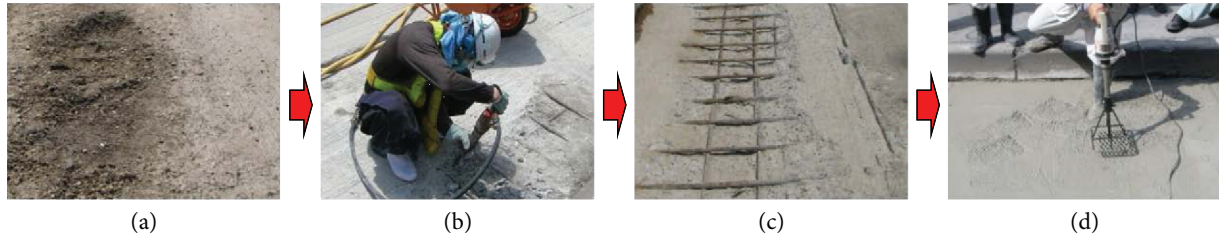


FIGURE 5: Example of thin-layer repair of upper layer of RC slab. (a) Degraded into aggregate. (b) Removal of damaged parts. (c) Removal of injured site. (d) Thin-layer repair.

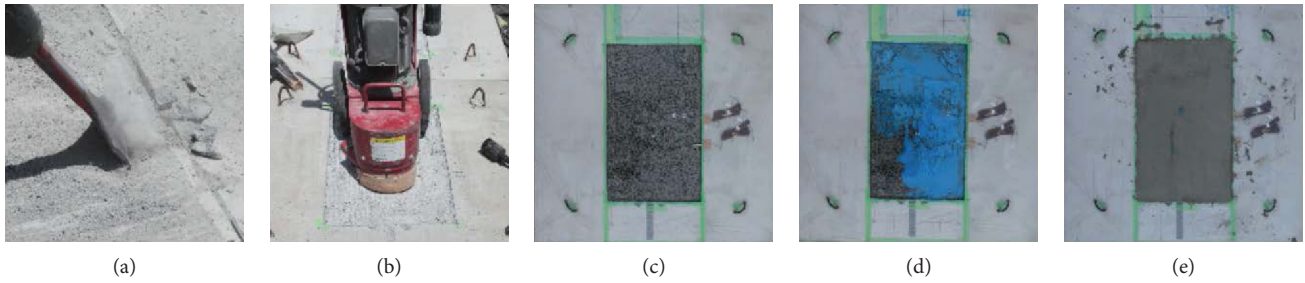


FIGURE 6: Procedure for manufacturing the RC slab specimen. (a) Removal of damaged parts. (b) Grinding of damaged parts. (c) Application of penetratable adhesive. (d) Application of bonding agent for placing. (e) Placing repair material and finish.

TABLE 6: The number of equivalent cycles and the reinforced equivalent running number used.

		RC-U-36	RC-UF-45
RC slab		7,865,598	7,865,598
Primary repair (wet state)	Equivalent runs, number of times	1,685,974	3,685,775
	Reinforcement effect	—	2.2
Secondary repair (wet state)	Equivalent runs, number of times	1,621,127	3,250,670
	Reinforcement effect	—	2.0
Tertiary repair (dry state)	Equivalent runs, number of times	10,493,077	42,350,384
	Reinforcement effect	—	4.0
Total until tertiary repair	Equivalent runs, number of times	21,665,776	57,152,427
	Reinforcement effect	—	2.64

of equivalent cycles for the third repair performed under dry conditions was  $10.493 \times 10^6$ , which resulted in punched shear failure. The cumulative number of the equivalent cycle count from 1 repair cycle to 3 repair cycles was  $21.665 \times 10^6$ , which resulted in a repair effect of 1.57 for the unrepaired slab plate. Wheel load data in Table 6 shows the number of equivalent cycles in the running wheel load running tests.

**3.1.2. Specimen RC-UM-45 Using New Repair Material U-FM.** The number of equivalent cycles of repairs using the proposed repair material U-FM and two kinds of adhesives was  $3.685 \times 10^6$  in the first cycle of repair,  $3.250 \times 10^6$  in the second cycle of repair, and  $42.35 \times 10^6$  in the third cycle. This is 2.19 times more in the first cycle under dry conditions than with the conventional repairing method, 2.01 times in the second cycle, and 11.49 times in the third cycle. Also, the cumulative number of equivalent cycles until

destruction in the 3rd cycle was  $57.152 \times 10^6$ . A reinforcement effect of 2.64 times that of the conventional construction method was obtained.

### 3.2. Relation between Deflection and Number of Equivalent Cycles

**3.2.1. Specimen RC-U-36 Using Conventional Repair Material U-M-36.** The residual deflection under initial loading was 1.42 mm. For repairs with repair material U-M-36, in the first cycle, the cumulative number of equivalent cycles is  $9.551 \times 10^6$ , the cumulative deflection is 3.44 mm, and the residual deflection is 1.96 mm. The cumulative number of equivalent cycles in repair cycle 2 is  $11.172 \times 10^6$ , the cumulative deflection is 4.10 mm, and the residual deflection is 2.74 mm. In the third repair performed under dry conditions, damage on the repair surface was suppressed. Therefore, the cumulative number of equivalent cycles is  $21.655 \times 10^6$  and

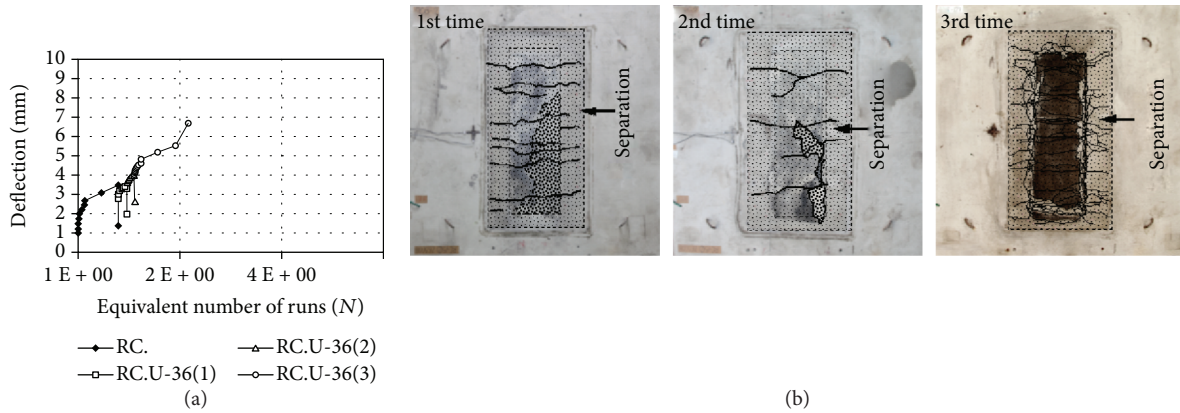


FIGURE 7: RC-U-36. (a) Relationship between deflection and number of equivalent cycles. (b) Condition of damage caused on the upper surface.

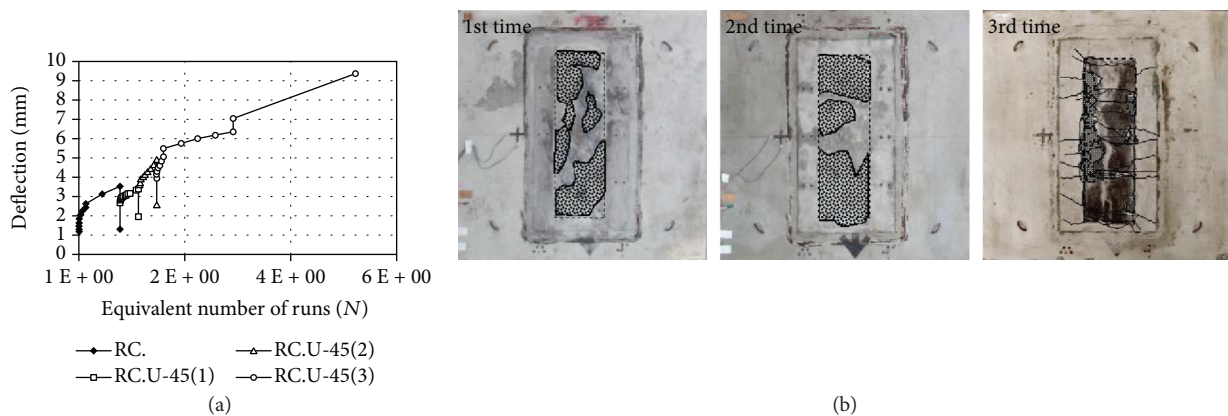


FIGURE 8: RC-U-45. (a) Relationship between deflection and number of equivalent cycles. (b) Condition of damage caused on the upper surface.

the cumulative deflection is 6.65 mm. Figure 7(a) shows the relationship between deflection and the number of equivalent cycles. Figure 7(b) shows the condition of damage caused on the upper surface.

**3.2.2. About the Slab Using the Proposed Repair Material U-FM Punching Shear Strength.** Residual deflection due to the initial loading of the proposed repair material U-FM-45 and the test specimen to which two types of adhesives are applied is 1.31 mm. The cumulative number of equivalent cycles in the first cycle of repair is  $11.551 \times 10^6$ , the cumulative deflection is 3.39 mm, and the residual deflection is 1.90 mm. Figure 8(a) shows the relationship between deflection and the number of equivalent cycles. As shown in Figure 8(a), the damaged upper surface of the specimen after the runs showed irregularities due to wear, but no cracks are observed. The cumulative number of equivalent cycles in repair cycle 2 is  $14.802 \times 10^6$ , the cumulative deflection is 4.85 mm, and the residual deflection is 2.53 mm. The only damage is the unevenness of the road surface. The cumulative number of the equivalent cycles of repair cycle 3 under dry conditions is  $57.152 \times 10^6$ , and the cumulative deflection is 9.33 mm. Since repair cycle 3 was conducted until the test specimen was destroyed by punching shear fracture, cracking occurred in the direction perpendicular to the axis on

the upper surface of the test specimen. However, the number of equivalent cycles was four times that when using the conventional reinforcement method. These results confirm that the proposed repair method provides fatigue resistance and is practical for repairs using conventional reinforcement materials.

## 4. Discussion

**4.1. Evaluation of Fatigue Resistance by the Number of Equivalent Cycles.** A higher repair effect was obtained for RC slab test specimens repaired with the repair material U-FM-45 by applying 2 types of adhesive at the top surface repair boundary of the RC slab than the repair effect for RC slab test specimens repaired with the conventional repair material U-M-36, by a factor of 2.2 for the first repair, a factor of 2 for the second repair, a factor of 4 for the third repair under dry conditions, and a factor of 2.64 at failure.

**4.2. Evaluation of Crack Resistance.** In these tests, after the deflection of the RC slab reached 1/400 of the span  $L$ , 2 cycles of repair were carried out under wet conditions and one cycle under dry conditions. After the wheel load running tests, multiple cracks were observed extending in the direction normal to the axial direction in the top surface of the slab that

was repaired using the conventional repair material U-M-36. However, on the top surface of the test specimens repaired with the repair material U-FM-45 after applying the two types of adhesive to the boundary, the number of cracks in the direction normal to the axial direction was greatly reduced compared with the repair material U-M-36, although damage due to wear could be seen on the running surface. As a result, the fatigue durability was increased.

## 5. Conclusions

In this study, we investigated countermeasure technologies presuming that redamage is caused by delamination of the adhesion interface and cracking of the repair material, further supposing that rainwater and others, intrude and induce damage. The first countermeasure technology is a permeable adhesive for strengthening the adhesion interface. The second countermeasure technology is an adhesive for fresh concrete that firmly bonds the existing repair material with the new repair material. Finally, the third is the development and application of a repair material that has an elastic modulus equivalent to that of existing slabs and further improves resistance to cracking by using resin fibers to add toughness. In this research, we proposed a repair method that combines these technologies and confirmed that the method provides much greater fatigue resistance than the conventional construction method. The repair method using the repair material U-M-45 after applying the two types of adhesive obtained the same repair effect as was verified in the tests when applied to a real bridge. Namely, the fragile concrete surface was strengthened by applying the penetrable adhesive, and the repair material was firmly bonded to the existing slab at the joint by applying the epoxy adhesive. Therefore, for repairing thin layers of RC slabs, a repair method that applies dedicated repair material for repairing the slab after application of two types of adhesive is practical.

## Data Availability

The data used to support the findings of this study are available from the corresponding author upon request.

## Conflicts of Interest

The authors declare that there is no conflict of interest regarding the publication of this paper.

## Acknowledgments

The authors are grateful for the advice from each of the engineers of Sumitomo Osaka Cement Co. Ltd and Kajima-road Co. Ltd.

## References

- [1] T. Tamakoshi, M. Okubo, and K. Ikuta, "Analysis of periodic inspection results of highway bridges in Japan," in *25th US-Japan Bridge Engineering Workshop*, pp. 61–68, Japan, 2009.
- [2] H. Nakai, S. Matsui, T. Yoda, and A. Kurita, "Trends in steel-concrete composite bridges in Japan," *Structural Engineering International*, vol. 8, no. 1, pp. 30–34, 1998.
- [3] Japan Road Association, *Specifications and commentary for road bridges I, II, III*, Yamato Planning Printing Co., Ltd., 2002.
- [4] T. Kodama, O. Kamada, M. Nishi, Y. Zuzuki, and T. Fukute, "A study of bonded concrete overlays using epoxy adhesive in Japan," in *Sixth International Conference on Maintenance and Rehabilitation of Pavements and Technological Control (MAIREPAV6)*, p. 111, Turin, Italy, 2009.
- [5] K. Ito, J. Takahagi, H. Chiba, and Y. Suzuki, "Study on a countermeasure for improving the fatigue durability of existing orthotropic steel deck plates using SFRC pavement," in *Proceedings of 5th China-Japan Workshop on Pavement Technologies (CJWPT 2009)*, pp. 221–226, China, 2009.
- [6] T. Kodama, M. Kagata, S. Higashi, K. Itoh, and Y. Ichinose, "Effect of reducing strains by SFRC pavement on Ohira Viaduct," in *Proceeding of the 25th US-Japan Bridge Engineering Workshop. Tsukuba: Public Works Research Institute 2009*, pp. 149–156, Tsukuba, Japan, 2009.
- [7] T. Abe, H. Suzuki, Y. Kishi, and K. Nomoto, "The effect of adhesive on the fatigue resistance of RC slabs strengthened by SFRC upper surface thickness increasing method," *Proceedings of Structural Engineering*, vol. 59A, pp. 1084–1091, 2013.
- [8] K. Ito, T. Abe, M. Fuchigami, N. Kozakai, and T. Kodama, "A study on fatigue durability of the top surface repair method using two types of adhesives for damaged RC slabs," in *Fourth Conference on Smart Monitoring, Assessment and Rehabilitation of Civil Structures (SMAR 2017)*, p. 144, Zürich, Switzerland, 2017.
- [9] T. Abe, T. Kida, M. Takano, and Y. Kawai, "Evaluation of the punching shear strength and fatigue resistance of road bridge RC slabs," *Journal of Japan Society of Civil Engineers, Ser. A1 (Structural Engineering & Earthquake Engineering (SE/EE))*, vol. 67, no. 1, pp. 39–54, 2011.
- [10] T. Abe, T. Kida, T. Sawano, A. Komori, and S. Hida, "Reinforcement effect and mechanical characteristics of CFS reinforced RC slabs with different number of layers," *Theoretical and Applied Mechanics Japan*, vol. 57, pp. 95–103, 2009.
- [11] M. Takano, T. Abe, T. Kida, A. Kobayashi, and A. Komori, "Fatigue characteristics of CFS-reinforced RC slabs sustaining running vibration loads and running constant loads," *Theoretical and Applied Mechanics Japan*, vol. 58, pp. 31–39, 2010.
- [12] S. Matui, "Design and construction of road bridge slabs and maintenance," *Mori Kita Publishing, Inc*, pp. 44–46, 2007.

## Research Article

# Crack Width and Load-Carrying Capacity of RC Elements Strengthened with FRP

Justas Slaitas , Mykolas Daugevičius, Juozas Valivonis, and Tatjana Grigorjeva

*Department of Reinforced Concrete Structures and Geotechnics, Vilnius Gediminas Technical University, LT-10223 Vilnius, Lithuania*

Correspondence should be addressed to Justas Slaitas; [justas.slaitas@vgtu.lt](mailto:justas.slaitas@vgtu.lt)

Received 7 March 2018; Revised 16 May 2018; Accepted 7 June 2018; Published 11 July 2018

Academic Editor: Young Hoon Kim

Copyright © 2018 Justas Slaitas et al. This is an open access article distributed under the Creative Commons Attribution License, which permits unrestricted use, distribution, and reproduction in any medium, provided the original work is properly cited.

The present study focuses on a prediction of crack width and load-carrying capacity of flexural reinforced concrete (RC) elements strengthened with fibre-reinforced polymer (FRP) reinforcements. Most studies on cracking phenomena of FRP-strengthened RC structures are directed to empirical corrections of crack-spacing formula given by design norms. Contrary to the design norms, a crack model presented in this paper is based on fracture mechanics of solids and is applied for direct calculation of flexural crack parameters. At the ultimate stage of crack propagation, the load-carrying capacity of the element is achieved; therefore, it is assumed that the load-carrying capacity can be estimated according to the ultimate crack depth (directly measuring concrete's compressive zone height). An experimental program is presented to verify the accuracy of the proposed model, taking into account anchorage and initial strain effects. The proposed analytical crack model can be used for more precise predictions of flexural crack propagation and load-carrying capacity.

## 1. Introduction

Retrofitting of existing structures is one of the main challenges for civil engineers today. One of the most advantageous material types for strengthening is fibre-reinforced polymers (FRP) due to their corrosion resistance and high strength to low weight ratio [1–5]. Anticorrosion properties are particularly relevant in aggressive environments, for example, bridge structures [6]. Strength properties could be used even more efficiently and economically by prestressing the FRP material [7, 8]. However, the effectiveness of strengthening can be compromised by loss of composite action, which can be delayed by using the additional anchorage [9]. There is a large quantity of researches made on the behaviour of the joint of concrete and FRP material [10–14], and the bond stiffness-reduction techniques are proposed [15–17], but none of the researches analysed by the authors was applied for prediction of concrete crack propagation. In accordance with design provisions [18, 19], the cracks in concrete open when a limiting tensile strain of

concrete is reached; therefore, the crack width can be calculated by multiplying the mean values of a difference between tensile reinforcement and concrete strains with crack spacing. The researchers working on cracking phenomena of FRP-strengthened structures are trying to correct the empirical formulas to calculate crack spacing given by the design norms [20–22]. A different approach is proposed in this paper, that is, a crack model for direct calculation of flexural crack parameters which neglect the crack spacing. At the ultimate stage of crack propagation, the load-carrying capacity of the element is achieved. Therefore, it is assumed that the load-carrying capacity can be estimated according to ultimate crack depth (directly measuring concrete's compressive zone height). The experimental program is presented to verify the accuracy of proposed crack propagation model, taking into account anchorage and initial strain effects. An extended database is used for comparison of numerical and experimental results of crack width under service load and load-carrying capacity of the element. In total, 98 RC beams, strengthened with externally bonded (EBR) and near

surface-mounted (NSM) carbon fibre-reinforced polymer (CFRP) and glass fibre-reinforced polymer (GFRP) sheets, plates, strips, and rods were tested. The experimental results were collected from different scientific publications.

## 2. Analytical Model

**2.1. Crack Width according to Design Standards.** In this chapter, the estimation methods of the crack width and the mean crack spacing proposed in design standards [18, 19] are presented. The crack width of a RC structure can be calculated by following equation proposed in EC2 [18].

$$w_{EC2} = s_{r,max}(\varepsilon_{sm} - \varepsilon_{cm}), \quad (1)$$

where  $s_{r,max}$  is the maximum crack spacing and  $\varepsilon_{sm}$  and  $\varepsilon_{cm}$  are the mean strains in reinforcement and in concrete between cracks, respectively.

The mean value of crack spacing can be defined as follows [18]:

$$s_{r,m} = \frac{S_{r,max}}{1.7} = 2c + \frac{0.25k_1k_2\phi}{\rho_{p,eff}}, \quad (2)$$

where  $k_1$  is a coefficient which evaluates the bond properties of the bonded reinforcement: 0.8 for high bond bars and 1.6 for bars with an effectively plain surface (e.g., prestressing tendons);  $k_2$  is a coefficient which takes into account the distribution of strain: 0.5 for bending and 1.0 for pure tension.

Assuming stabilized cracking, the characteristic value of the crack width of FRP-strengthened RC structures is calculated according to fib bulletin 14 [19] recommendations:

$$w_{FIB} = 1.7s_{r,m}\zeta\varepsilon_2, \quad (3)$$

where  $\zeta$  is a tension-stiffening coefficient and  $\varepsilon_2$  is the reinforcement strain in the fully cracked state.

The mean crack spacing, taking into account the effect of both the internal and the external reinforcement, can be calculated as [19]

$$\begin{aligned} s_{r,m} &= \frac{2f_{ctm}A_{c,eff}}{\tau_{sm}u_{s1}} \frac{E_{s1}A_{s1}}{E_{s1}A_{s1} + \xi_b E_f A_f} \\ &= \frac{2f_{ctm}A_{c,eff}}{\tau_{fm}u_f} \frac{\xi_b E_f A_f}{E_{s1}A_{s1} + \xi_b E_f A_f}, \end{aligned} \quad (4)$$

where  $f_{ctm}$  is a mean value of concrete tensile strength;  $A_{c,eff}$  is an effective area of concrete's tensile zone;  $A_{s1}$  and  $A_f$  are the areas of steel and FRP reinforcements, respectively;  $E_{s1}$  and  $E_f$  are the elasticity modules of steel and FRP reinforcements, respectively;  $u_{s1}$  and  $u_f$  are the bond perimeters of steel and FRP reinforcement, respectively;  $\tau_{sm} = 1.8f_{ctm}$  and  $\tau_{fm} = 1.25f_{ctm}$  are the mean bond stresses of steel and FRP reinforcement; and  $\xi_b$  is a bond parameter given as

$$\xi_b = \frac{\tau_{fm}E_{s1}A_{s1}u_f}{\tau_{sm}E_f A_f u_{s1}}. \quad (5)$$

Neglecting the tension-stiffening effect and initial strain, the characteristic crack width is as follows [19]:

$$w_{FIB2} = 2.1\rho_{c,eff} \frac{M_a}{E_{s1}d\rho_{eq}} \frac{1}{(u_{s1} + 0.694u_f)}, \quad (6)$$

where  $M_a$  is the acting moment in a cross-section,  $\rho_{c,eff}$  is a ratio of the effective area in tension, and  $\rho_{eq}$  is the equivalent reinforcement ratio.

Hence, a denser cracking and the smaller crack widths are obtained for RC beams strengthened with FRP; the crack widths estimated by the methodology proposed in [19] were used for further analysis.

## 2.2. Proposed Methodology

**2.2.1. Crack Width.** In accordance with Jokūbaitis and Juknevičius and Jokūbaitis et al.'s [23, 24] proposed crack development model for RC structures, a flexural reinforced concrete element crack has two peaks; one leads to the crack spread toward the beam neutral axis, and the other refers to the tensile reinforcement. The width of the crack apex closer to the neutral axis is critical for further crack spread. The bond strength of concrete and reinforcements, which is equal to the tensile strength of concrete ( $f_{ct}$ ), stresses of FRP, and steel reinforcements ( $\sigma_s$  and  $\sigma_f$ , respectively), resist crack propagation. Parts of the element separated by the crack rotates about the intersection point of the crack surface and neutral axis (see Figure 1(a)).

The proposed crack model is presented in Figure 1(a), where  $A_{s1}$ ,  $A_{s2}$ , and  $A_f$  are the inner tensile, compressive steel, and external FRP reinforcements, respectively;  $d_1$  and  $d_2$  are the distances to centroids of inner reinforcements;  $h_{cr}$  and  $h_{ct}$  are the crack depth and the depth of tensile zone above it, respectively; and  $w_{cr}$  and  $\delta_{cr}$  are the crack width and the critical width of a normal crack tip, respectively. Strain distribution in a cross-section is reflected in Figure 1(b), where  $x_e$  is a depth of compression zone of concrete;  $\varepsilon_{ctu}$  and  $\varepsilon_f$  are the ultimate tensile strain of concrete and the FRP strain, respectively. The crack depth and width dependence can be expressed from a condition of similarity of triangles:

$$\frac{\delta_{cr}}{w_{cr}} \approx \frac{h_{ct}}{h_{cr}} \approx \frac{\varepsilon_{ctu}}{\varepsilon_f}. \quad (7)$$

General expression of ultimate value of concrete's tensile strain is used for analysis:

$$\varepsilon_{ctu} = \frac{f_{ctm}}{\nu_{pl}E_{cm}} \approx \frac{2f_{ctm}}{E_{cm}}, \quad (8)$$

where  $\nu_{pl}$  is concrete plasticity factor ( $\nu_{pl} \approx 0.5$ );  $E_{cm}$  is a secant modulus of elasticity.

The mean value of concrete's tensile strength and secant modulus of elasticity are estimated in accordance with EC2 [18]:

$$\begin{aligned} f_{ctm} &= 0.30\sqrt{(f_{cm} - 8)^2}, \\ E_{cm} &= 22 \left( \frac{f_{cm}}{10} \right)^{0.3}. \end{aligned} \quad (9)$$

The ratio of ultimate strain of concrete in tension and the strain of FRP reinforcement can be calculated as follows:

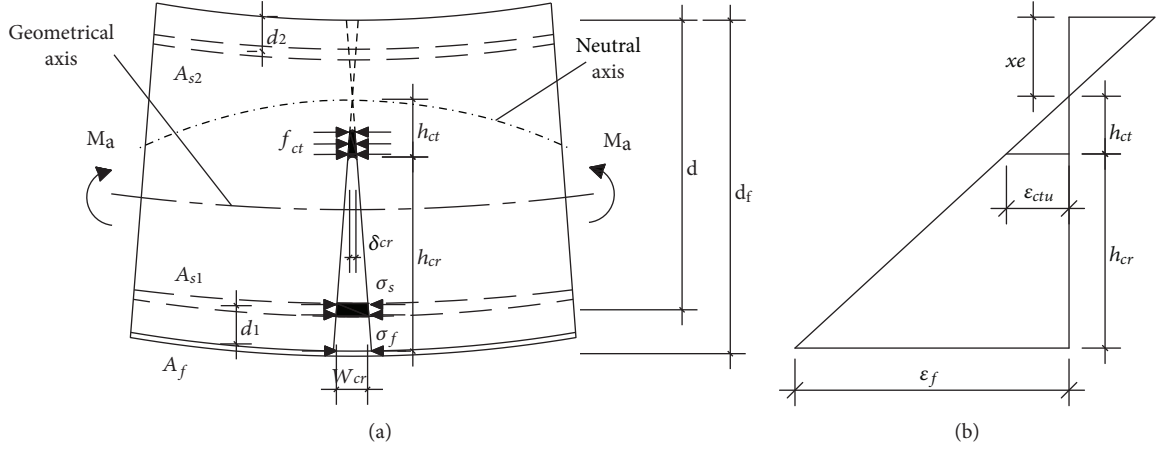


FIGURE 1: The model for calculation of normal crack propagation: (a) crack model; (b) strain distribution.

$$\frac{\epsilon_{ctu}}{\epsilon_f} \approx \frac{2f_{ctm}(\alpha_{s1}A_{s1}((d-x_e)/(d_f-x_e))(d-x_e/3) + \alpha_f A_f(d_f-x_e/3) + \alpha_{s2}A_{s2}((x_e-d_2)/(d_f-x_e))(x_e/3-d_2))}{M_a - A_f E_f (\epsilon_p - \epsilon_0)(d_f-x_e/3)}, \quad (10)$$

$$x_e = \frac{\sqrt{B_e^2 + 2(b - 2\alpha_f A_f ((M_p - M_0)/M_a x_0))(\alpha_{s2} A_{s2} d_2 + \alpha_{s1} A_{s1} d + \alpha_f A_f d_f)} - B_e}{b - 2\alpha_f A_f ((M_p - M_0)/M_a x_0)}, \quad (11)$$

$$B_e = \alpha_{s2} A_{s2} + \alpha_{s1} A_{s1} + \alpha_f A_f, \quad (12)$$

where  $\alpha_{s1}$ ,  $\alpha_{s2}$ , and  $\alpha_f$  are the ratios of elasticity modules of steel reinforcements and FRP reinforcement, respectively;  $\epsilon_p$  is the FRP prestressing strain and  $\epsilon_0$  is the initial strain;  $M_p$  and  $M_0$  are the bending moment caused by the prestressing force and the initial bending moment, respectively; and  $x_0$  is the initial depth of the concrete compressive zone.

A wide range of experimental research was conducted by Jokūbaitis et al. [23–28], and the empirical expression of the critical width of a normal crack tip was derived for flexural RC elements:

$$\delta_{cr,0} \approx 0.00012d_1^3 \sqrt{\phi} \mu, \quad (13)$$

where  $d_1$  is the distance to the tensile steel reinforcement resultant (see Figure 1),  $\phi$  is the diameter of tensile steel reinforcement, and  $\mu$  is the parameter, which evaluates the influence of different factors (cross-section, bond between concrete and reinforcement, and reinforcement ratio) on the relation between the crack parameters.

Below is the same expression with some modifications which could be used for FRP-strengthened structures:

$$\delta_{cr} \approx 0.00012d_{1,eff}^3 \sqrt{\phi_{eq}} \mu, \quad (14)$$

where  $\phi_{eq}$  is the equivalent factor of tensile zone;  $\mu$  is the parameter evaluating the influence of the cross-section of the element and bond between concrete and FRP

reinforcement (the reinforcement ratio is already taken into account estimating the equivalent factor of the tensile zone):

$$\mu = \frac{\beta \vartheta(b, h)}{\psi_f}, \quad (15)$$

where  $\beta = 2$  and  $1$  for long-term and short-term loading, respectively;  $\vartheta(b, h)$  is the empirical function of cross-sectional parameters; and  $\psi_f$  is the reduction factor of stiffness in the interface between the RC member and FRP based on the built-up-bar theory [12, 16, 17]:

$$\psi_f = 1 - \frac{\text{sh}(\lambda \cdot L_s) \cdot \text{ch}(\lambda \cdot (L/2 - L_s))}{\lambda \cdot L_s \cdot \text{ch}((\lambda \cdot L)/2)}. \quad (16)$$

Factor  $\lambda$  evaluates the stiffness of the interface and could be calculated as follows:

$$\lambda = \sqrt{\xi \cdot \gamma}. \quad (17)$$

Stiffness of the interface between separate members:

$$\xi = \frac{u_f G_{eff}}{a}, \quad (18)$$

where  $a$  is the distance between the centroids of the RC beam and FRP;  $G_{eff}$  is the effective shear modulus [12]:

$$G_{eff} = 0.001 \cdot K \cdot E_{cm}, \quad (19)$$

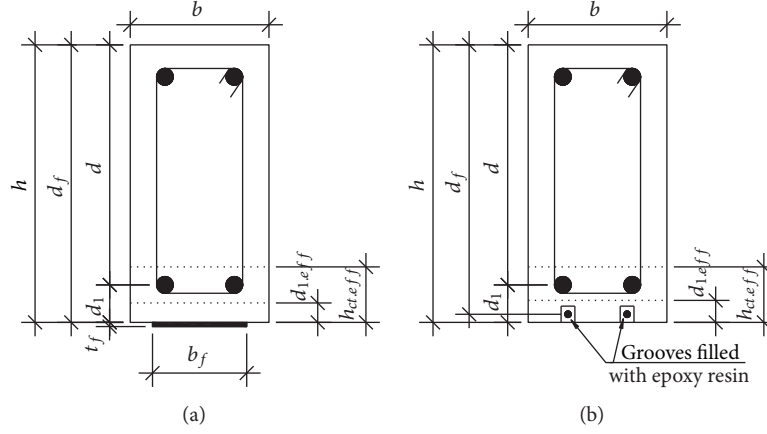


FIGURE 2: Effective tension area: (a) EBR; (b) NSM.

where  $K$  is the coefficient evaluating the anchorage of FRP.  $K = 1$  when FRP is not anchored,  $K = 1.5$  when steel plates are used for the anchorage, and  $K = 2.0$  when FRP wraps or interlocking grooves are used for the anchorage.

Factor  $\gamma$  could be calculated as follows:

$$\gamma = \frac{1}{E_{cm}A_{c,eff}} + \frac{1}{E_f A_f} + \frac{a^2}{E_{cm}I_{c,eff}}, \quad (20)$$

where  $A_{c,eff}$  and  $I_{c,eff}$  are the area and the moment of inertia of a cracked concrete cross-section, respectively. For rectangular cross-sections

$$A_{c,eff} = bx_e, \quad (21)$$

$$I_{c,eff} = \frac{bx_e^3}{3}. \quad (22)$$

The distance to tensile steel and FRP-reinforcement resultant (in mm) (see Figure 2) is as follows:

$$\begin{aligned} d_{1,eff} &= d_1 - \frac{A_f \sigma_f (d_f - d)}{A_f \sigma_f + A_{s1} \sigma_{s1}} \\ &= d_1 - \frac{A_f E_f (d_f - d)}{A_f E_f + A_{s1} E_{s1} ((d - x_e)/(d_f - x_e))}. \end{aligned} \quad (23)$$

In EC2, the effective reinforcement ratio of tensile zone of concrete is expressed as follows:

$$\rho_{t,eff} = \frac{A_{s1} + \xi_1 A_p}{A_{ct,eff}}, \quad (24)$$

where  $A_p$  is the area of pre- or posttensioned tendons within  $A_{ct,eff}$  and  $\xi_1$  is the adjusted ratio of bond strength taking into account the different diameters of prestressing and reinforcing steel.

As proposed in [21] for FRP-strengthened RC structures,  $A_p = A_f$  and  $\xi_1 = E_f/E_{s1}$ ; then the effective reinforcement ratio of the tensile zone of concrete will be as follows:

$$\rho_{t,eff} = \frac{A_{s1} + A_f E_f/E_{s1}}{A_{ct,eff}}, \quad (25)$$

where  $A_{ct,eff}$  is the effective area of concrete in tension:

$$A_{ct,eff} = bh_{ct,eff} = \min \begin{cases} 2.5bd_{1,eff}, \\ \frac{b(h - x_e)}{3}, \\ \frac{h}{2}. \end{cases} \quad (26)$$

The equivalent factor of the tensile zone, taking into account both steel and FRP reinforcements, can be derived from (2) and (4):

$$\phi_{eq} = \frac{8\rho_{t,eff}A_{ct,eff}f_{ctm}\xi_b E_f A_f}{\tau_{fm} u_f (E_s A_s + \xi_b E_f A_f) k_1 k_2}, \quad (27)$$

where the bond perimeter of FRP reinforcement  $u_f$  is determined from Figure 3.

Subsequently, the crack width is derived from (7) and (10):

$$w_{cr,f} = \frac{\delta_{cr}(M_a - A_f E_f (\varepsilon_p - \varepsilon_0)(d_f - x_e/3))}{2f_{ctm}(\alpha_{s1} A_{s1} ((d - x_e)/(d_f - x_e))(d - x_e/3) + \alpha_f A_f (d_f - x_e/3) + \alpha_{s2} A_{s2} ((x_e - d_2)/(d_f - x_e))(x_e/3 - d_2))}, \quad (28)$$

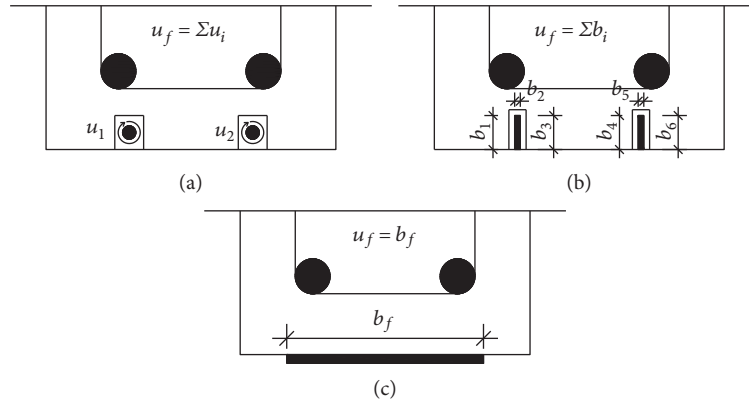


FIGURE 3: Bond perimeter of FRP reinforcement: (a) FRP rods; (b) FRP strips; (c) EBR.

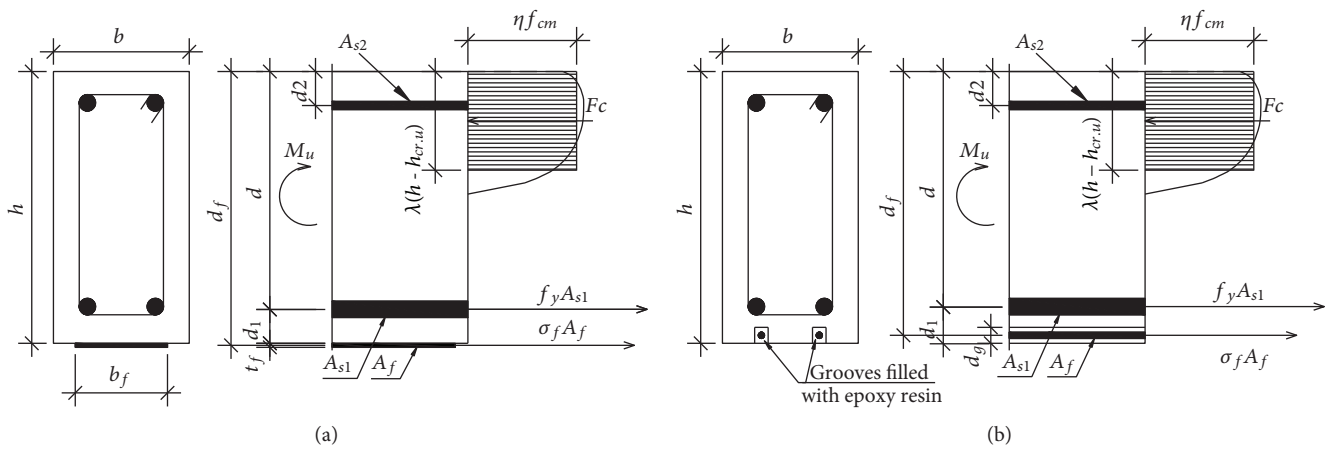


FIGURE 4: State of stress in RC beam strengthened with (a) EB FRP reinforcement and (b) NSM FRP reinforcement.

where  $d$  and  $d_f$  are the depths of inner and external reinforcements, respectively. If the structure was already cracked at the strengthening moment, the initial crack width should be added to calculation:

$$w_{cr} = w_{cr,f} + w_{cr,0} \tag{29}$$

$$w_{cr,0} = \frac{\delta_{cr,0} M_0}{2f_{ctm}(\alpha_{s1} A_{s1}(d - x_0/3) + \alpha_{s2} A_{s2}((x_0 - d_2)/(d - x_0))(x_0/3 - d_2))} \tag{30}$$

2.2.2. Relation between Crack Depth and Load-Carrying Capacity. The same relation in (7) relates the crack depth with the acting bending moment and the depth of the concrete tensile zone, whose relation with crack parameters can be expressed as follows:

$$h_{ct} \approx \frac{\delta_{cr}}{w_{cr}} h_{cr} \tag{31}$$

Furthermore, there will always be a retained condition:

$$h = h_{cr} + \frac{\delta_{cr}}{w_{cr}} h_{cr} + x_e \tag{32}$$

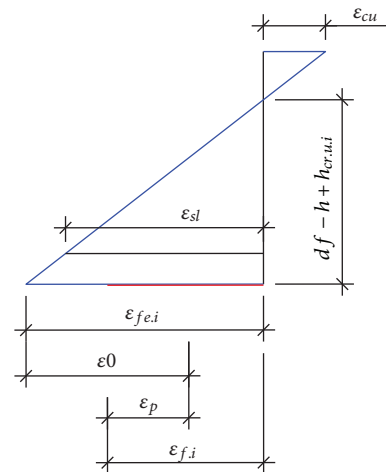


FIGURE 5: Limit state of strain in the flexural member.

Therefore, the crack depth can be expressed as follows:

$$h_{cr} = \frac{h - x_e}{1 + \delta_{cr}/w_{cr}} = \frac{h - x_e}{1 + \epsilon_{ctu}/\epsilon_f} \tag{33}$$

When the load of the RC element strengthened with FRP is close to its ultimate value, the strain in tensile steel

reinforcement, in most cases, shall exceed the yield strength and large plastic deformations will occur in the element ( $\delta_{cr}/w_{cr} \rightarrow 0$ ,  $\varepsilon_{ctu}/\varepsilon_f \rightarrow 0$ , and  $h_{ct} \rightarrow 0$ ). Therefore, the tensile zone of concrete above the crack can be disregarded, and the ultimate crack depth of the element could be evaluated according to Figure 4, by using the equivalent rectangular concrete compressive stress diagram.

Although FRP stress is unknown, the equilibrium condition between the ultimate crack depth and the FRP stress can be reached iteratively. This way, the ultimate crack depth could be evaluated by the following:

$$h_{cr.u.i} \approx h - \frac{A_{s1}f_y + A_f\sigma_{f,i}}{\eta\lambda f_{cm}b}, \quad (34)$$

where  $f_y$  and  $f_{cm}$  are the yield strength of tensile steel reinforcement and the mean value of concrete compressive strength, respectively, and  $\eta$  and  $\lambda$  are the reduction factors of concrete compressive strength and compressive zone height, respectively (in accordance with EC2 [18]:  $\eta = 1.0$ ,  $\lambda = 0.8$  for concrete strength  $f_{ck} < 50$  MPa). The FRP stress of  $i$ th iteration can be found, assuming the linear elastic stress-strain relationship, but it must be lower than the design strength:

$$\sigma_{f,i} = E_f \varepsilon_{f,i} \leq f_f, \quad (35)$$

where  $\varepsilon_{f,i}$  is a FRP strain, which could be determined from Figure 5.

In accordance with EC2 [18], the ultimate strain of the compressive concrete  $\varepsilon_{cu}$  could be taken as 3.5‰, when  $f_{ck} < 50$  MPa. Iterations are repeated until equilibrium condition is achieved:

$$\sigma_{f,n} \approx \sigma_{f,n-1}. \quad (36)$$

Afterwards, the compressive reinforcement stress is calculated and the ultimate crack depth is revised, evaluating the impact of compressive reinforcement and reduced stiffness in the interface between the RC member and the FRP reinforcement.

$$\sigma_{s2} = E_{s2}\psi_f\varepsilon_{fe} \frac{h - h_{cr.u} - d_2}{d_f - h + h_{cr.u}} \leq f_{y,s2}, \quad (37)$$

$$h_{cr.u} = h - \frac{(A_{s1}f_y + A_f\psi_f\sigma_f - A_{s2}\sigma_{s2})^2}{\eta\lambda f_{cm}b(A_{s1}f_y + A_f\psi_f\sigma_f)}, \quad (38)$$

where the reduction factor  $\psi_f$  is taken from (16), (17), (18), (19), (20), (21), and (22), only that  $A_{c,eff} = b(h - h_{cr.u})$  and  $I_{c,eff} = b(h - h_{cr.u})^3/3$ .

Real reduction coefficients of a concrete compressive zone stress diagram can be determined using the modified technique proposed by Dulinskas et al. [29] (see Figure 6).

The areas of separate parts and the whole curvilinear concrete's compressive zone diagram [30]:

$$A_{asc} = \frac{1}{2}2x_{asc} \frac{2}{3}f_{cm} = \frac{2}{3}f_{cm}(h - h_{cr.u}) \frac{\varepsilon_{c1}}{\varepsilon_{c2}}, \quad (39)$$

$$A_{desc2} = f_{cm}x_{desc} = f_{cm} \left(1 - \frac{\varepsilon_{c1}}{\varepsilon_{c2}}\right) (h - h_{cr.u}), \quad (40)$$

$$A_{desc3} = A_{sum} - A_{asc} - A_{desc2}, \quad (41)$$

$$A_{sum} = \frac{A_{s1}f_y + A_f\psi_f\sigma_f - A_{s2}\sigma_{s2}}{b}, \quad (42)$$

where the concrete strain at peak stress [18] is  $\varepsilon_{c1} = 0.7f_{cm}^{0.31} \leq 2.8$  and the concrete ultimate strain  $\varepsilon_{c2} = \varepsilon_{fe}(h - h_{cr.u})/(d_f - (h - h_{cr.u}))$ .

When  $A_{desc3} < 0$ , the descending part of concrete's compressive zone diagram exists and it is possible to calculate its parameters.

$$\lambda = \frac{2x_c}{h - h_{cr.u}} \leq 1.0, \quad (43)$$

$$\eta = \frac{A_{sum}}{f_{cm}\lambda(h - h_{cr.u})} \leq 1.0; \quad (44)$$

where  $x_c$  is a coordinate of centroid of curvilinear concrete's compressive zone stress diagram:

$$x_c = \frac{\sum A_i x_{ci}}{A_{sum}}. \quad (45)$$

If  $\varepsilon_{c2} < \varepsilon_{c1}$ , there will not be any descending part and the area of the ascending part would be equal to the area of the whole curvilinear concrete compressive zone diagram. The strength of compressive concrete will not be reached (see Figure 7), and maximum stress in the most compressed fibre can be determined by stress-strain relation for nonlinear structural analysis proposed in EC2 [18]:

$$\sigma_c = f_{cm} \frac{k\varepsilon_{c2}/\varepsilon_{c1} - (\varepsilon_{c2}/\varepsilon_{c1})^2}{1 + (k-2)(\varepsilon_{c2}/\varepsilon_{c1})}, \quad (46)$$

$$k = \frac{1.05E_c|\varepsilon_{c1}|}{f_{cm}}. \quad (47)$$

Next, the ascending part of the concrete stress diagram is divided into the simpler figures, and the parameters of equivalent stress diagram are calculated by (43) and (44).

Subsequently, the flexural strength of the strengthened member can be expressed as

$$M_{u,calc} = \eta f_{cm} b \lambda (h - h_{cr.u}) \left( h - \frac{\lambda(h - h_{cr.u})}{2} \right) + A_{s2}\sigma_{s2}(h - d_2). \quad (48)$$

A simplified methodology proposed by Slaitas et al. [31] could be used for nonstrengthened RC structures, using a triangular concrete compressive zone stress diagram.

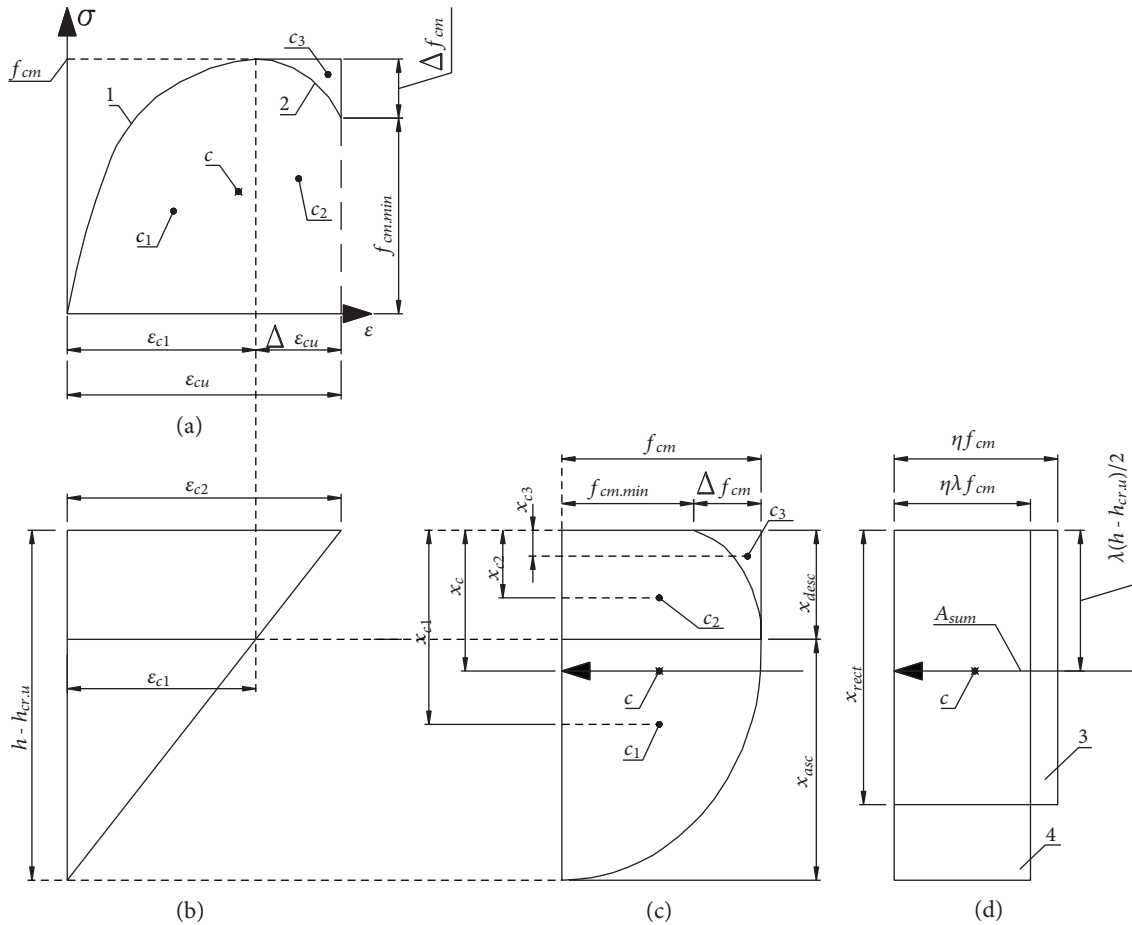


FIGURE 6: Stress distribution diagrams for concrete in compression: (a) curvilinear: 1—ascending part, 2—descending part; (b) strains in the cross-section; (c) curvilinear concrete's compressive zone stress diagram and centroids of its parts:  $c$ —whole stress diagram,  $c_1$ —ascending part,  $c_2$ —constant (rectangular) part,  $c_3$ —separated part from rectangular by curved descending line, and  $x_c$ ,  $x_{c1}$ ,  $x_{c2}$ , and  $x_{c3}$ —the coordinates of centroids of stress diagram parts; and (d) rectangular stress diagrams: 3—equivalent and 4—inequivalent [30].

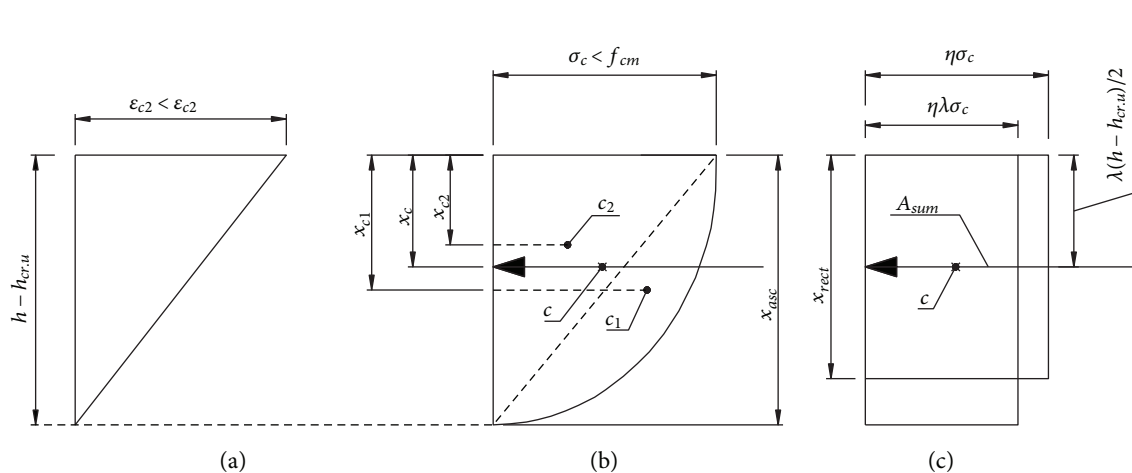


FIGURE 7: Stress distribution diagrams for concrete in compression, when mean value of concrete compressive strength is not reached: (a) strains in cross-section; (b) curvilinear concrete compressive zone stress diagram; (c) rectangular stress diagram.

The analytical model proposed above could be used for more reliable prediction of concrete crack parameters and flexural strength for FRP-strengthened RC structures.

2.3. *Analysed Beams.* Four-point bending tests were carried out on seven full-scale beams (see Figure 8). The experimental beams varied by length, material properties,

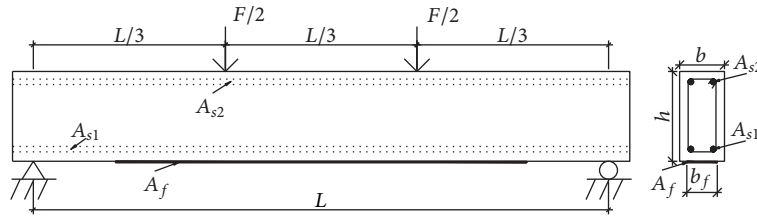


FIGURE 8: Loading scheme of tested beams.

TABLE 1: Properties of specimens and materials.

Beam ID	$b$ (m)	$h$ (m)	$L$ (m)	$A_{s1}$ (mm <sup>2</sup> )	$f_y$ (MPa)	$A_f$ (mm <sup>2</sup> )	$f_f$ (MPa)	$A_{s2}$ (mm <sup>2</sup> )	$M_0$ (kNm)	$f_{cm}$ (MPa)	Anchored
CB	0.15	0.3	2.7	308	569	—	—	226	0	25.40	—
B1-0	0.15	0.3	2.7	308	569	144	2334	226	0	25.40	Yes
B2-P*	0.15	0.3	2.7	308	569	144	2334	226	0	25.40	Yes
B3-0	0.1	0.2	1.2	226	318	16.7	4800	100	0	28.70	No
B4-0	0.1	0.2	1.2	226	318	16.7	4800	100	0	28.70	No
B5-7	0.1	0.2	1.2	226	318	16.7	4800	100	7	28.70	No
B6-7	0.1	0.2	1.2	226	318	16.7	4800	100	7	28.70	No

\*FRP was prestressed,  $\sigma_p = 120$  MPa.

TABLE 2: Properties of additional beams for serviceability stage [21].

Beam ID	$b \times h$ (mm)	$L$ (mm)	$A_{s1}$ (mm <sup>2</sup> )	$f_y$ (MPa)	$A_f$ (mm <sup>2</sup> )	$f_f$ (MPa)	$A_{s2}$ (mm <sup>2</sup> )	$M_s^*$ (kNm)	Anchored
1-A2	180 × 100	2000	157	456	16.70	3450	100	10.63	No
1-A3	180 × 100	2000	157	456	33.40	3450	100	11.90	No
1-A4	180 × 100	2000	157	456	33.40	3450	100	11.05	No
1-A5	180 × 100	2000	157	456	16.70	3450	100	12.33	No
1-A7	180 × 100	2000	157	456	16.70	3450	100	12.75	No
1-A8	180 × 100	2000	100	513	16.70	3450	157	7.86	No
1-B2	180 × 100	1800	226	432	16.70	3450	100	12.75	No
1-B3	180 × 100	1800	226	432	33.40	3450	100	12.00	No
1-B4	180 × 100	1800	226	432	33.40	3450	100	10.50	No
1-B5	180 × 100	1800	226	432	16.70	3450	100	12.75	No
1-B7	180 × 100	1800	226	432	16.70	3450	100	13.13	No
2-A2	150 × 100	1800	100	530	18.15	3450	100	4.61	No
2-A3	150 × 100	1800	100	530	18.15	3450	100	4.80	No
2-A4	150 × 100	1800	100	530	16.50	3450	100	4.91	No
2-B2	150 × 100	1800	157	570	18.15	3450	157	6.45	No
2-B3	150 × 100	1800	157	570	18.15	3450	157	6.45	No
2-B4	150 × 100	1800	157	570	33.00	3450	157	6.19	No
2-C3	100 × 150	1800	100	530	13.20	3450	100	4.46	No
2-C4	100 × 150	1800	100	530	13.20	3450	100	4.01	No
2-D3	100 × 150	1400	157	570	13.20	3450	157	7.34	No
2-E3	100 × 150	1800	314	570	33.00	3450	157	10.01	No

\*Crack width checking moment.

reinforcement ratio, and strengthening. Beam CB served as a control beam. Beams B1-0 and B2-P were strengthened, and the CFRP layer was additionally anchored with steel clumps. Beams B5-7 and B6-7 were strengthened under an external load action. Beams B3-0 and B4-0 were

strengthened without an external load action. The CFRP layer of beams B3-0, B4-0, B5-7, and B6-7 was unanchored. The properties of tested beams are listed in Table 1.

Additionally, an extended database of 27 beams total was used for comparison of numerical and experimental

TABLE 3: Properties of additional beams for load-carrying capacity.

Ref.	$A_{s1}/bd$ (%)	$f_y$ (MPa)	$A_f/bd_f$ (%)	$f_f$ (MPa)	$E_f$ (GPa)	$\sigma_p$ (MPa)	EBR/NSM
[32]	0.85	400	0.11	3100	165	1000	EBR
[32]	0.85	400	0.13 ÷ 0.14	2068	131	0 ÷ 1000	NSM
[33]	0.40	426	0.04 ÷ 0.12	2453 ÷ 3479	165 ÷ 230	0	EBR
[33]	0.40	426	0.04 ÷ 0.11	1878 ÷ 2453	121 ÷ 165	0	NSM
[34]	0.45	436	0.04 ÷ 0.22	1500 ÷ 2483	100 ÷ 167	0	NSM
[35]	0.29 ÷ 1.19	466 ÷ 501	0.08	2850	165	0 ÷ 1323	EBR
[36]	0.50 ÷ 0.75	525 ÷ 531	0.11	3263	251	0	EBR
[37]	0.58	545	0.12 ÷ 0.26	1350 ÷ 2350	64 ÷ 170	0	NSM
[38]	0.58	540	0.13 ÷ 0.26	1350 ÷ 2500	64 ÷ 170	0	NSM
[39]	0.77	475	0.08	2167	130	0 ÷ 1241	NSM
[40]	0.54 ÷ 0.94	730	0.16 ÷ 0.24	2740	159	0	NSM
[41]	0.39	585	0.06	1922	164	0 ÷ 823	NSM

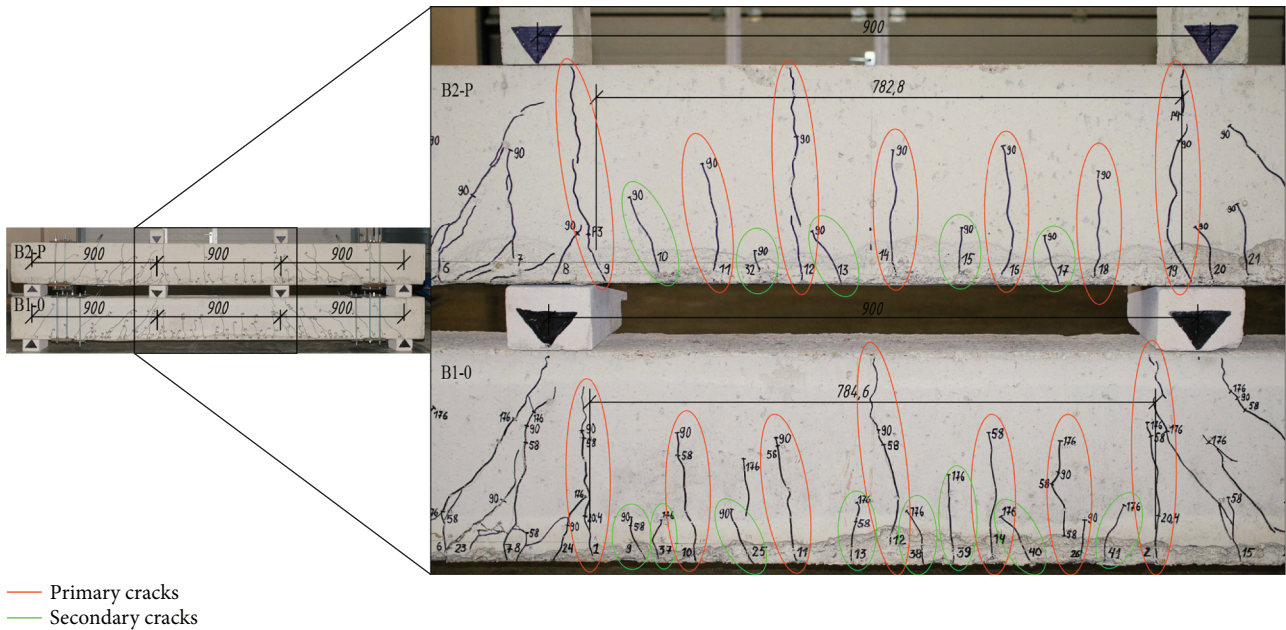


FIGURE 9: Experimental crack pattern of beams B1-0 and B2-P.

results. Additional 21 beams were taken from a research conducted in [21]. The properties of extra beams are listed in Table 2.

A number of additional RC beams, strengthened with carbon fibre-reinforced polymer (CFRP) and glass fibre-reinforced polymer (GFRP) sheets, plates, strips, and rods, tested by different researchers, were analysed in a comparison of numerical and experimental results of load-carrying capacity (sample size: 98 beams). The properties of extra 71 beams are listed in Table 3.

### 3. Results and Discussion

3.1. Crack Pattern. The crack pattern of the higher beams (B1-0 and B2-P) is presented in Figure 9. It can be seen in

both beams that the spacing of primary cracks was similar ( $s_{r.m.P.B1-0} \approx s_{r.m.P.B2-P} \approx 130$  mm), but the spacing of secondary cracks was denser in beam B1-0, although the crack widths were smaller in the prestressed beam (B2-P), taking into account secondary cracks:  $s_{r.m.P-S.B1-0} \approx 56$  mm and  $s_{r.m.P-S.B2-P} \approx 71$  mm, and crack widths under service load:  $w_{cr.B1-0} \approx 0.200$  mm and  $w_{cr.B2-P} \approx 0.075$  mm. The maximum crack width was reduced by 2.67 times by prestressing the external reinforcement. This was evaluated in the proposed method (calculated crack width of B1-0 was 2.55 times bigger than B2-P).

The crack pattern of smaller beams (B3-0, B4-0, B5-7, and B6-7) is presented in Figure 10.

In beams without initial strain, the crack distribution was denser, because from the start the beams had higher

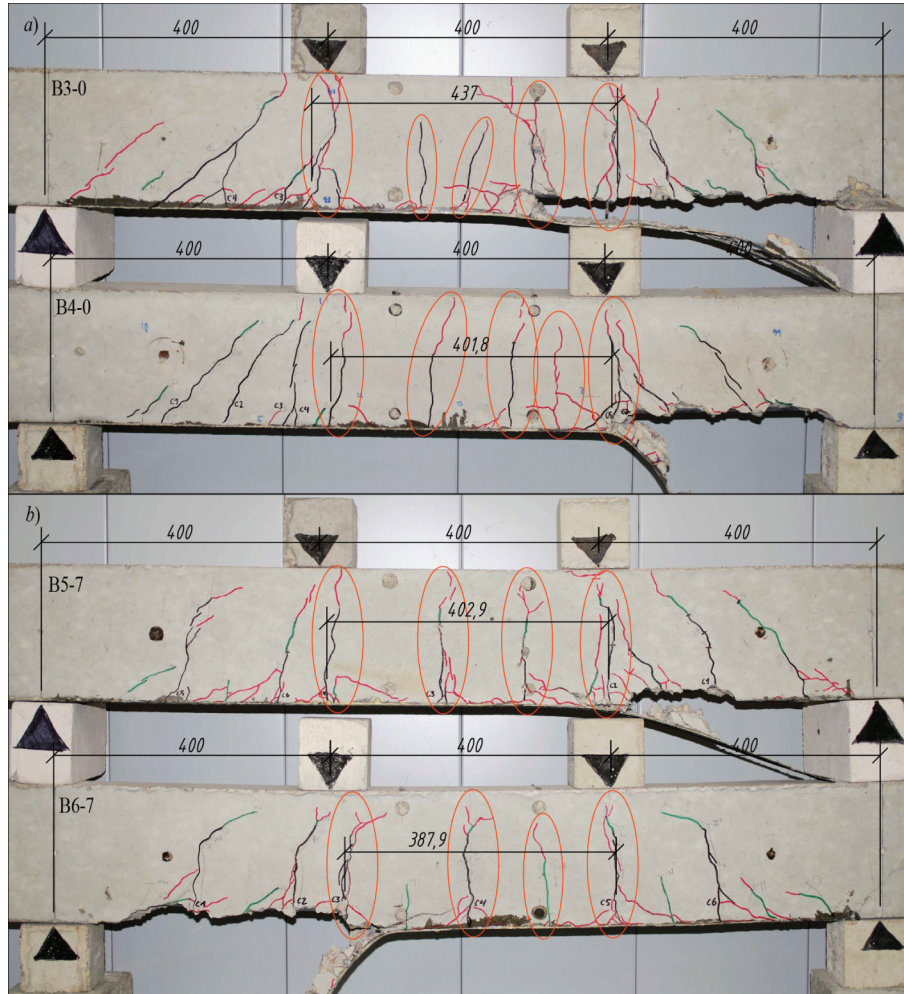


FIGURE 10: Experimental crack pattern of beams B3-0, B4-0, B5-7, and B6-7.

reinforcement ratios. Until the strengthening moment, the beams B5-7 and B6-7 were acting as ordinary RC beams and the primary cracks had already developed; after strengthening, the crack development was slower, but the spacing remained the same as earlier; that is, the distribution and propagation of cracks are different if the stiffness of beams at the moment of strengthening is different. As a result, crack widths of the beams strengthened under external load action (B5-7, B6-7) were 2 times higher than those strengthened without it (B3-0, B4-0). This validates the evaluation of the initial crack width in (29).

It should be mentioned that in smaller beams, mainly primary cracks were developing and the absence of anchorage has led to the horizontal cracks in the contact zone of concrete and FRP, which appeared when the external load has reached about 80% of the load-carrying capacity. The failure result of these beams was concrete cover separation.

**3.2. Function of Cross-Sectional Parameters.** The function of cross-sectional parameters  $\vartheta(b, h)$  in (15) could be expressed as a polynomial of the ratio of width and height

for a rectangular cross-section (as it has only these 2 parameters):

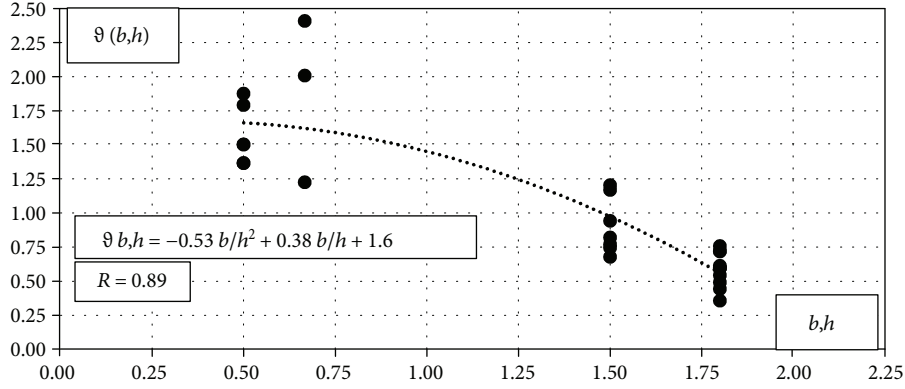
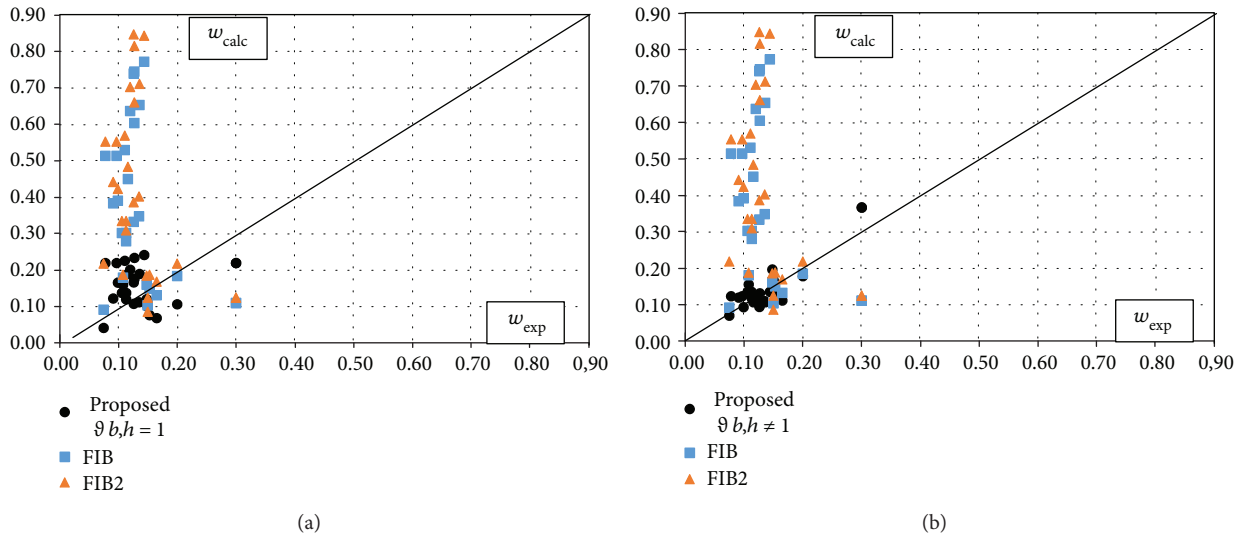
$$\vartheta(b, h) = C_1 \left(\frac{b}{h}\right)^2 + C_2 \left(\frac{b}{h}\right) + C_3, \quad (49)$$

where  $C_1$ ,  $C_2$ , and  $C_3$  are constant values, which could be determined empirically from Figure 11.

The constants  $C_1$ ,  $C_2$ , and  $C_3$  in (49) could be determined from Figure 11, and the values of the function  $\vartheta(b, h)$  could be calculated by the following expression (coefficient of correlation 0.89):

$$\vartheta(b, h) = -0.53 \left(\frac{b}{h}\right)^2 + 0.38 \left(\frac{b}{h}\right) + 1.6. \quad (50)$$

**3.3. Crack Width.** The comparison of experimental and numerical results of the crack widths is presented in Figure 12 and Table 4. The statistical parameters are shown in Table 4:


 FIGURE 11: The function of cross-sectional parameters  $\vartheta(b, h)$ .

 FIGURE 12: Comparison of the crack width estimation results with experimental ones at service load: (a)  $\vartheta(b, h) = 1$ ; (b)  $\vartheta(b, h)$  from (50).

$$\begin{aligned}
 x_i &= \frac{w_{\text{exp},i}}{w_{\text{calc},i}}, \\
 \bar{x} &= \frac{1}{n} \sum_{i=1}^n x_i, \\
 s &= \sqrt{\frac{1}{n-1} \sum_{i=1}^n (x_i - \bar{x})^2}, \\
 c_v &= \frac{s}{\bar{x}} \cdot 100\%, \\
 c_i &= \bar{x} \pm 1.96 \left( \frac{s}{\sqrt{n}} \right).
 \end{aligned} \tag{51}$$

Crack widths calculated by design provisions while evaluating the tension-stiffening effect and without it were overestimated with up to 85% (mean 32%) and 86% (mean 40%) errors ( $\Delta = (1 - w_{\text{exp}}/w_{\text{calc}}) \cdot 100\%$ ), respectively. Besides, the coefficient of variation was very high, over 100%; its scatter is 2 times higher than in the proposed method by the authors without evaluation of the influence of cross-sectional parameters and 5 times higher with it. Moreover, the proposed

TABLE 4: Statistical parameters of crack width estimation.

	$w_{\text{calc}}$ (Eq. (29), $\vartheta(b, h) = 1$ )	$w_{\text{calc}}$ (Eq. (29), $\vartheta(b, h)$ Eq. (50))	$w_{\text{FIB}}$ (Eq. (3))	$w_{\text{FIB2}}$ (Eq. (6))
$\bar{x}$	1.03	1.00	0.68	0.60
$s$	0.53	0.22	0.70	0.64
$c_v$ (%)	51.44	21.62	103.59	107.50
$c_i$	0.83, ..., 1.23	0.92, ..., 1.08	0.41, ..., 0.95	0.36, ..., 0.84

method in comparison with the design norms had a low average error (3%, 0%), low standard deviation (0.53 and 0.22), and low coefficient of variation (51.44% and 21.62%), which led to the much better confidence intervals ( $c_i$ ). It means that the FRP-strengthened RC elements could be designed with more rational cross-sections and reinforcement ratios if the proposed methodology is being used.

**3.4. Load-Carrying Capacity.** Generally, the numerical calculations of the load-carrying capacity without reduction

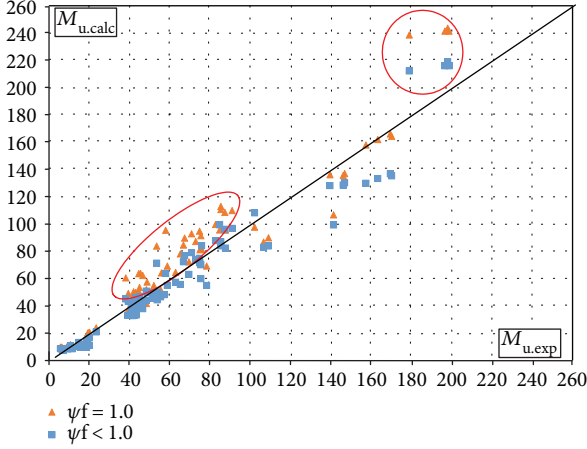


FIGURE 13: Comparison of experimental and numerical results of load-carrying capacity.

of FRP stress (due to the slippage between concrete and FRP,  $\psi_f = 1.0$ ) had lower mean error (0% to 14%) but higher scatter (coefficient of variation  $c_v$ , 24.07% to 20.84%). However, it should be noted that in some cases, the beams actually failed at loads close to 60% of the calculated ones (marked red in Figure 13) which is critically unsafe. Thus, it is vital to choose the correct calculation method. The main statistical parameters of the analysis are presented in Table 5.

The statistical parameters in Table 5:

$$\begin{aligned}
 x_i &= \frac{M_{u,exp,i}}{M_{u,calc,i}}, \\
 \bar{x} &= \frac{1}{n} \sum_{i=1}^n x_i, \\
 s &= \sqrt{\frac{1}{n-1} \sum_{i=1}^n (x_i - \bar{x})^2}, \\
 c_v &= \frac{s}{\bar{x}} \cdot 100\%, \\
 c_i &= \bar{x} \pm 1.96 \left( \frac{s}{\sqrt{n}} \right).
 \end{aligned} \tag{52}$$

The analysis of experimental and numerical results proves that this calculation method allows the accurate evaluation of the load-carrying capacity of the normal section of flexural RC beams strengthened with FRP.

The proposed calculation method could be treated as appropriate for practical application when choosing the most effective strengthening material and when determining the crack width and load-carrying capacity of the strengthened member.

#### 4. Conclusions

A crack width propagation and load-carrying capacity prediction model was presented in this paper. The conclusions

TABLE 5: Statistical parameters of load-carrying capacity.

	$M_{u,calc}$ (Eq. (48), $\psi_f = 1.0$ )	$M_{u,calc}$ (Eq. (48), $\psi_f < 1.0$ )
$\bar{x}$	1.00	1.14
$s$	0.24	0.24
$c_v$ (%)	24.07	20.84
$c_i$	0.95, ..., 1.05	1.09, ..., 1.19

of the analysis of experimental and numerical results are presented below.

- (i) The crack width calculation techniques proposed in the design recommendations overestimate the crack width with up to 86% (average 32% and 40%) error and very high scatter (coefficient of variation more than 100%).
- (ii) The predicted crack widths by the proposed model agreed very well with experimental results (with 0% average error and a rather low coefficient of variation: 21.62%), even for beams without additional anchorage and with initial strain (common situation in practice).
- (iii) The crack propagation analysis revealed that prestressing of the strengthening material reduced the maximum crack width 2.67 times. This was evaluated in the proposed calculation method (calculated crack width of the non-prestressed beam was 2.55 times bigger than that of the prestressed one).
- (iv) The propagation of cracks differs if the stiffness of the beams at the moment of strengthening is different. In the beams strengthened under external load action (with initial strain), the cracks had developed as in RC beams. After strengthening, further development of the cracks has slowed down, but the spacing remained the same. As a result, the crack widths of the beams strengthened under external load action (B5-7, B6-7) were 2 times higher than those strengthened without it (B3-0, B4-0). This validates the evaluation of the initial crack width in (29).
- (v) The results of numerical calculations of the load-carrying capacity without reduction of FRP stress (due to the slippage between concrete and FRP,  $\psi_f = 1.0$ ) had lower mean error (0% comparing to 14%) but higher scatter (coefficient of variation  $c_v$  equals to 24.07% and 20.84%, resp.) than those with it. However, it should be noted that in some cases, the beams actually failed at loads close to 60% of the calculated ones which is critically unsafe. Thus, a calculation method with reduced FRP stress and a rather low (average 14%) reserve could be treated as appropriate for the practical application when choosing the most effective strengthening material and when determining the load-carrying capacity of strengthened member.

## Data Availability

All data and results of a research are provided in the manuscript.

## Conflicts of Interest

The authors declare that there is no conflict of interest regarding the publication of this paper.

## References

- [1] C. E. Bakis, L. C. Bank, V. L. Brown et al., "Fiber-reinforced polymer composites for construction—state-of-the-art review," *Journal of Composites for Construction*, vol. 6, no. 2, pp. 73–87, 2002.
- [2] J. Valivonis, M. Budvytis, M. Atutis, E. Atutis, and L. Juknevičius, "Study on shear resistance of fiber-reinforced polymer-reinforced concrete beams," *Advances in Mechanical Engineering*, vol. 7, no. 7, 2015.
- [3] M. Panjehpour, N. Farzadnia, R. Demirboga, and A. A. A. Ali, "Behavior of high-strength concrete cylinders repaired with CFRP sheets," *Journal of Civil Engineering and Management*, vol. 22, no. 1, pp. 56–64, 2015.
- [4] L. Torres, I. A. Sharaky, C. Barris, and M. Baena, "Experimental study of the influence of adhesive properties and bond length on the bond behaviour of NSM FRP bars in concrete," *Journal of Civil Engineering and Management*, vol. 22, no. 6, pp. 808–817, 2016.
- [5] M. Aktas and Y. Sumer, "Nonlinear finite element analysis of damaged and strengthened reinforced concrete beams," *Journal of Civil Engineering and Management*, vol. 20, no. 2, pp. 201–210, 2014.
- [6] T. Skuturna, J. Valivonis, P. Vainiunas, G. Marciukaitis, and M. Daugevicius, "Analysis of deflections of bridge girders strengthened by carbon fibre reinforcement," *The Baltic Journal of Road and Bridge Engineering*, vol. 3, no. 3, pp. 145–151, 2008.
- [7] M. Atutis, J. Valivonis, and E. Atutis, "Analysis of serviceability limit state of GFRP prestressed concrete beams," *Composite Structures*, vol. 134, pp. 450–459, 2015.
- [8] Y. J. Kim, M. F. Green, and R. Gordon Wight, "Prestressed fiber-reinforced polymer (FRP) composites for concrete structures in flexure: fundamentals to applications," in *Advanced Composites in Bridge Construction and Repair*, Y. J. Kim, Ed., pp. 30–60, Woodhead Publishing, 2014.
- [9] T. Skuturna and J. Valivonis, "Experimental study on the effect of anchorage systems on RC beams strengthened using FRP," *Composites Part B Engineering*, vol. 91, pp. 283–290, 2016.
- [10] S. T. Smith and J. G. Teng, "FRP-strengthened RC beams. I: review of debonding strength models," *Engineering Structures*, vol. 24, no. 4, pp. 385–395, 2002.
- [11] J. G. Teng, S. T. Smith, J. Yao, and J. F. Chen, "Intermediate crack-induced debonding in RC beams and slabs," *Construction and Building Materials*, vol. 17, no. 6-7, pp. 447–462, 2003.
- [12] J. Valivonis and G. Marčiukaitis, "Technological-structural peculiarities of reinforced concrete structures strengthened with carbon fiber-reinforced polymer," *Technological and Economic Development of Economy*, vol. 12, no. 2, pp. 77–83, 2006.
- [13] G. Marchukaitis, Y. Valivonis, and J. Bareishis, "An analysis of the joint operation of a CFRP concrete in flexural elements," *Mechanics of Composite Materials*, vol. 43, no. 5, pp. 467–478, 2007.
- [14] M. Daugevicius, J. Valivonis, and G. Marciukaitis, "Deflection analysis of reinforced concrete beams strengthened with carbon fibre reinforced polymer under long-term load action," *Journal of Zhejiang University SCIENCE A*, vol. 13, no. 8, pp. 571–583, 2012.
- [15] J. Valivonis and T. Skuturna, "Cracking and strength of reinforced concrete structures in flexure strengthened with carbon fibre laminates," *Journal of Civil Engineering and Management*, vol. 13, no. 4, pp. 317–323, 2007.
- [16] T. Skuturna, *Research of flexural reinforced concrete members strengthened with external carbon fibre*, PhD Thesis, Vilnius Gediminas Technical University, Lithuania, 2009.
- [17] T. Skuturna and J. Valivonis, "Design method for calculating load-carrying capacity of reinforced concrete beams strengthened with external FRP," *Construction and Building Materials*, vol. 50, pp. 577–583, 2014.
- [18] EN 1992-1-1:2004, "Eurocode 2: Design of concrete structure—part 1-1: general rules and rules for buildings," *European standard*, European Committee for Standardization (CEN), 2004.
- [19] Fib bulletin 14, "Externally bonded FRP reinforcement for RC structures," Technical report, 2001.
- [20] C. Miàs, L. Torres, M. Guadagnini, and A. Turon, "Short and long-term cracking behaviour of GFRP reinforced concrete beams," *Composites Part B: Engineering*, vol. 77, pp. 223–231, 2015.
- [21] F. Ceroni and M. Pecce, "Design provisions for crack spacing and width in RC elements externally bonded with FRP," *Composites: Part B*, vol. 40, no. 1, pp. 17–28, 2009.
- [22] M. Zomorodian, G. Yang, A. Belarbi, and A. Ayoub, "Cracking behavior and crack width predictions of FRP strengthened RC members under tension," *Engineering Structures*, vol. 125, pp. 313–324, 2016.
- [23] V. Jokūbaitis and L. Juknevičius, "Critical depth of normal cracks in reinforced concrete beams of rectangular cross-section," *Journal of Civil Engineering and Management*, vol. 19, no. 4, pp. 583–590, 2013.
- [24] V. Jokūbaitis, L. Juknevičius, and R. Šalna, "Conditions for failure of normal section in flexural reinforced concrete beams of rectangular cross-section," *Procedia Engineering*, vol. 57, pp. 466–472, 2013.
- [25] V. Jokūbaitis and Z. Kamaitis, *Gelžbetoninių konstrukcijų pleišėjimas ir remontas [Cracking and repair of reinforced concrete structures]*, p. 156, Technika, Vilnius, Lithuania, 2000.
- [26] V. Jokūbaitis, *Statybinių medžiagų ir konstrukcijų irimo mechanikos pagrindai [Basics of fracture mechanics of building materials and constructions]*, p. 92, Technika, Vilnius, Lithuania, 2001.
- [27] V. Jokūbaitis, "Peculiarities of methods for calculation of normal crack width in reinforced concrete members," in *Selected Papers of Conference "Statybinės konstrukcijos"*, vol. 6, pp. 73–84, Vilnius, Lithuania, February 2009.
- [28] V. Jokūbaitis and L. Juknevičius, "Gelžbetoninių konstrukcijų normalinių plyšių pločio skaičiavimo metodų analizė—Analysis of methods for calculating the width of normal cracks in reinforced concrete structures," *Statybinės konstrukcijos ir technologijos*, vol. 1, no. 1, pp. 23–29, 2009.

- [29] E. Dulinskas, D. Zabulionis, and R. Balevičius, “A composition of equivalent compressive stress diagrams for strength analysis of flexural reinforced concrete elements,” in *Selected Papers of Conference “Statybinės konstrukcijos”*, vol. 6, pp. 5–11, Vilnius, Lithuania, February 2009.
- [30] J. Slaitas, J. Valivonis, L. Juknevičius, and R. Šalna, “Load-bearing capacity of flexural reinforced concrete members strengthened with fiber-reinforced polymer in fracture stage,” *Advances in Mechanical Engineering*, vol. 10, no. 5, 2018.
- [31] J. Slaitas, Z. Hlavac, and A. Šneideris, “Flexural reinforced concrete elements normal section bearing capacity evaluation in fracture stage,” *Engineering Structures and Technologies*, vol. 9, no. 2, pp. 70–78, 2017.
- [32] H. Peng, J. Zhang, C. S. Cai, and Y. Liu, “An experimental study on reinforced concrete beams strengthened with prestressed near surface mounted CFRP strips,” *Engineering Structures*, vol. 79, pp. 222–233, 2014.
- [33] W.-T. Jung, Y.-H. Park, J.-S. Park, J.-Y. Kang, and Y.-J. You, “Experimental investigation on flexural behavior of RC beams strengthened by NSM CFRP reinforcements,” in *SP-230: 7th International Symposium on Fiber-Reinforced (FRP) Polymer Reinforcement for Concrete Structure*, pp. 795–806, Kansas City, Missouri, November 2005.
- [34] W. T. Jung, J. S. Park, J. Y. Kang, and M. S. Keum, “Flexural behavior of concrete beam strengthened by near-surface mounted CFRP reinforcement using equivalent section model,” *Advances in Materials Science and Engineering*, vol. 2017, Article ID 9180624, 16 pages, 2017.
- [35] S. K. Woo, J. W. Nam, J. H. J. Kim, S. H. Han, and K. J. Byun, “Suggestion of flexural capacity evaluation and prediction of prestressed CFRP strengthened design,” *Engineering Structures*, vol. 30, no. 12, pp. 3751–3763, 2008.
- [36] B. Fu, G. M. Chen, and J. G. Teng, “Mitigation of intermediate crack debonding in FRP-plated RC beams using FRP U-jackets,” *Composite Structures*, vol. 176, pp. 883–897, 2017.
- [37] I. A. Sharaky, L. Torres, J. Comas, and C. Barris, “Flexural response of reinforced concrete (RC) beams strengthened with near surface mounted (NSM) fibre reinforced polymer (FRP) bars,” *Composite Structures*, vol. 109, pp. 8–22, 2014.
- [38] I. A. Sharaky, L. Torres, and H. E. M. Sallam, “Experimental and analytical investigation into the flexural performance of RC beams with partially and fully bonded NSM FRP bars/strips,” *Composite Structures*, vol. 122, pp. 113–126, 2015.
- [39] R. El-Hacha and M. Gaafar, “Flexural strengthening of reinforced concrete beams using prestressed, near-surface-mounted CFRP bars,” *PCI Journal*, vol. 56, no. 4, pp. 134–151, 2011.
- [40] J. A. O. Barros and A. S. Fortes, “Flexural strengthening of concrete beams with CFRP laminates bonded into slits,” *Cement and Concrete Composites*, vol. 27, no. 4, pp. 471–480, 2005.
- [41] M. Rezazadeh, I. Costa, and J. Barros, “Influence of prestress level on NSM CFRP laminates for the flexural strengthening of RC beams,” *Composite Structures*, vol. 116, pp. 489–500, 2014.

## Research Article

# Experimental and Numerical Study on the Compression Behavior of Square Concrete-Filled Steel Tube Stub Columns with Steel Fiber-Reinforced High-Strength Concrete

Hyung-Suk Jung <sup>1</sup>, Baek-Il Bae <sup>2</sup>, Hyun-Ki Choi <sup>3</sup>, Joo-Hong Chung,<sup>4</sup> Chang-Sik Choi,<sup>5</sup> and Yun-Cheul Choi <sup>6</sup>

<sup>1</sup>Department of Architectural Engineering, Catholic Kwandong University, Gangneung, Gangwon-do, Republic of Korea

<sup>2</sup>Research Institute of Industrial Science, Hanyang University, Seoul, Republic of Korea

<sup>3</sup>Department Fire and Disaster Prevention Engineering, Kyungnam University, Changwon, Gyeongsangnam-do, Republic of Korea

<sup>4</sup>Department of Architecture, Sahmyook University, Seoul, Republic of Korea

<sup>5</sup>Department of Architectural Engineering, Hanyang University, Seoul, Republic of Korea

<sup>6</sup>Department of Architectural Engineering, Chungwoon University, Incheon, Republic of Korea

Correspondence should be addressed to Yun-Cheul Choi; 21ycchoi@chungwoon.ac.kr

Received 3 March 2018; Accepted 22 April 2018; Published 11 June 2018

Academic Editor: Aamer Bhutta

Copyright © 2018 Hyung-Suk Jung et al. This is an open access article distributed under the Creative Commons Attribution License, which permits unrestricted use, distribution, and reproduction in any medium, provided the original work is properly cited.

This study was conducted to evaluate the applicability of concrete-filled steel tube (CFT) columns made from high-performance construction materials. KBC2016, South Korea's current building code, limits the maximum compressive strength of concrete at 70 MPa and the maximum yield strength of steel at 650 MPa. Similar restrictions to material properties are imposed on major composite structural design parameters in other countries worldwide. With the recent acceleration of the pace of development in the field of material technology, the compressive strength of commercial concrete has been greatly improved and the problem of low tensile strength, known to be the major limitation of concrete, is being successfully addressed by adding fiber reinforcement to concrete. Therefore, the focus of this study was to experimentally determine the strength and ductility enhancement effects, which depend on material composition. To this end, we performed concentric axial loading tests on CFT stub columns made from steel with a yield strength of 800 MPa and steel fiber-reinforced high-strength concrete. By measuring the strain at the yield point of CFT steel during the test, we could determine whether steel yields earlier than ultimate failure load of the member, which is a key design concept of composite structures. The analysis results revealed that the yield point of steel preceded that of concrete on the stress-strain curve by the concurrent action of the strain increase at the maximum strength, attributable to the high compressive strength and steel fiber reinforcement, and the strain increase induced by the confining stress of the steel tube. Additionally, we performed parametric study using ABAQUS to establish the broad applications of CFT using high-performance materials, with the width-to-thickness ratio as the main parameter. Parametric study was undertaken as experimental investigation was not feasible, and we reviewed the criteria for limiting the width-to-thickness ratio as specified in the current building code.

## 1. Introduction

In line with the continuous trend toward high-rise buildings and long-span structures, it is becoming increasingly necessary to develop high-strength and high-performance materials. Development of high-performance construction materials is an essential factor enabling the construction industry to build ultrahigh buildings and ultra-long-span

structures and can contribute to fundamentally solving the issue of securing usable floor space, caused by increased member sizes. In particular, for ultrahigh buildings requiring vertical members with large cross-sections, high-performance materials can allow this cross-section to be reduced. This is reflected in the recent trend of column cross-section design for large-scale structures based on the use of high-performance materials and increasing

demand for composite cross-sections designed to maximize material performance.

However, current design codes [1–4] prescribe the upper and lower limits of material strength in the design of composite members, as well as systems combining structural steel and steel-reinforced concrete. This can be ascribed to the conservatism of design codes, which basically apply conservative requirements and criteria on the basis of various research reports when evaluating untested design elements [5–10]. The reason for such restrictions on material strengths is the change in strain at the maximum strength when the compressive strength of concrete exceeds 70 MPa in the ultimate strength calculation, according to existing research results. Furthermore, a maximum allowable yield strength is applied to members subjected to compressive loads to reflect the difficulty of inducing the yield of steel before that of concrete at a design yield strength exceeding 650 MPa. In cases where the material strength levels deviate from those of the test results from previous studies as reviewed by the building code, it is recommended to ensure security through separate testing or to reduce the design yield strength and compressive strength to the imposed limits. To err on the side of safety, it is general practice to opt for the latter method; however, this approach is tantamount to losing the advantages gained by using high-performance materials as described above. In order to leverage the advantages of high-performance materials, it is therefore of paramount importance to perform experiments to test the actual effects of high-performance materials when their strengths exceed the maximum strength allowed by the building code. This is especially important for high-strength steel, given the necessity to use it along with high-strength concrete (HSC) to enhance the performance of the compressive strength of concrete.

The major problem associated with the use of high-strength steel for rectangular CFT is the strain capacity of concrete. In general, the strain capacity of concrete in CFT is greatly enhanced owing to the enlarged confinement zone in concrete compared with steel-reinforced concrete. According to EC2 [11], however, as the compressive strength of concrete increases, the local strain in specific sections decreases during maximum strength development, which may make it difficult to apply CFT to HSC.

There has been continuous research into steel-reinforced concrete since its development in the 1960s [12], and it is now a common construction material. The ultimate failure of concrete subjected to uniaxial compression is caused not only by compressive stress but also by cracks triggered by lateral expansion under compressive loads. In this process, steel fiber-reinforced concrete contributes to increasing the initial strength of crack generation by tensile force, whereas HSC contributes to preventing spalling through high density owing to the crosslinking effect of steel fiber [13–16].

With this background, this study was conducted to investigate the applicability of HSC for high-strength steel rectangular CFT. The study aimed to evaluate the possible contribution of steel fiber reinforcement to solving the problem of insufficient strain capacity of concrete that may result from the use of HSC. To this end, we performed experiments

on rectangular CFT stub columns made from high-performance materials. Additionally, finite element analysis was performed to investigate the effect of CFT using high-performance materials depending on the width-to-thickness ratio, which is one of the important factors by which the yield strength is influenced in the design standards.

## 2. Limitation of Material Strength and Axial Strength according to Code Provisions

According to South Korea's current building code (KBC 2016) [1], the compressive strength of CFT columns can be calculated from the flexural buckling limit state depending on the slenderness ratio. Specification for Structural Steel Buildings of the American National Standards Institute (ANSI/AISC 360-16) [3] also sets forth an approach to calculating the strength of members taking account of the slenderness ratio. Specifically, when the ratio of the strength of section to the elastic critical buckling load, which represents the slenderness ratio of the member, is less than or equal to 2.25, (2) is used to calculate the compressive strength, and if it exceeds 2.25, (3) is to be used. This is identical to the calculation method presented in KBC 2016. For noncompact sections, the compressive strength of composite columns is to be calculated in two categories of local buckling and its absence. For slender members, since the slenderness of steel is determined by the width-to-thickness ratio, the compressive strength of the section is to be calculated according to the slenderness ratio of each component part.

The strength of compact sections, whose width-to-thickness ratio is smaller than  $2.26\sqrt{E/F_y}$ , is to be calculated using

$$P_{n0} = P_p = A_s F_y + A_{sr} F_{yr} + 0.85 A_c f_{ck}, \quad (1)$$

where  $P_{n0}$  is the nominal axial compressive strength of the section ( $N$ ),  $P_p$  is the superimposed strength of the section ( $N$ ),  $F_y$  is the yield strength of steel (MPa),  $A_s$  is the area of steel cross section ( $\text{mm}^2$ ),  $f_{ck}$  is the compressive strength of concrete (MPa),  $A_c$  is the area of concrete cross section ( $\text{mm}^2$ ),  $A_{sr}$  is the area of continuous rebar ( $\text{mm}^2$ ), and  $F_{yr}$  is the yield strength of the rebar (MPa).

The strength of the noncompact section, whose width-to-thickness ratio falls within the range of  $3.00\sqrt{E/F_y}$  and  $5.00\sqrt{E/F_y}$ , is to be calculated using

$$P_{n0} = P_p - \frac{P_p - P_y}{(\lambda_r - \lambda_p)} (\lambda - \lambda_p)^2, \quad (2)$$

where  $\lambda$  is the slenderness ratio of the element,  $\lambda_p$  is the limiting width-to-thickness parameter for compact element ( $2.26\sqrt{E/F_y}$ ),  $\lambda_r$  is the limiting width-to-thickness parameter for noncompact element ( $3.00\sqrt{E/F_y}$ ).  $P_y$  denotes the axial yield strength of the column ( $N$ ) and is to be calculated using

$$P_y = F_y A_s + 0.7f'_c \left( A_c + A_{sr} \frac{E_s}{E_c} \right), \quad (3)$$

where  $E_s$  and  $E_c$  denote the moduli of elasticity (MPa) of steel and concrete, respectively.

The nominal strength of the slender section, whose width-to-thickness ratio exceeds  $3.00\sqrt{E/F_y}$  (lower limit) and smaller than or equal to  $5.00\sqrt{E/F_y}$  (upper limit), is to be calculated using

$$P_{n0} = F_{cr} A_s + 0.7f'_c \left( \frac{E_s}{E_c} \right), \quad (4)$$

where  $F_{cr}$  is the critical stress, which is determined as follows in case of a rectangular cross-section:

$$F_{cr} = \frac{9E_s}{(b/t)^2}, \quad (5)$$

where  $b$  is the width of element exposed to compression (mm) and  $t$  is the thickness of plate (mm).

A strength reduction factor of 0.75 is to be applied and the percentage of steel in the total cross-sectional area must exceed 1%.

It was found that the same limits are applied to concrete compressive strength in KBC2016 [1] and ANSI/AISC 360-16 [3]: the lower and upper limits are 21 MPa and 70 MPa, respectively, for normal-weight concrete, and the upper limit for lightweight concrete is 42 MPa. As for the yield strength of steel, however, the two codes set forth different upper limits: KBC2016 [1] prescribes the design yield strength of structural steel used for calculating the strength of composite columns not to exceed 650 MPa and ANSI/AISC 360-16 [3] limits the maximum yield strength of structural steel and steel reinforcement to 525 MPa and 550 MPa, respectively.

### 3. Compression Test of Rectangular CFT Stub Columns Using High-Performance Materials

**3.1. Experiment Design.** To determine the applicability of rectangular CFT made from high-performance materials in view of the provisions of the design codes as reviewed above, compression testing was performed on rectangular CFT columns made from high-performance materials. A total of eight experiments were performed, with the compressive strength of concrete, type of steel, and content level of steel fiber as independent variables. The specifications of the specimens are shown in Figure 1, and those of each variable are outlined in Table 1.

Two types of steel that differed in yield strength, SM490 and HSB800, were used to evaluate the effect of enhanced yield strength on the compressive strength development. The design compressive strength of HSC was set at 100 MPa, and ultra-high-strength concrete (UHSC) implementing the concept of reactive powder concrete (RPC) was fabricated in an attempt to induce a compressive strength development exceeding 100 MPa [17]. Table 2 presents the concrete blending ratios for fabricating the test specimens. As steel fiber reinforcement, we used straight

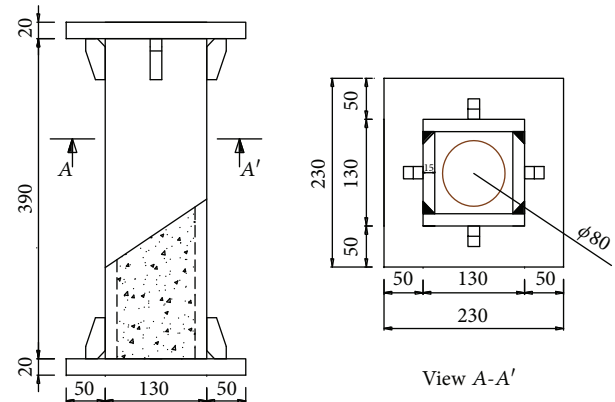


FIGURE 1: Details of test specimens.

TABLE 1: Variables and details of test specimens.

Specimen	$b/t$	$f'_c$ (MPa)	$F_y$ (MPa)	Partial concrete strength ( $\chi$ )	$P_{cal}$
HS-800	6.7	0	879	NA	5472
CS-800-3	6.7	30	879	0.05	5725
CS-800-10	6.7	102	879	0.14	6328
CS-800-F10	6.7	102	879	0.14	6328
HS-490	6.7	0	360	NA	2165
CS-490-3	6.7	30	360	0.11	2418
CS-490-10	6.7	102	360	0.29	3024
CS-490-F10	6.7	102	360	0.29	3024

$b$ : width of column section;  $t$ : thickness of steel;  $f'_c$ : compressive strength of concrete;  $F_y$ : yield strength of steel;  $\chi = (A_c f'_c)/(A_s F_y)$ ;  $A_c$ : sectional area of concrete;  $A_s$ : sectional area of steel;  $P_{cal}$ : calculated strength of test specimen based on KBC2016.

brass-coated fibers (13 mm length and 0.2 mm diameter) with a tensile strength of 2600 MPa, mixing them at a 2% volume ratio normally applied to UHSC. A hollow rectangular steel tube specimen was additionally fabricated for each steel type in order to determine the effect of concrete filling on strength enhancement. We applied additional reinforcement to the end parts of the specimens to prevent early failure at both ends during buckling. For the HSB800 steel, specially designed welding rods were used.

**3.2. Material Test.** The main objective of this study was to evaluate the applicability of high-performance materials. Therefore, it is important to define the properties of the high-performance materials used. To this end, we performed tests on each of the steel and concrete materials to be used for the compression test. The experiments on the mechanical properties of steel were carried out in compliance with KS B 0801 and 0802 [18, 19]. Specifically, in order to investigate the increase in compressive strength and tensile strength induced by mixing steel fibers into HSC, we measured experimentally the compressive strength, splitting tensile strength, and flexural tensile strength among the mechanical properties of concrete, in compliance with the test methods stipulated in KS F 2405 [20], KS F 2423 [21], and JCI-S-001 [22], respectively.

TABLE 2: Mix proportions of concrete.

ID	W/B (HSC) W/C (NSC) (%)	C	W	SF	Unit weight (kg/m <sup>3</sup> )				
					S	F	G	SP	StfF
3	0.25	809	222	80	1052	162		3.01	
10/F10	63.2	348	220		1065		666	2.85	157 (100F)

W/B: water binder ratio; W/C: water cement ratio; C: cement; W: water; SF: silica fume; S: fine aggregated; F: filler; G: coarse aggregate; SP: super plasticizer; StfF: steel fiber (volume fraction %).

TABLE 3: Mechanical properties of steel.

Steel	$F_y$ (MPa)	$F_u$ (MPa)	$F_y/F_u$	Elongation (%)
HSB800	879	944	0.93	22
SM490	360	506	0.70	26

$F_y$ : yield strength of steel;  $F_u$ : ultimate strength of steel.

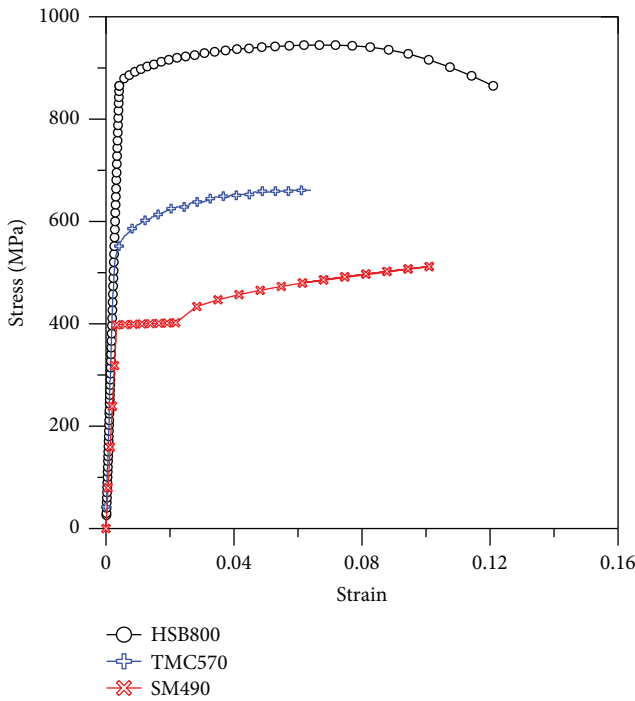


FIGURE 2: Stress-strain relation of steel.

The results of the tests on steel types used in the experiments are outlined in Table 3. The stress-strain relationship of the high-strength steel HSB800 was compared with that of SM490 and SM570TMC, and the results are plotted in Figure 2. As shown in Figure 2, steel HSB800 is no-yield-point steel, that is, it does not show any clear yield point as does SM570TMC steel, and has a higher yield ratio than SM490. Consequently, its yield strength was calculated using the 0.2% offset method used for defining the yield strength of typical high-strength steel.

Table 4 outlines the measurement results of the compressive strength, splitting tensile strength, and flexural tensile strength of concrete. Specifically, the results of compression

TABLE 4: Mechanical properties of concrete.

ID	$E_c$	$f'_c$ (MPa)	$f_{sp}$	$f_r$	Remarks
10	36233	102.38	7.86	11.54	No fiber
F10	38099	104.87	10.50	16.50	$V_f = 2.0\%$

$f'_c$ : compressive strength tested according to KS F 2405;  $f_{sp}$ : splitting strength tested according to KS F 2423;  $f_r$ : flexural tensile strength tested according to JCI-S-001-2003.

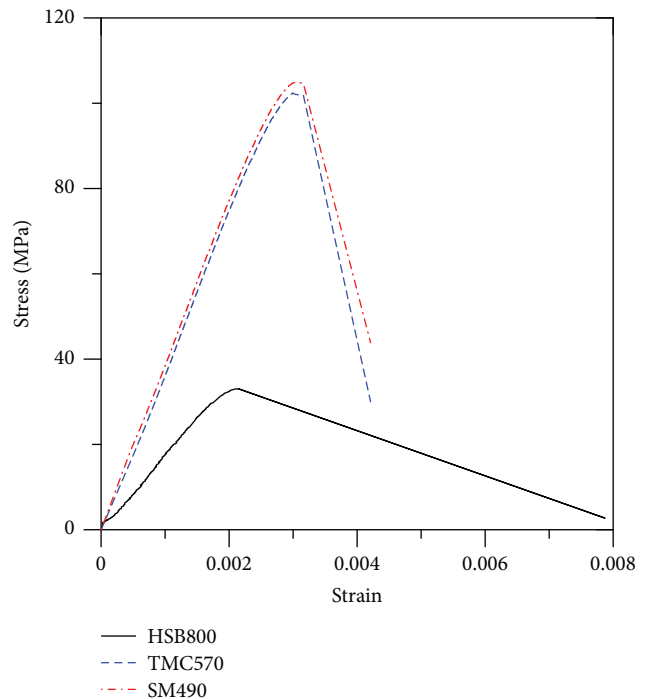


FIGURE 3: Stress-strain relation of concrete.

test are expressed by the stress-strain relationship as plotted in Figure 3. Three matrices were used in total. In the concrete matrix with a compressive strength of 30 MPa, generally classified as ordinary strength concrete, the load supporting capacity was found to decrease slowly without occurrence of any sudden decrease in load supporting capacity after the maximum strength development. In contrast, HSC was observed to lose the entire load supporting capacity due to spalling which occurred concurrently with the maximum strength development. However, no spalling appeared when



FIGURE 4: Test setup.

HSC was reinforced by steel fibers; although the load supporting capacity was considerably reduced after the maximum strength was reached, a complete loss did not occur. It was also found that the steel fiber reinforcement contributed to increasing the splitting tensile strength and flexural tensile strength by a factor of 1.33 and 1.42, respectively, when compared with the specimens not reinforced by steel fiber.

**3.3. Test Setup and Measurement Plan.** For the experiments, we used a universal testing machine (UTM) with a capacity of 10000 kN, taking account the axial strength of the specimens. Experiments were carried out in the form of uniaxial compression testing of each specimen. Figure 4 shows the test setup of the specimens. The load acting on the specimen was obtained with the load cell of the UTM, and the values of the vertical displacement at the top of the specimen and the lateral expansion at the center were obtained using linear variable differential transformer (LVDT) sensors. Strain gauges were installed at the center part to obtain the strain of the steel. The measurement plan is outlined in Figure 5.

## 4. Test Results and Discussion

Figure 6 illustrates the failure modes of the specimens at each load increment. All specimens (HS-800, HS-490, CS-800 series, and CS-490 series) went through the same pattern of failure modes. The load increased from the initial elastic slope up to the postyielding strain hardening zone and then decreased with the onset of local buckling. Ultimately, the load on the specimen decreased sharply with the onset of weld fracture. In all four specimens, no weld fracture was observed until the ultimate strength was reached. Figure 6 shows the specimens after the completion of the experiments [23].

The composite section of the HSB800 CFT stub column tested does not undergo fracture unlike brittle materials due to the effect of its perfectly plastic stress-strain behavior ( $b/t = 6.7 < \lambda_{p,HSB800} = 17$ ). Accordingly, the yield strength was determined by the 1/3 stiffness method, tangential method, and 0.2% offset method for the efficient analysis of the test results. The three yield strength determination methods are presented in Figure 7. Of them, the 1/3 stiffness method was regarded as being most appropriate from the safety point of view and was used for calculating the yield strength of the members and

the analysis of the experimental results. Table 5 outlines the yield strengths of the specimens obtained using these three methods.

**4.1. Load-Displacement Relation.** The load-displacement relations are plotted in Figure 8. The load-displacement curves were used for calculating the maximum strength. All three specimens with composite sections (CS-800-3, CS-800-10, and CS-800-F10) showed an approximately 10% increase in strength when compared with the hollow steel tube specimen (HS-800). However, they showed no significant intergroup differences in the load-displacement relations. This is assumed to be the result of the small ratio of contribution of the steel-governed composite section to strength due to the width-to-thickness ratio and material strength. However, with regard to the material strength composition, it was found that the high-strength steel section did not show any significant differences in strength at a width-to-thickness ratio of 6.7 regardless of whether filled with low-strength concrete (LSC) or HSC. In other words, in the case of high-strength steel CFT, it is not necessary to fill the tube with HSC because it demonstrates the same strength enhancement effect when filled with LSC. This finding is based on a small width-to-thickness ratio and is not enough for drawing general conclusions.

CS-490 series specimens showed different patterns of load-displacement relations depending on the concrete strength. The CS-490-F10 specimen exhibited superior values compared with other specimens in both strength and strain, demonstrating that the strength of the steel fibers mixed into concrete contributes to enhancing its strength and strain. These results lead to the assumption that the ratio of contribution of concrete to the strength is higher than that of CS-800 series specimens in such a way that concrete contributed to the strength enhancement. Table 5 outlines the initial stiffness, yield strength, and ultimate strength of each specimen and their respective displacements.

**4.2. Effect of High-Strength Concrete.** As a result of comparing the yield strength and ultimate strength increase rates among all specimens depending on the concrete type, as presented in Table 5 and based on the load-displacement relations, the combination of HSB800 and HSC showed a higher increase rate in the yield strength in comparison with the combination of HSB800 and LSC. The same result was obtained when SM490 was used. In the ultimate strength, however, a higher strength increase rate was demonstrated by the combination of HSB800 and LSC compared with the combination of HSB800 and HSC. This is assumed to be ascribable to the decrease in the effect of confinement with the increase in concrete compressive strength, as demonstrated by earlier studies on the confinement effect of HSC [23–26]. In both steel types, HSC800 and SM490, the increase rate of strain capacity from the onset of yield of the member to the ultimate state was found to be similar regardless of whether the steel was combined with LSC or HSC.

**4.3. Effect of Steel Fiber.** In an attempt to solve the problems of HSC-inherent brittle fracture behavior and strain

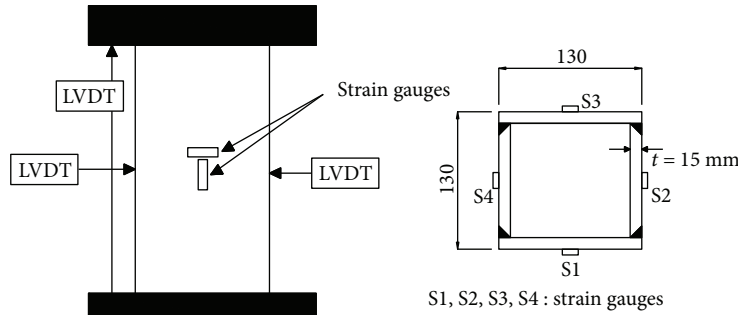


FIGURE 5: Measurement plan.

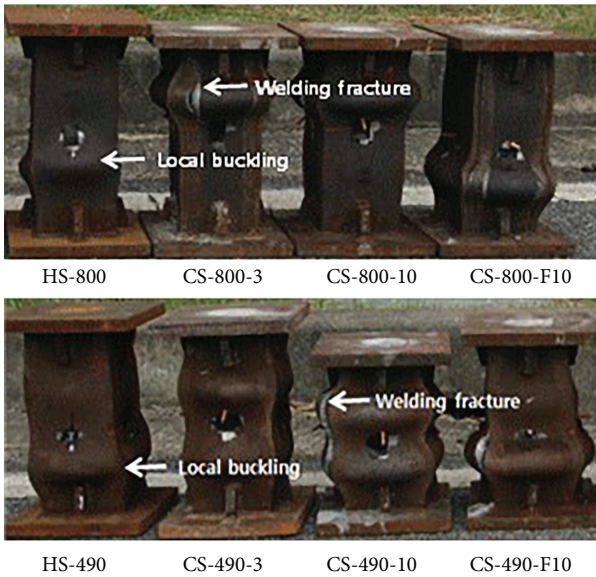


FIGURE 6: Failure of test specimens.

decrease at the maximum strength, we performed experiments on steel fiber-reinforced specimens. As shown in Figure 3, the strain was found to increase at the maximum strength. HSC specimens did not show any significant strength enhancement in both steel types despite the steel fiber reinforcement. In the case of the ultimate strength, however, SM490 exhibited a higher increase rate after the steel fiber reinforcement. On the other hand, the displacement ratio of the ultimate strength to the yield strength was found to increase after steel fiber reinforcement.

**4.4. Change of Failure Pattern.** The steel tube used for the specimen fabrication was a 15 mm-thick panel with a small cross-sectional area (130 mm); that is, the composite section of the CFT stub column tends to show steel-governed behavior. Drawing on this, on the assumption that the steel tube part hardly undergoes any change in strength regardless of whether it is filled with concrete or not on the composite section of steel tube and concrete, the value obtained by subtracting the pure strength of the steel tube from the strength of the composite section was defined as the strength under concrete confinement.

As explained in the introduction, the reason for limiting the material strength in the current building code is to enable a design that induces the exterior steel tube to yield earlier than the compression fracture of core concrete. If high-strength steel is used, concrete failure can occur first depending on the strain rate. This is not desirable from a safety point of view and is therefore a point that must be checked when designing HSB800 steel composite members. Given the nature of concrete that increased strength and confinement bring about increase in maximum strain, the strain of the core concrete under confinement explained in the preceding section was indirectly measured and compared with the steel tube strain in order to examine the yield pattern, that is, whether the steel tube yields first. As shown in Figure 9, the maximum strain of the core concrete was found to grow larger than that of the HSC-filled steel tube. This result deviates from the EC2 model, in which the maximum strain decreases as the concrete compressive strength increases, and may be explained by the comparatively low modulus of elasticity of the HSC used in this study, which was fabricated according to the RPC concept. This confirmed the possibility of maintaining the pattern of earlier steel yield complying with the conventional design concept of filling the steel tube with RPC-based 100 MPa concrete. Additionally, as could be confirmed from steel fiber-reinforced material tests, the strain exhibited a higher value at the maximum strength. This is another factor conducive to inducing the earlier yield of steel. From these findings, it may be concluded that rectangular CFTs made from high-strength steel may find safe applications in construction sites when combined with high-strength fiber-reinforced concrete.

## 5. Finite Element Analysis of Test Specimens and Parametric Study

As mentioned above in Section 4, the CFT-related effect of concrete could not be clearly demonstrated due to the material properties and the limitations of the test equipment [23]. Therefore, we performed numerical analysis to investigate the width-/thickness-dependent behavior changes of the CFT made from high-performance materials, using the commercial finite element analysis (FEA) program ABAQUS [27]. The adequacy of the FEA was tested by comparing the numerical and experimental results obtained in this study, followed by parametric analysis.

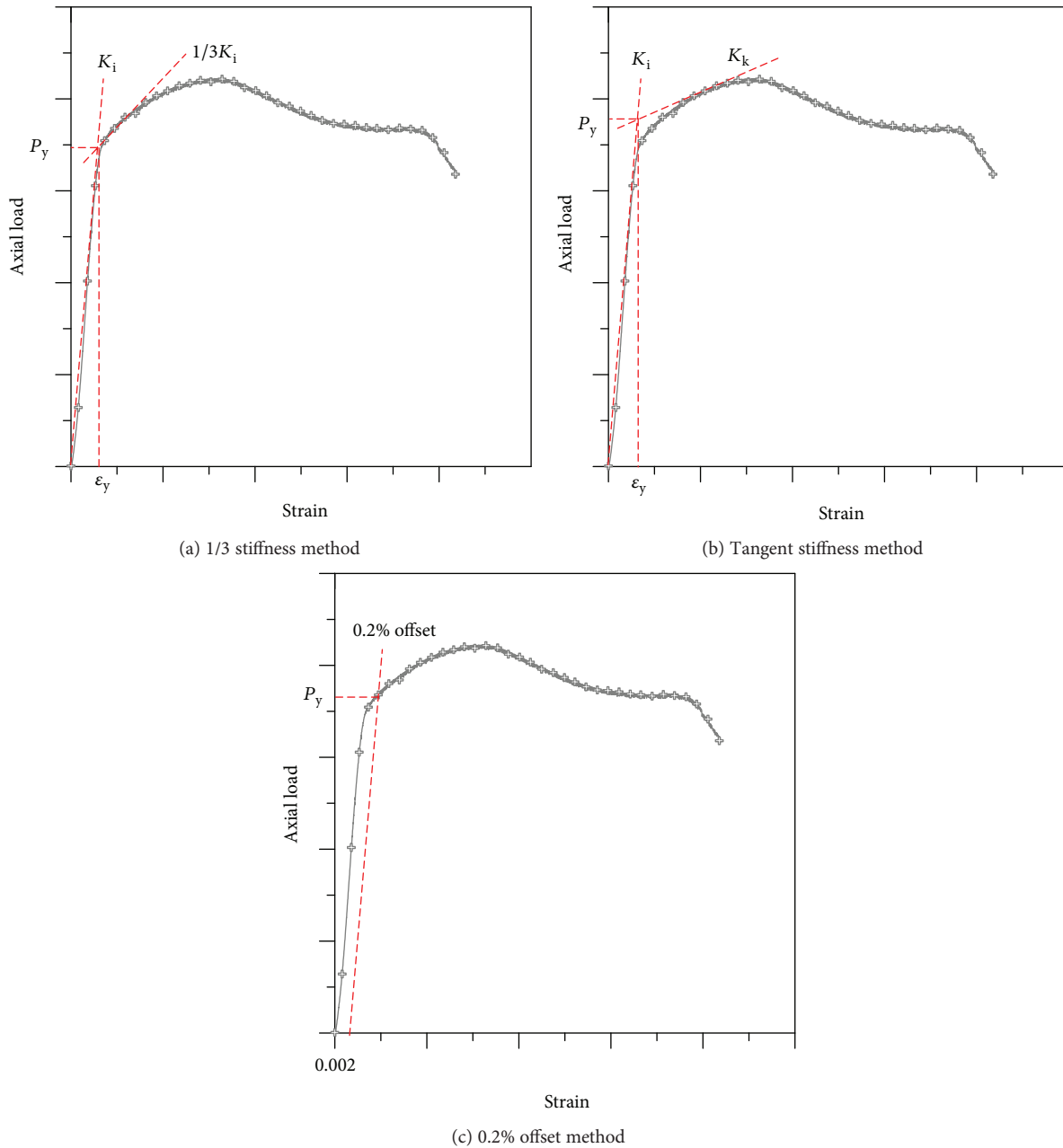


FIGURE 7: Determination method for yield strength of member.

**5.1. Modeling and Verification.** Concrete and steel modeling was performed using 3D solid elements. It was judged to be most efficient to model steel with solid elements to directly reflect the changes in the width-to-thickness ratio. As solid elements, we used the eight-node linear brick element C3D8R element provided by ABAQUS [27]. The model was constructed in a manner to express the deformation due to local buckling by using a nonlinear geometry option. As the constitutive law, it was decided to follow the isotropic hardening rule for steel, and for the uniaxial stress-strain relationships, we used the results of experiment performed on each specimen, as presented in Figure 2.

As for the concrete constitutive law, we used the concrete damaged plasticity model [28]. The concrete damaged

plasticity model is a model designed to describe the continuum plasticity-based concrete damage; for the purpose of this study, the major failure of concrete was assumed to arise from tensile cracking and compressive fracture. The plastic flow rule, nonassociated, can constitute an asymmetric stiffness matrix and is thus known to express rock-like brittle materials fairly well. Although it cannot express the cracks directly, it was selected for failure modeling because cracks do not play any significant role in this study.

Concrete material behavior can be modeled by inputting the uniaxial loads or the stress-strain relationships in the tensile state. In order to reflect the concrete strength changes, the compressive stress-strain model of Collins and Porasz [29] was used to enable the application of HSC. For modeling

TABLE 5: Strength of test specimens.

Specimen	$P_{cal}$ (kN)	$P_y$ (kN)	$P_u$ (kN)	$d_y$ (mm)	$d_u$ (mm)	$d_u/d_y$	$k$ (kN/mm)
HS-800	6007	6038	7632	7.00	28.88	4.13	875
CS-800-3	6261	7025	8402	7.03	31.16	4.43	1062
CS-800-10	6862	7400	8442	8.05	35.76	4.44	1120
CS-800-F10	6862	7627	8553	8.50	38.98	4.59	1125
HS-490	2473	2849	5620	3.79	57.70	15.22	880
CS-490-3	2726	3423	6127	4.50	106.50	23.67	882
CS-490-10	3332	3951	6745	4.68	112.16	23.97	960
CS-490-F10	3332	3958	7322	5.12	139.40	27.23	1040

$P_{cal}$ : calculated test specimen strength based on the code provisions (KBC2016);  $P_y$ : yield strength of test specimen;  $P_u$ : ultimate strength of test specimen;  $d_y$ : axial shortening of test specimen experiencing yield strength;  $d_u$ : axial shortening of test specimen experiencing ultimate strength;  $k$ : initial stiffness.

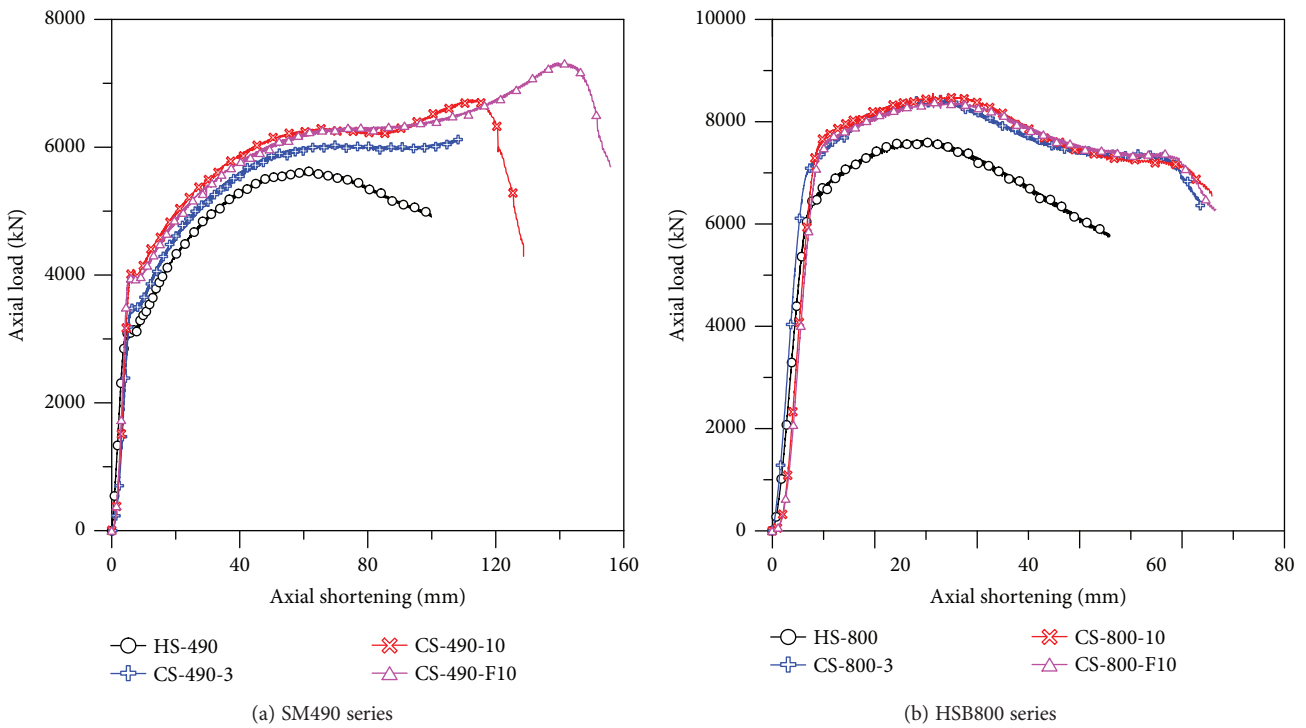


FIGURE 8: Load-displacement relation.

concrete tensile, the widely used Okamura–Maekawa [30] model was used and the effect of steel fibers was taken from the research results of Lok and Xiao [31]. The modulus of elasticity of concrete was calculated according to the methods provided in the Concrete Design Code (2012) [32], taking account of the link to KBC2016 [1]. The concrete-steel interface was modeled using the contact element. In the tangential direction, the frictional force between concrete and steel was modeled by inputting the friction coefficient of 0.25 proposed by Korea Concrete Institute [33] and modeling in the normal direction, with the mutual nodes of concrete and the steel configured to not permeate. This enabled the modeling of the confinement effect caused by the difference in the Poisson's ratio between steel and concrete. The general displacement control method was used for loading, and the

boundary conditions of the both ends of the column analyzed were entered as fixed ends.

Validation of the proposed model is an indispensable part of the process of FEA-based parametric analysis performed for the evaluation of the applicability of high-strength steel. This was done by analyzing the experimental results obtained in this study as well as the experimental results obtained in an earlier study [34] using specimens with compressive strength exceeding 800 MPa. The specimens used in the earlier study were rectangular CFTs ( $110 \times 110$  mm) made from HSS2 with a steel yield strength of 750 MPa, concrete compressive strength of 28 MPa, and panel thickness of 5 mm. The length of the specimens was 300 mm. The analysis results of the measured values obtained from the HSS2 specimens in the

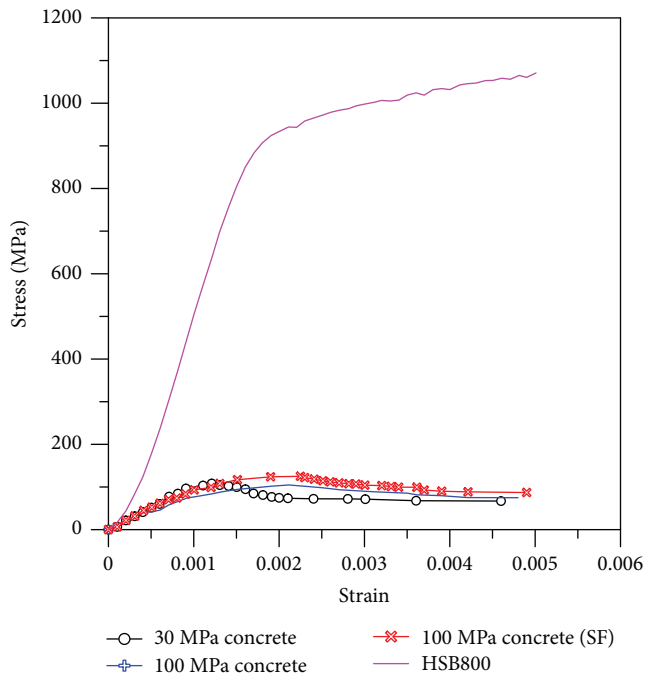


FIGURE 9: Stress-strain relation of concrete through the test results.

previous study and those obtained in the present study were compared with the numerical analysis results and presented in Figure 10. The comparison of the analysis results between the experimental and numerical values of all tested parameters revealed that the errors in the maximum load modeling were within the range of 10%, thus demonstrating that FEA model can be applied when analyzing the behavior of CFTs made from high-strength materials. The numerical and experimental results obtained from each specimen are outlined in Table 6.

*5.2. Failure Pattern with a Different  $b/t$  Ratio and Effectiveness of Matrix Strength and Steel Fiber Inclusion.* Figure 11 shows the analysis results of two specimens performed in this study, the CSS-800-10 and CSS-800-10, which used high-strength concrete and iron fiber-reinforced high-strength concrete for high-strength steels. Figure 11 showed the stress distribution diagram in the state in which the specimen was about to yield. It is confirmed that if it is not reinforced with steel fibers, as shown in Figure 11(a), the concrete can be converted into a tensile stress without resisting expansion due to compression stress. At the same time, it was found that the compression stress was about to be converted to tensile stress in the steel. On the other hand, it was found that, when mixed with steel fibers, there was no tensile stress on both concrete and steel, but only compressed stress appeared. As can be found in the material test results, this is judged to be the result of increased tensile strength by steel fibers. Accordingly, it is judged that the use of steel fiber may be delayed to buckling by the expansion force due to increased tensile strength of concrete.

The effect of the width-to-thickness ratio of high-strength steel panel on strength and strain was investigated,

and the load-displacement relations were normalized for the use of LSC and that of HSC based on the design formulae provided by the current design code; the results of which are plotted in Figures 11(a) and 11(b). It can be confirmed that the maximum strength point varied according to the width/thickness change. As the latter increased, the former occurred earlier. In the case of LSC, in particular, the maximum loads were found to fall short of the calculated values when the width-to-thickness ratio exceeded 50. In the case of HSC, the strength was found to be lower than the design strength when the width-to-thickness ratio exceeded 70. From this, it can be inferred that when high-strength steel is used, the maximum permissible width-to-thickness ratio needs to be reviewed to reflect different levels of concrete compressive strength. Figure 12(c) presents the analysis results for the steel fiber-reinforced HSC obtained to investigate the effect of steel fibers. The steel fiber reinforcement was found to increase not only the maximum load but also the crushing strain of concrete, thus increasing the maximum permissible width-to-thickness ratio when HSC is used. This highlights the need to consider the effect of steel fibers as well when reviewing the maximum permissible width-to-thickness ratio.

## 6. Conclusion

The main purpose of this study was to evaluate the feasibility of the application of rectangular CFTs made from high-performance materials, as well as their behavior. To this end, we performed experiments on rectangular CFT stub columns using high-strength steel and steel fiber-reinforced ultra-high-strength concrete and performed numerical analysis to investigate the relationship between the width-to-thickness ratio and high-performance concrete, which could not be tested experimentally. From these experimental and numerical processes, the following conclusions could be drawn.

- (1) It was confirmed by the experimental results that none of the specimens underwent weld fracture until their ultimate strength was reached and were thus shown to have sufficient strain capacity to resist the ultimate strength of steel, demonstrating that high-strength steel and steel fiber-reinforced high-strength concrete may be used within the test range.
- (2) Comparison of the experimentally obtained ultimate loads with the calculated loads led to the finding that experimental values exceeded the values prescribed as per design formulas. Therefore, it is considered reasonable to apply existing design formulas to the composite section of SB800 steel.
- (3) Because of the relatively large contribution of steel to strength, concrete filling was not found to bring about any significant degree of strength changes. In the case of using high-strength concrete, only the specimen using SM490 and all specimens using HSB800 showed yield strength enhancement rates

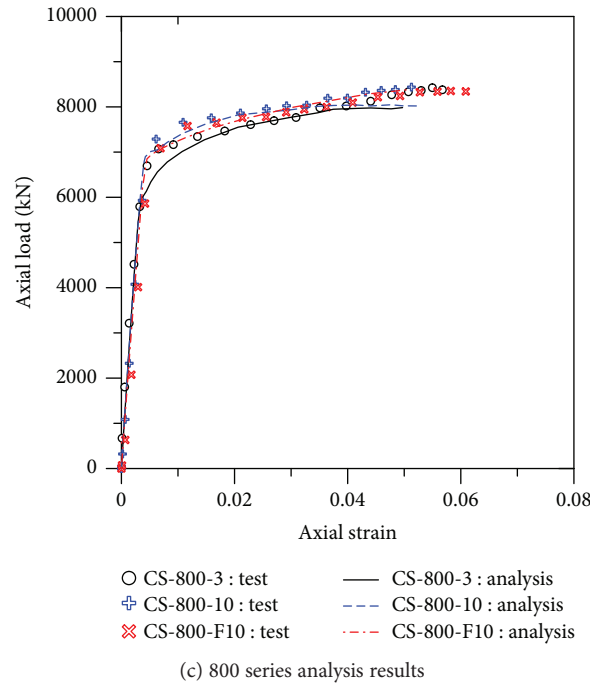
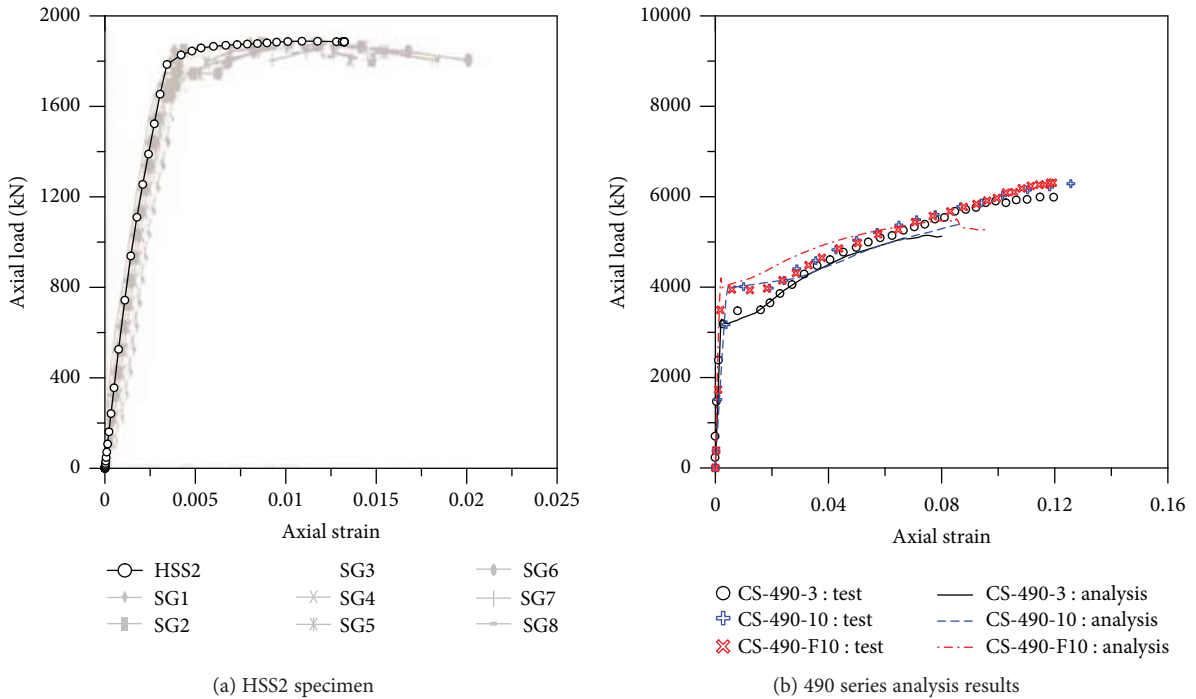


FIGURE 10: Verification of analysis.

similar to those of normal strength concrete. In strain capacity as well, no significant changes were observed when high-strength concrete was used, presumably because of a low confinement effect in enhancing its strength.

- (4) Steel fiber reinforcement was found to have little influence on strength enhancement in all specimens using HSB800 and SM490. This may be ascribable to the negligible strength change in concrete by the

steel fiber reinforcement. By contrast, the effect of steel fiber reinforcement was clearly demonstrated in the strain capacity.

- (5) Given the nature of concrete that increased strength and confinement bring about increase in maximum strain, the strain of the core concrete under confinement was indirectly measured and compared with the steel tube strain in order to examine the yield pattern, that is, whether the steel tube yields first. As a

TABLE 6: Comparison between analysis results and test results for CFT specimens.

Specimen	$P_{cal-code}$ (kN)	$P_{y-test}$ (kN)	$P_{y-mum}$ (kN)	$P_{u-test}$ (kN)	$P_{u-mum}$ (kN)
CS-800-3	6261	7025	6560	8402	7984
CS-800-10	6862	7400	7056	8442	8040
CS-800-F10	6862	7627	6943	8553	8386
CS-490-3	2726	3423	3277	6127	5077
CS-490-10	3332	3951	3779	6745	5402
CS-490-F10	3332	3958	3944	7322	5380

$P_{cal-code}$ : code-based strength;  $P_{y-test}$ : yield strength-test results;  $P_{y-mum}$ : yield strength-analysis results;  $P_{u-test}$ : ultimate strength-test results;  $P_{u-mum}$ : ultimate strength-analysis results.

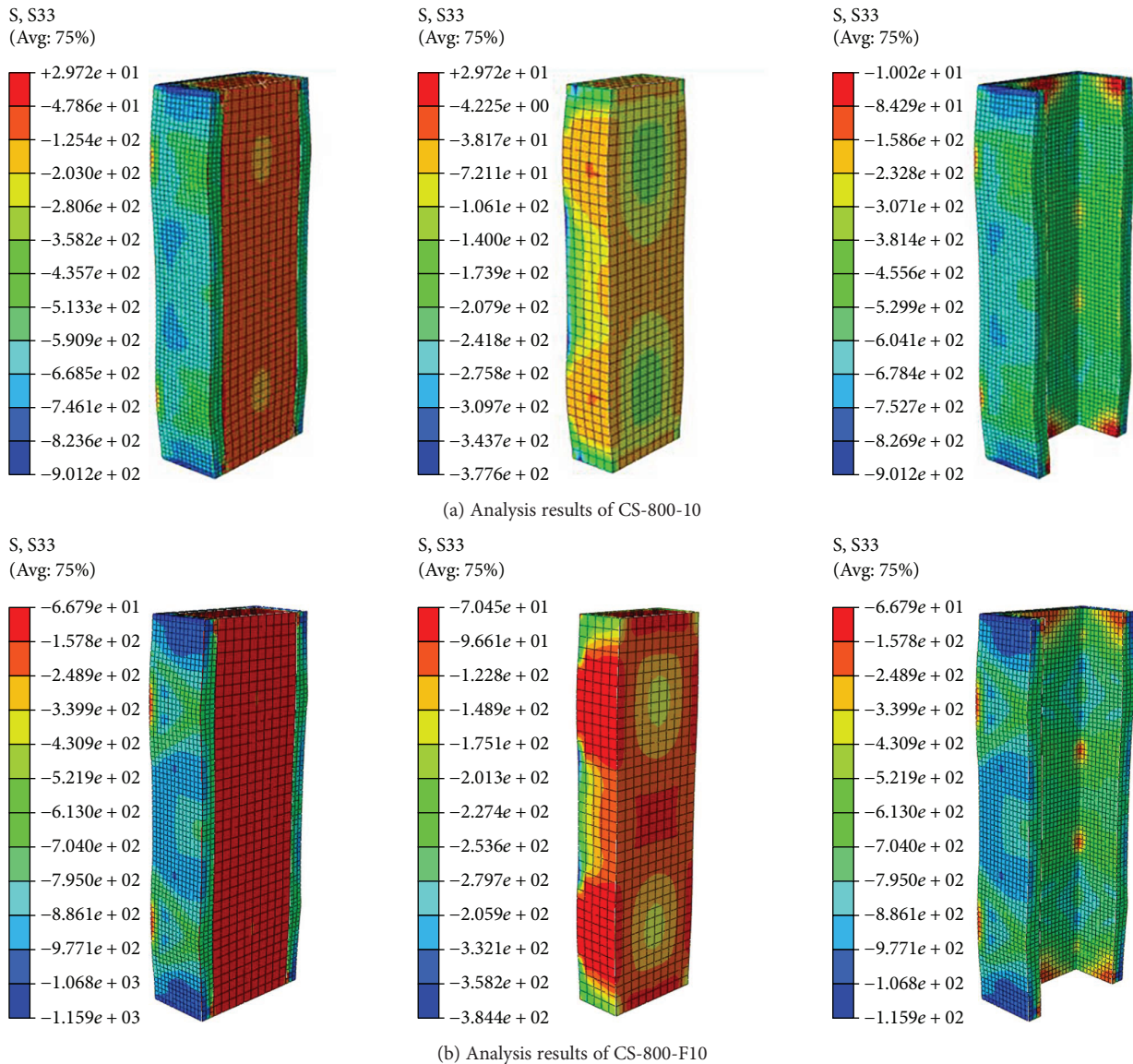


FIGURE 11: Failure aspect of SFRC-filled high-strength steel tube column.

result, it was found that the maximum strain of the core concrete was found to grow larger than that of the steel tube when it was filled with 100 MPa concrete and reinforced with steel fibers.

(6) Finite element analysis was performed to investigate the effect of the width-to-thickness ratio of steel, which could not be investigated experimentally. As a result of this numerical analysis, it was found that

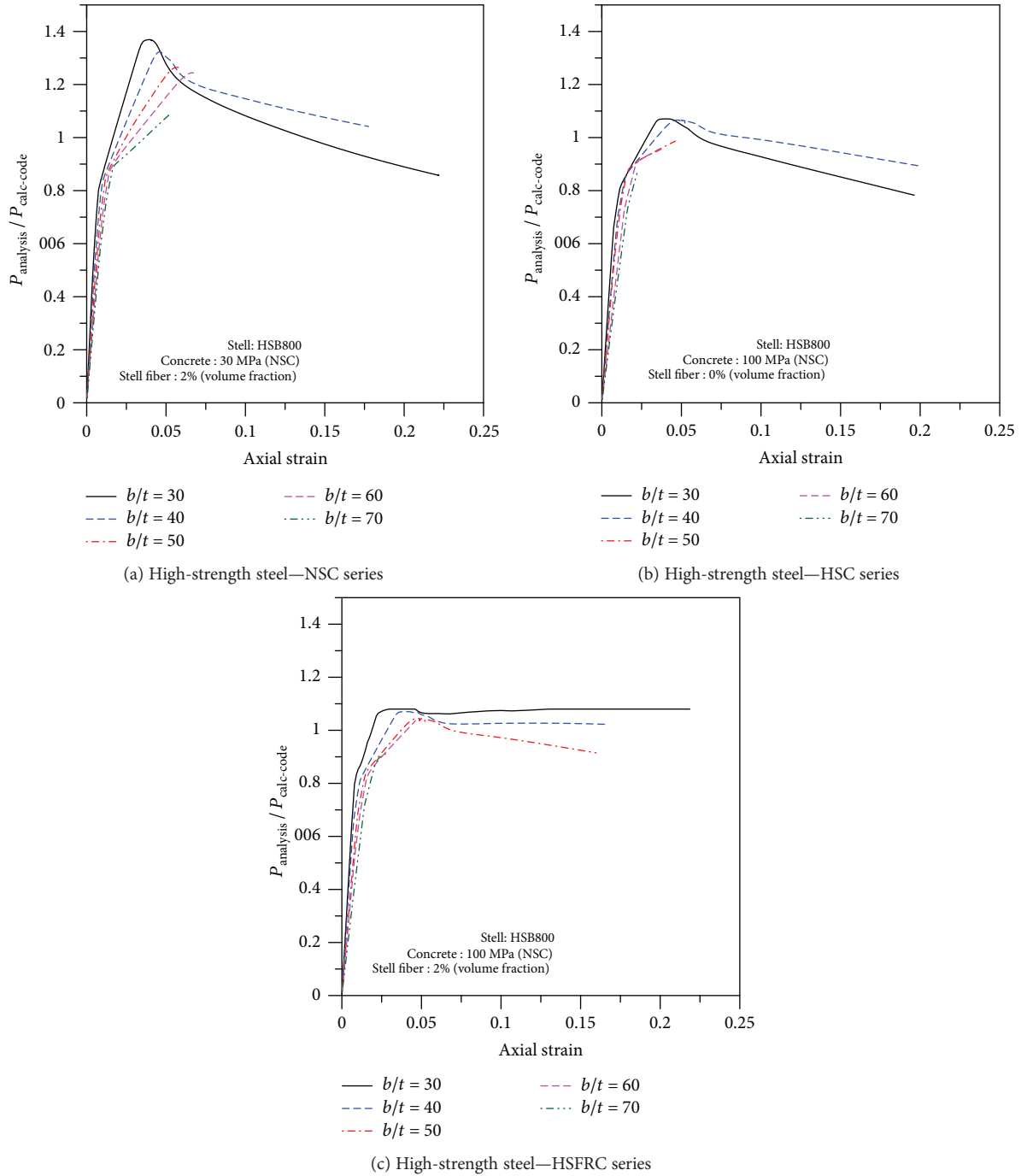


FIGURE 12: Limit  $b/t$  ratio according to matrix strength and steel fiber inclusion.

the maximum width-to-thickness ratio permissible for the strength limit set forth by the current building code varied depending on the concrete properties. The maximum permissible width-to-thickness ratio decreased as the concrete strength increased and increased after steel fiber reinforcement.

**Conflicts of Interest**

The authors declare that they have no conflicts of interest.

**Acknowledgments**

This work was supported by Chungwoon University Foundation grant, 2017, and the National Research Foundation of Korea (NRF) grant funded by the Korea government (MOE) (NRF-2015R1D1A1A01059989).

**References**

[1] KBC, *Korean Building Code and Commentary (KBC 2016)*, Architectural Institute of Korea, 2016.

- [2] ACI Committee 318, *Building Code Requirements for Structural Concrete (ACI 318-11) and Commentary*, American Concrete Institute, Farmington Hills, MI, USA, 2011.
- [3] ANSI/AISC 360-16, *Specification for Structural Steel Buildings*, American Institute of Steel Construction, Chicago, IL, USA, 2010.
- [4] European Committee for Standardization, *Eurocode 4: Design of Composite Steel and Concrete Structures*, CEN, 1994.
- [5] R. D. Ziemian, Ed., *Guide to Stability Design Criteria for Metal Structures*, John Wiley & Sons, Inc., Hoboken, NJ, USA, 6th edition, 2010.
- [6] J. F. Hajjar, "Concrete-filled steel tube columns under earthquake loads," *Progress in Structural Engineering and Materials*, vol. 2, no. 1, pp. 72–81, 2000.
- [7] N. E. Shanmugam and B. Lakshmi, "State of the art report on steel-concrete composite columns," *Journal of Constructional Steel Research*, vol. 57, no. 10, pp. 1041–1080, 2001.
- [8] A. H. Varma, J. M. Ricles, R. Sause, and L.-W. Lu, "Experimental behavior of high strength square concrete-filled steel tube beam-columns," *Journal of Structural Engineering*, vol. 128, no. 3, pp. 309–318, 2002.
- [9] R. T. Leon, D. K. Kim, and J. F. Hajjar, "Limit state response of composite columns and beam-columns part 1: formulation of design provisions for the 2005 AISC specification," *Engineering Journal*, vol. 44, no. 4, pp. 341–358, 2007.
- [10] J. R. Kim, S. S. Kim, C. H. Lee, E. T. Lee, and K. Y. Beak, "A study on the material characteristics and the welding properties of 600MPa grade steel (SM 570 TMC)," *Journal of Korean Society of Steel Construction*, vol. 20, no. 6, pp. 773–781, 2008.
- [11] European Committee for Standardization, *Eurocode 2: Design of Concrete Structures*, CEN, 1992.
- [12] ACI Committee 544, *Measurement of Properties of Fiber Reinforced Concrete*, American Concrete Institute, Farmington Hills, MI, USA, 1988.
- [13] B. A. Graybeal, "Compressive behavior of ultra-high-performance fiber-reinforced concrete," *ACI Materials Journal*, vol. 104, no. 2, pp. 146–152, 2007.
- [14] P. Bhargava, U. K. Sharma, and S. K. Kaushik, "Compressive stress-strain behavior of small scale steel fibre reinforced high strength concrete cylinders," *Journal of Advanced Concrete Technology*, vol. 4, no. 1, pp. 109–121, 2006.
- [15] A. S. Ezeldin and P. N. Balaguru, "Normal- and high-strength fiber-reinforced concrete under compression," *Journal of Materials in Civil Engineering*, vol. 4, no. 4, pp. 415–429, 1992.
- [16] B. De Nicolò, L. Pani, and E. Pozzo, "Strain of concrete at peak compressive stress for a wide range of compressive strengths," *Materials and Structures*, vol. 27, no. 4, pp. 206–210, 1994.
- [17] P. Richard and M. H. Cheyrezy, "Reactive powder concretes with high ductility and 200 - 800 MPa compressive strength," *Special Publication*, vol. 144, pp. 507–518, 1994.
- [18] KS B 0801, *Test Pieces for Tensile Test for Metallic Materials, KS B 0801*, Korean Agency for Technology and Standards (in Korean), 2007.
- [19] KS B 0802, *Method of Tensile Test for Metallic Materials, KS B 0802*, Korean Agency for Technology and Standards (in Korean), 2013.
- [20] KS F 2405, *Standard Test Method for Compressive Strength of Concrete, KS F 2405*, Korean Agency for Technology and Standards (in Korean), 2010.
- [21] KS F 2423, *Method of Test for Splitting Tensile Strength of Concrete, KS F 2423*, Korean Agency for Technology and standards (in Korean), 2006.
- [22] JCI-S-001, *Method of Test for Fracture Energy of Concrete by Use of Notched Beam, JCI-S-001*, Japan Concrete Institute Standard, 2003.
- [23] C. S. Choi, H. S. Jung, and H. K. Choi, "Behaviour of concrete filled steel square-tube stub column with steel-fiber reinforced high strength concrete," *Advanced Materials Research*, vol. 663, pp. 125–129, 2013.
- [24] M. A. Mansur, M. S. Chin, and T. H. Wee, "Stress-strain relationship of high-strength fiber concrete in compression," *Journal of Materials in Civil Engineering*, vol. 11, no. 1, pp. 21–29, 1999.
- [25] L. S. Hsu and C. T. Hsu, "Stress-strain behavior of steel-fiber high-strength concrete under compression," *ACI Structural Journal*, vol. 91, no. 4, pp. 448–457, 1994.
- [26] G. Campione, S. Mindness, and G. Zingone, "Compressive stress-strain behavior of normal and high-strength carbon fiber concrete reinforced with steel spirals," *ACI Materials Journal*, vol. 96, no. 1, pp. 27–34, 1999.
- [27] P. Paultre, R. Eid, Y. Langlois, and Y. Lévesque, "Behavior of steel fiber-reinforced high-strength concrete columns under uniaxial compression," *Journal of Structural Engineering*, vol. 136, no. 10, pp. 1225–1235, 2010.
- [28] D. Hibbit, B. Karlsson, and P. Sorensen, *ABAQUS Theory Manual Ver. 6.10.1*, Hibbit, Karlsson and Sorensen, Inc., 2010.
- [29] J. Lee and G. L. Fenves, "A plastic-damage concrete model for earthquake analysis of dams," *Earthquake Engineering & Structural Dynamics*, vol. 27, no. 9, pp. 937–956, 1998.
- [30] M. P. Collins and A. Porasz, *Shear Design for High Strength Concrete*, The International Federation for Structural Concrete, CEB Bulletin d'Information, No. 193, 1989.
- [31] H. Okamura and K. Maekawa, *Nonlinear Analysis and Constitutive Models of Reinforced Concrete*, Gihodo-Shuppan Co., Tokyo, Japan, 1991.
- [32] T. S. Lok and J. R. Xiao, "Flexural strength assessment of steel fiber reinforced concrete," *Journal of Materials in Civil Engineering*, vol. 11, no. 3, pp. 188–196, 1999.
- [33] Korea Concrete Institute, *Code Requirement and Commentary for Reinforced Concrete Structure*, Korea Concrete Institute, 2012.
- [34] E. Ellobody, B. Young, and D. Lam, "Behaviour of normal and high strength concrete-filled compact steel tube circular stub columns," *Journal of Constructional Steel Research*, vol. 62, no. 7, pp. 706–715, 2006.

## Research Article

# Flexural Assessment of Blast-Damaged RC Beams Retrofitted with CFRP Sheet and Steel Fiber

Jin-Young Lee <sup>1</sup>, Hyun-Oh Shin,<sup>2</sup> Kyung-Hwan Min,<sup>3</sup> and Young-Soo Yoon <sup>1</sup>

<sup>1</sup>School of Civil, Environmental and Architectural Engineering, Korea University, 145 Anam-ro, Seongbuk-gu, Seoul 02841, Republic of Korea

<sup>2</sup>Department of Agricultural and Rural Engineering, Chungnam National University, 99 Daehak-ro, Yuseong-gu, Daejeon 34134, Republic of Korea

<sup>3</sup>Rail Research Institute, Chungnam National University, 99 Daehak-ro Yuseong-gu, Daejeon 34134, Republic of Korea

Correspondence should be addressed to Young-Soo Yoon; [ysyoon@korea.ac.kr](mailto:ysyoon@korea.ac.kr)

Received 29 January 2018; Accepted 16 April 2018; Published 10 June 2018

Academic Editor: Aamer Bhutta

Copyright © 2018 Jin-Young Lee et al. This is an open access article distributed under the Creative Commons Attribution License, which permits unrestricted use, distribution, and reproduction in any medium, provided the original work is properly cited.

This study presents the effects of blast-induced local damages on the flexural strength of blast-damaged and repaired specimens. In the experimental program, blast-damaged specimens were repaired with steel fiber reinforced cementitious composite (SFRCC) as well as carbon fiber-reinforced polymer (CFRP) sheets and tested for flexural strength measurements. The test parameters included shear reinforcement (amount and spacing), steel fiber content (0, 1.0 vol%), and retrofitting with CFRP sheets. The test results indicated that the use of higher amounts of stirrups demonstrated insignificant benefits in preventing local damages. However, it was shown that the use of small-diameter steel bars for stirrups with small spacing could decrease the local damages more effectively compared to the large-diameter steel reinforcement. For the residual strength of the damaged specimens, the specimens using more stirrups could resist over 60% of their original flexural strength. CFRP retrofitting showed insignificant enhancement in ductility of intact, damaged, and repaired specimens. However, it distributed the blast load and protected debris scattering. The addition of steel fibers results in increased ductility and enhanced blast resistance against local damages. All specimens, excluding control specimen, that repaired with SFRCC showed higher flexural strength to their original strength. Therefore, it can be concluded that replacing damaged concrete cover with SFRCC is adequate for repairing the blast-damaged RC members.

## 1. Introduction

The most effective method to protect a structure from a blast risk is to maintain an adequate stand-off distance from the source of the blast. In other words, a structural member is extremely vulnerable from a close-in blast. If such a blast causes a local damage on the structure, it may lead to a progressive collapse. Therefore, vehicles are not allowed near important structures in the United States in order to prevent the structures from damage by close-in blasts [1]. When maintaining a stand-off distance is difficult, the structures should be constructed by using the reinforcing method that can protect themselves from blasts. Therefore, numerous researchers [2–21] have conducted studies to suggest the enhanced reinforcing method against a blast and evaluate

the blast resistance of the suggested method. The conventional method to increase the blast resistance is to use a considerable amount of shear reinforcement. Fujikake and Aemlaor [9] experimentally and numerically analyzed the blast resistance of the RC (reinforced concrete) columns by considering not only the shear reinforcement ratio but also the concrete strength and reported that the shear-reinforcing bars confining the core concretes of the RC columns significantly affect the damage of the specimens. Burrell et al. [5] also reported that seismic detailing improves blast performance of RC columns. Despite the results of the abovementioned research, considerably little experimental studies have been devoted to examining the role of shear reinforcement in RC beams under blast load. Therefore, in this study, the blast test on RC beams considering the

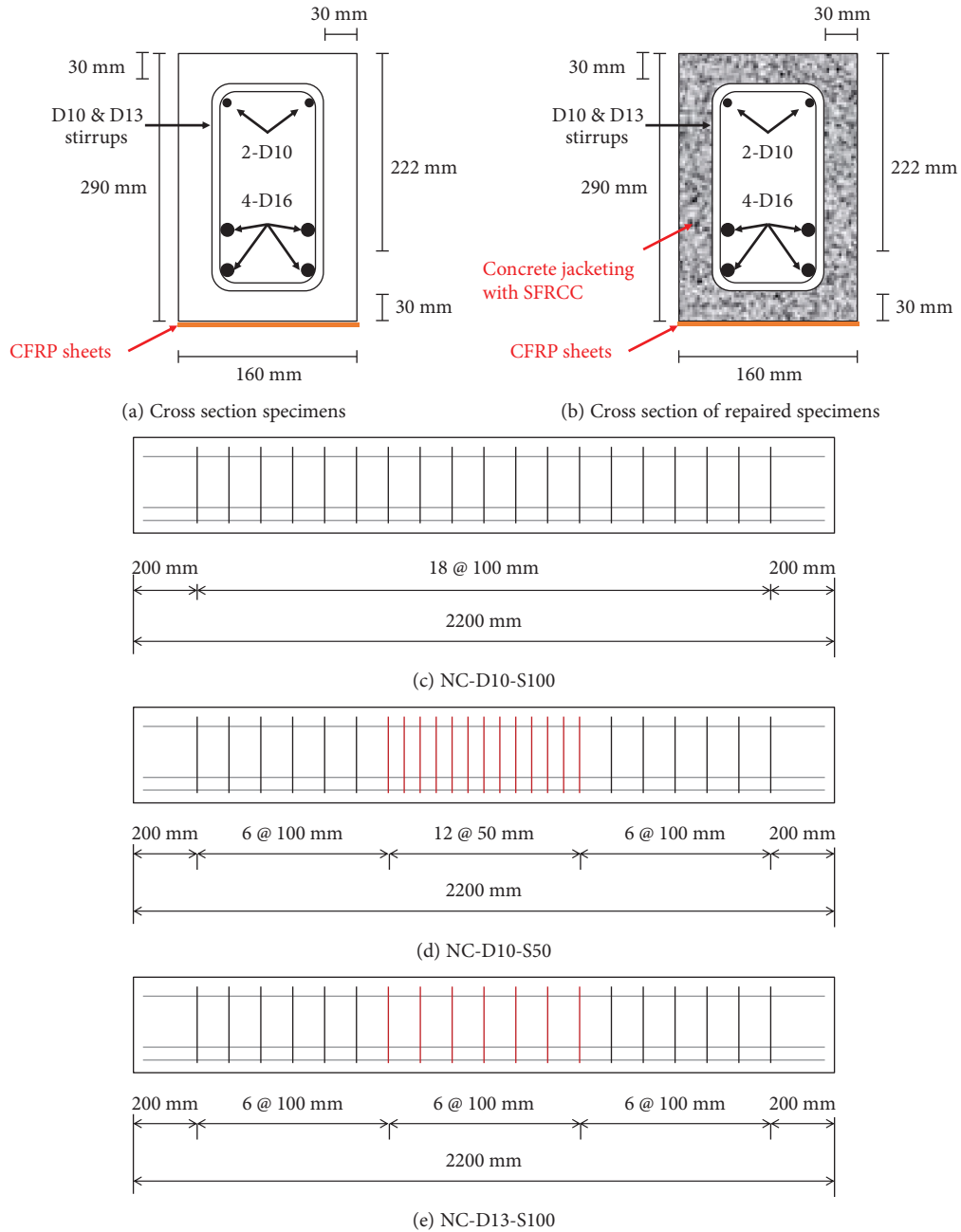


FIGURE 1: Details of test specimens.

TABLE 1: Test variables.

Notation	Concrete	Shear reinforcement	$A_v$ (mm <sup>2</sup> )	FRP
NC-D10-S100	Normal concrete	D10, $s = 100$ mm	998	Not retrofitted
NC-D10-S50		D10, $s = 50$ mm	1854	
NC-D13-S100		D13, $s = 100$ mm	1774	CFRP sheet
NC-D10-S100-F		D10, $s = 100$ mm	998	
SFRC-D10-S100		SFRC with 60 mm steel fiber	D10, $s = 100$ mm	

amount and spacing of shear reinforcements as variables was conducted. A better understanding of the mechanics associated with the effects of shear reinforcement on the local

damages and residual strength could allow the designer to determine the shear reinforcement that is most desirable for the blast-resistant structures.

TABLE 2: Mix proportions of NC, SFRC, and SFRCC [12].

Type of concrete	Water (kg/m <sup>3</sup> )	Cement (kg/m <sup>3</sup> )	Fine aggregate (kg/m <sup>3</sup> )	Coarse aggregate (kg/m <sup>3</sup> )	Steel fiber (%) <sup>a</sup>
NC <sup>b</sup>	140	350	792	1015	0.0
SFRC <sup>b</sup>	140	350	792	1015	1.0
SFRCC	140	350	1807	0	1.0

<sup>a</sup>Volume fraction of fibers. <sup>b</sup>Data cited from [12].

TABLE 3: Strength of NC, SFRC, and SFRCC [12].

Concrete	Compressive strength (MPa)	Flexural strength (MPa)
NC <sup>a</sup>	38.7	4.7
SFRC <sup>a</sup>	31.0	6.4
SFRCC	42.3	6.2

<sup>a</sup>Data cited from [12].

TABLE 4: Properties of steel fibers.

Type of fiber	Length (mm)	Diameter (mm)	Aspect ratio (L/D)	Tensile strength (MPa)
End-hooked steel fiber	60	0.75	80	1196

Recent research has shown that using SFRC and retrofitting with FRP composites can improve the strength and ductility of RC members [22–28]. The effectiveness of using FRP sheet to improve blast behavior of RC members has been demonstrated experimentally and numerically by Saatcioglu et al. [21]. Ross et al. [14] also reported that FRP retrofitting is effective in increasing blast resistance. In case of SFRC, some limited research has been conducted on RC members under blast load. Lan et al. [29] conducted a field blast test on RC slabs and noted that SFRC panels demonstrated improved damage tolerance. However, most previous studies focused on the blast resistance at the moment; the blast load was imparted on the specimens without considering the structural behavior after the blast. In this context, few studies were performed to evaluate residual strength of blast-damaged specimens, although the effect of local damages on the structural strength of the specimens is an important factor that could lead to progressive collapse. Moreover, limited research has been conducted on the repaired RC beams using steel fiber-reinforced cementitious composite (SFRCC) and carbon fiber-reinforced polymer (CFRP) sheet.

Accordingly, in this study, blast-induced local damages and static flexural strength of intact, damaged, and repaired specimens were examined. The test data of the flexural test on intact specimens and blast test was cited from previous studies [11, 12]. The amount and spacing of shear reinforcements, the addition of steel fiber, and FRP retrofitting were considered as test variables to investigate the effect of the various reinforcing methods on blast-local damages. For the flexural test on repaired specimens, the specimens were fabricated by using SFRCC, CFRP sheet, and blast-damaged specimens that were tested in the previous study and tested

TABLE 5: Properties of reinforcement.

Deformed bar	Nominal diameter (mm)	Area (mm <sup>2</sup> )	Yield strength (MPa)	Ultimate strength (MPa)
D10	9.53	71.3		
D13	12.7	126.7	508.5	605.3
D16	15.9	198.6		

TABLE 6: Typical mechanical properties of FRP composite [11].

	Thickness (mm)	Tensile strength (MPa)	Elastic modulus (GPa)	Ultimate strain (%)
CRFP sheet	1.4	2400	131	1.87

to investigate the effect of repairing materials on flexural strength of repaired specimens.

## 2. Experimental Program

**2.1. Details of Test Specimens.** The experimental program consisted of four phases: (1) static tests on intact specimens, (2) blast tests on intact specimens, (3) static tests on blast-damaged specimens, and (4) static tests on repaired specimens. Five reinforced RC beams were tested, and the test data of ten specimens were cited to investigate the effect of CFRP sheet, steel fibers, and shear reinforcement in RC beams under blast load [11, 12]. The details of the specimens are shown in Figure 1 and Table 1.

The types of concrete (NC, SFRC), CFRP retrofitting, and details of shear reinforcement were considered as variables. As illustrated in Figure 1, all specimens were 160 mm in width, 290 mm in height, and 2200 mm in length. In addition, longitudinal reinforcements consisted of four 15.26 mm diameter-deformed steel-reinforcing bars (denoted as D16). NC-D10-S100 (control specimen), NC-D10-S100-F, and SFRC-D10-S100 were designed according to the minimum shear requirements of ACI 318-14 [30] and composed of 10 mm deformed reinforcing bars (denoted as D10). They were conventional rectangular stirrups and spaced at 100 mm along the middle zone of the beams. In case of NC-D10-S50 and NC-D13-S100, the stirrups, composed of D10 and D13 rebars, were spaced at 50 and 100 mm, respectively. For the FRP retrofitting, two layers of CFRP sheets were bonded with epoxy on the bottom of the beam. After the blast test, blast-damaged specimens were repaired with SFRCC. The details of the repaired specimens are presented in Figure 1(b). A 30 mm thick SFRCC layer was used to wrap

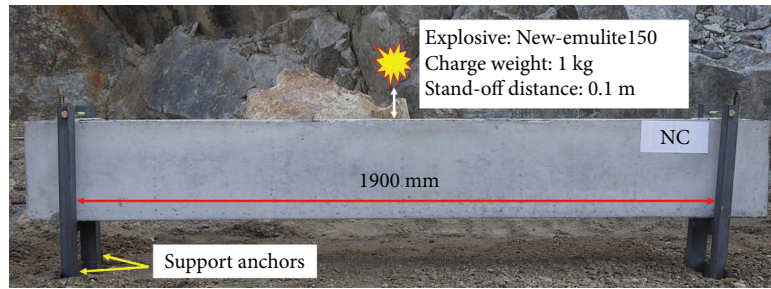


FIGURE 2: Test set-up of a blast test.

TABLE 7: Properties of explosive [12].

Detonation velocity (m/s)	Volume density (g/cc)	Energy of explosion (kcal/kg)	Drop sensitivity (cm)	Amount of gas (L/kg)
5900	1.18 ~ 1.50	1140	100	820

TABLE 8: Anticipated blast load.

Charge weight (kg)	Stand-off distance (m)	Peak pressure (MPa)	Peak impulse (MPa/ms)	Duration for positive phase (ms)
1.0	0.1	38.6	1.42	0.07

the damaged specimens after eliminating a damaged concrete cover. In the case of NC-D10-S100-F, the repaired specimen was retrofitted with CFRP sheet again.

**2.2. Material Properties.** The concrete properties and mix proportions are summarized in Tables 2 and 3. All specimens were fabricated with an identical mixture that had a water-to-cement ratio of 0.4 and maximum aggregate size of 20 mm. However, in the case of SFRCC, coarse aggregate was not used in order to gain better structural performance under static and blast loadings. For SFRC and SFRCC, 60 mm hooked-end steel fibers were used in the cement paste and the fiber content was 1.0 vol%. The properties of steel fiber are shown in Table 4. The compressive and flexural strengths were measured based on ASTM C39 and C1609 [31, 32], on cylinders with a diameter of 100 mm and height of 200 mm and beams with a cross section of 100 × 100 mm and a length of 400 mm. The compressive strength of NC, SFRC, and SFRCC was approximately 39, 31, and 42 MPa, respectively. In case of flexural strength, NC exhibited an average strength of 4.7 MPa, while the SFRC and SFRCC exhibited an average strength of approximately 6.3 MPa. For steel reinforcements, Grade 400 Korean Standard (KS) deformed reinforcing bars were used. The properties are presented in Table 5. Woven carbon fiber sheets were used for FRP retrofitting, and typical properties of FRP composite are shown in Table 6.

### 2.3. Test Procedure

**2.3.1. Static Test.** Static three-point flexural tests were carried out on five repaired specimens with a quasi-static loading rate of 0.02 mm/s using a universal testing machine (UTM) with maximum load capacity of 2800 kN. The mid-span deflection, excluding the support settlement, was measured by linear variable differential transducers (LVDTs). The specimens were simply supported, and clear span was 1900 mm. The steel bearing plates were placed at the loading and support points to prevent local crushing of the concrete.

Static flexural tests on the intact and damaged specimens were performed by Lee et al. [11, 12], and the test results were cited to evaluate the effect of CFRP sheet, steel fibers, and shear reinforcement in RC beams. All of the tests on intact, damaged, and repaired specimens were conducted using identical instrumentation.

**2.3.2. Close-In Blast Test.** Close-in blast tests on specimens were carried out by Lee et al. [11, 12]. The local damages and effect of CFRP sheet, steel fibers, and shear reinforcement were investigated by analyzing the test results. After the blast tests, the residual strength of blast-damaged specimens and flexural strength of repaired specimens were measured. Test set-up of the blast test is presented in Figure 2. For the blast tests, New-emulite150, emulsion explosive, was used to impart the blast load on the specimens. The TNT equivalent factor of this explosive is 1.01, and the properties of explosive are presented in Table 7. Charge weight of explosive was 1 kg, and stand-off distance was 0.1 m. The imparted blast pressure was calculated by AT-Blast software and shown in Table 8.

## 3. Experimental Results and Discussion

### 3.1. Evaluation of Blast-Induced Local Damages

**3.1.1. Effect of Shear Reinforcement on Local Damages.** When a blast occurs, the main types of local damage on concrete specimen can be classified into three types: crater, spall, and breach. As shown in Figure 3, crater occurs at the front side of the specimen when the specimen is directly exposed to the blast pressure, while the spall is a rear side damage induced by tensile stress. Breach occurs when the specimen is totally penetrated [33]. In addition, shear plug also occurs when the impact or blast load is imparted on the concrete beams because the velocity of the crack propagation is higher than the load transfer velocity. After the close-in blast test, the fracture behaviors of the specimens were observed. Diameter and depth of local damages, angle of shear crack,

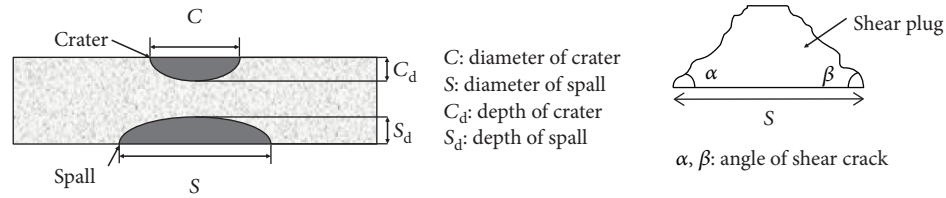


FIGURE 3: Blast-induced local damages.

TABLE 9: Local damages of specimens [11, 12].

Variables	Local damages					
	C (cm)	C <sub>d</sub> (cm)	S (cm)	S <sub>d</sub> (cm)	α (°)	β (°)
NC-D10-S100	77	14	89	6	26	29
NC-D10-S50	72	16	74	7	23	32
NC-D13-S100	70	14	88	9	26	28
NC-D10-S100-F	79	15	103	5	30	25
SFRC-D10-S100	48	12	0	0	34	25

and weight loss were measured. These are presented in Table 9 and Figure 4. The average crack angle was 25° in blast-damaged specimens. In the case of NC series, there were no significant differences in size of crater and spall, because most of the fracture occurred at the concrete cover. However, for the weight loss, NC-D10-S50 showed the smallest weight loss among the NC series except NC-D10-S100-F. On the other hand, NC-D13-S100 showed same weight loss with NC-D10-S100, even though it had 1.8 times of shear reinforcement compared with NC-D10-S100. From the above results, it was confirmed that the space of stirrups is a more important factor in protecting the concrete core than the amount of shear reinforcements.

**3.1.2. Effect of FRP and Steel Fiber on Local Damages.** As presented in Table 9 and Figure 4, retrofitting with CFRP sheets and adding fibers enhance the blast resistance against local damages. Particularly, spalling did not occur in SFRC specimen because of a fiber bridging capacity at the rear side of the specimen. Moreover, the smallest amounts of crater and weight loss were observed. Therefore, it was verified through the experimental tests that the addition of steel fibers can be an effective method to enhance blast resistance against local damages. In case of NC-D10-S100-F, weight loss was reduced compared to control beam, NC-D10-S100, even though there were no significant differences in size of crater and spall. In addition, CFRP sheet distributed the blast load and protected debris scattering before bonding failure between CFRP sheet and concrete.

**3.2. Static Response of Intact Specimens.** The load-displacement curves and summary of test results obtained from the static tests on intact, blast-damaged, and repaired specimens are presented in Figure 5 and Table 10. In the static flexural test, all of the intact specimens failed in flexure-critical mode, because every specimen had identical details in longitudinal reinforcement. NC series except NC-D10-

S100-F sustained an average flexural strength of 183.1 kN-m. The addition of fibers and retrofitting with CFRP sheet resulted in an increase of 13% and 8% in the flexural strength, respectively, compared to the average strength of NC series. Although these specimens failed at similar maximum loads, SFRC-D10-S100, which was reinforced with steel fibers, exhibited the highest ductility index calculated as follows:

$$\text{Ductility index} = \frac{\Phi_u}{\Phi_y} \quad (1)$$

In case of NC-D10-S100-F, the brittle bonding failure between CFRP sheet and concrete occurred, while it showed the highest flexural strength. In addition, it exhibited the lowest ductility index. Therefore, it is recommended to use FRP sheet on RC members with caution.

**3.3. Residual Strength of Blast-Damaged Specimens.** After the blast test, static flexural test on damaged specimens was carried out to investigate the residual strength of the specimens [11, 12]. From these test results, the effect of local damages on residual strength was examined. In the damaged NC series, flexural strength of NC-D10-S100, NC-D10-S50, and NC-D13-S100 decreased by 59%, 30%, and 39%, respectively, compared to the original strength of intact specimens. The residual strength was significantly decreased because of buckling of compressive reinforcing bars when the concrete cover at compression zone was fractured. On the other hand, NC-D10-S50 and NC-D13-S100, which were the specimens reinforced with more amounts of shear stirrups than the control specimen, showed relatively less decrease in residual strength because of the effect of confinement by stirrups. SFRC specimens showed the highest residual strength because relatively small local damages at the front and rear sides occurred. Thus, it can be concluded that the addition of steel fibers is the most effective method to maintain residual strength of a structural member after blast. In the case of NC-D10-S100-F, flexural strength was decreased by 33%, compared to original strength.

**3.4. Flexural Strength of Repaired Specimens.** As plotted in Figure 5, all repaired specimens showed ductile behavior and higher flexural strength than the strength of intact specimens. In the case of the control specimen, NC-D10-S100, the flexural strength increased by 11%, while the ductility index decreased by 44%, compared to test results of the intact specimen. These results are because the concrete cover was replaced with SFRC that had a higher compressive and tensile strength than that of normal concrete, and the longitudinal reinforcements yielded

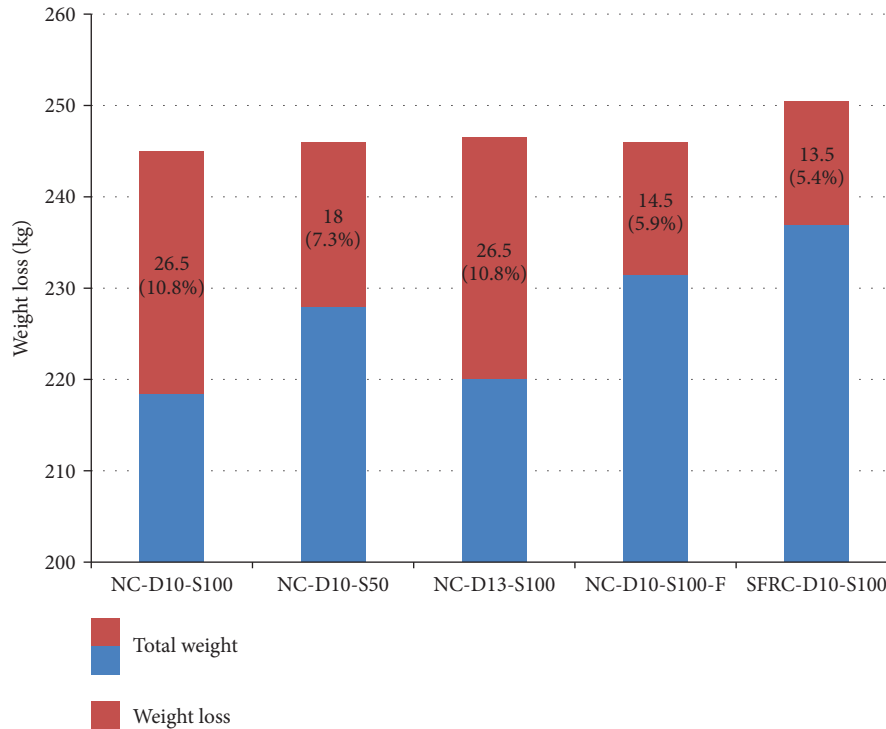


FIGURE 4: Weight loss of blast-damaged specimens.

during the blast load was imparted on the specimen. For NC-D10-S50 and NC-D13-S100, these two specimens had similar flexural behavior. The flexural strength of these specimens increased by 6% and 14%, respectively. Moreover, these beams showed an increase in the ductility index approximately 27% and 19%, respectively. From these results, it can be concluded that sufficient shear reinforcement can provide considerable blast resistance against local damages and yielding of the longitudinal reinforcement. As a result of the decrease in local damages, the flexural strength of repaired specimens can regain the design-intended structural performance.

The NC-D10-S100-F, CFRP-retrofitted specimen, demonstrated significant increase in flexural strength and ductility. Although bonding failure between CFRP sheet and concrete occurred during the test, the specimen still showed ductile behavior with higher flexural strength than the strength of the intact specimen. However, further research is required to study the bond failure between FRP and concrete under blast-loading condition.

As mentioned previously, adding fibers enhances the blast resistance against local damages under the blast loads. However, it led to an increase in load ratio that was resisted by the longitudinal reinforcement. This was due to the increase in maximum displacement at maximum load of SFRC specimen over the yield point of steel rebars. As a result, the ductility index of repaired specimen decreased because the longitudinal reinforcement was yielded when the blast load was imparted on the specimen, whereas the structural behavior of blast-damaged specimen was relatively ductile. Therefore, there is the need to consider the design

goals of structural members when the SFRC is applied on the members.

#### 4. Conclusions

This study investigated the effects of stirrups, FRP retrofitting, and adding steel fibers on intact, blast-damaged, and repaired RC beams. From the above discussions, the following conclusions are drawn:

- (1) When blast load was imparted on RC beams by close-in detonation, critical local damages on RC beams occurred even if the charge weight was small. It was verified through the experimental tests that the progressive collapse could have occurred because the residual strength of the damaged control specimen, NC-D10-S100, was below 40% of its original strength. Therefore, it is necessary to apply the protective design using more stirrups and SFRC and retrofitting with FRP on the structural members, if the members are vulnerable to a blast.
- (2) The use of higher amounts of stirrups demonstrated insignificant benefits in preventing local damages. However, it was shown that the use of small-diameter steel bars for stirrups with small spacing could decrease the local damages rather than the use of large-diameter steel reinforcements, when the volume of stirrups was fixed. For the residual strength of the damaged specimens, both specimens

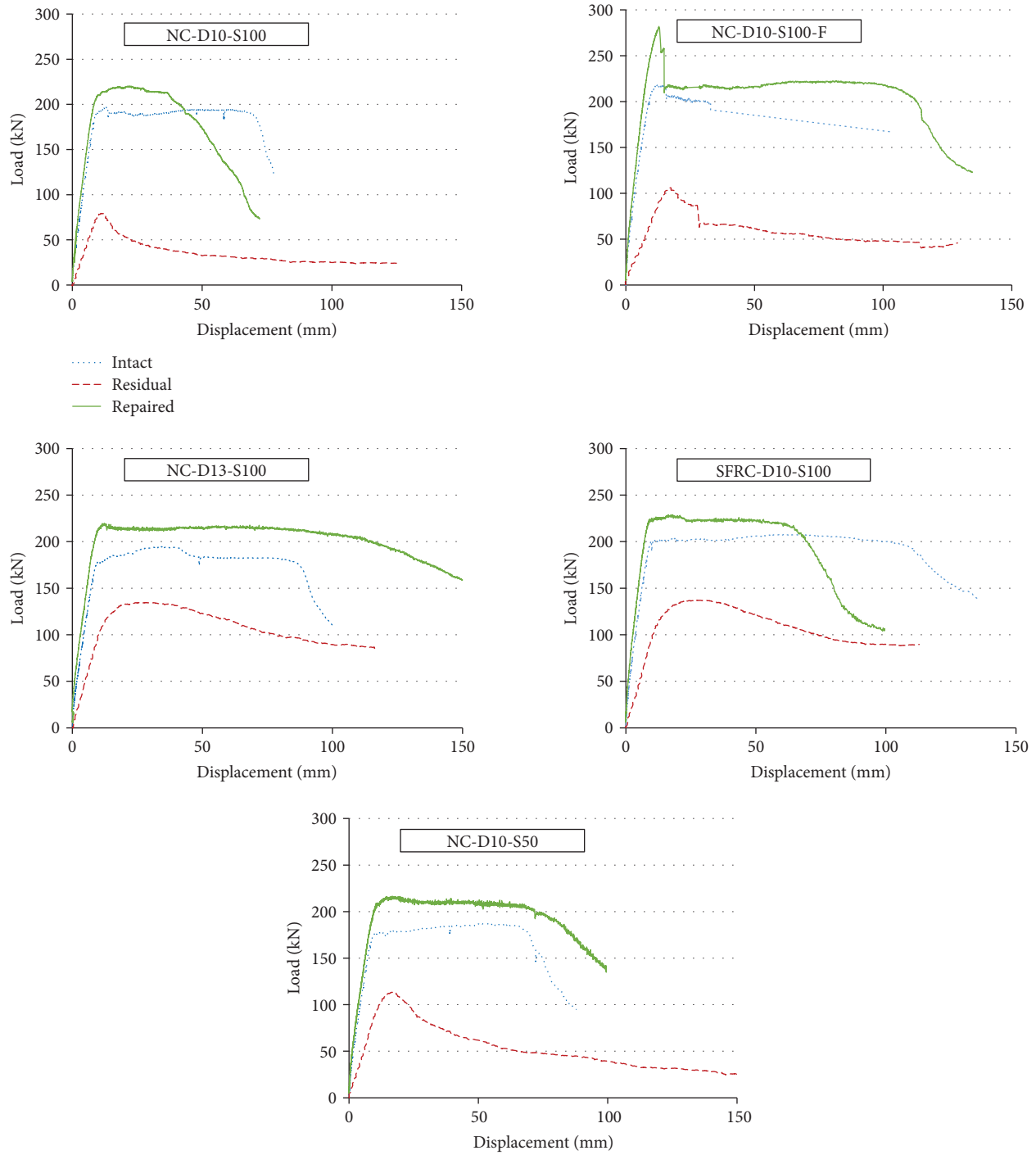


FIGURE 5: Load-displacement curves of intact, blast-damaged, and repaired specimens.

TABLE 10: Static flexural test results.

Variables	Max. load (kN)			Flexural strength (kN·m)			Ductility index ( $\Phi_u/\Phi_y$ )		
	Intact	Damaged	Repaired	Intact	Damaged	Repaired	Intact	Damaged	Repaired
NC-D10-S100	196.5	79.3	217.6	186.7	75.3	206.7	7.9	1.3	4.4
NC-D10-S50	194.6	134.6	205.8	184.9	127.9	195.5	4.8	3.1	6.1
NC-D13-S100	186.9	113.3	212.3	177.6	107.6	201.7	7.3	1.4	8.7
NC-D10-S100-F	217.5	105.9	258.4	206.6	100.6	245.5	3.3	1.9	9.1
SFRC-D10-S100	207.5	137.2	225.3	197.1	130.3	225.3	11.5	2.7	5.5

using more stirrups could resist above 60% of the original flexural strength. Therefore, it can be concluded that although the use of higher amounts of stirrups was not adequate to prevent the blast-induced local damages, it can increase the residual strength because of improved confinement.

- (3) The addition of steel fibers results in increased ductility and enhanced blast resistance against local damages. However, the ductility index of repaired specimen decreased, because the longitudinal reinforcement experienced flexural yielding when the blast load was imparted on the beam. Therefore, it is recommended to design the steel reinforcements with consideration of the characteristics of SFRC, while designing the structures subjected to extreme loadings. In case of FRP retrofitting, it demonstrated significant increase in flexural strength. Moreover, it showed benefit in protecting debris. However, bonding failure between CFRP sheet and concrete occurred in the intact and repaired specimens. Therefore, further research is needed to increase the bond strength between FRP sheet and concrete.
- (4) All specimens that repaired with SFRC showed higher flexural strength than the original strength, except the control specimen. In the case of ductility, all specimens demonstrated ductile behavior, although the ductility index was slightly decreased in control and SFRC specimens. Therefore, it can be concluded that replacing the damaged concrete cover with SFRC is adequate to repair the blast-damaged members if the longitudinal reinforcements were not failed.

## Data Availability

The data used to support the findings of this study are available from the corresponding author upon request.

## Conflicts of Interest

The authors declare that they have no conflicts of interest.

## Acknowledgments

This work was supported by the National Research Foundation of Korea (NRF) grant funded by the Korean Government (Ministry of Education, Science and Technology (MEST)) (NRF-2017K1A3A1A12073381).

## References

- [1] T. Krauthammer, *Modern Protective Structures*, CRC Press, 2008.
- [2] A. F. Ashour, S. A. El-Refaie, and S. W. Garrity, "Flexural strengthening of RC continuous beams using CFRP laminates," *Cement and Concrete Composites*, vol. 26, no. 7, pp. 765–775, 2004.
- [3] X. L. Bao and B. Li, "Residual strength of blast damaged reinforced concrete columns," *International Journal of Impact Engineering*, vol. 37, no. 3, pp. 295–308, 2010.
- [4] P. A. Buchan and J. F. Chen, "Blast resistance of FRP composites and polymer strengthened concrete and masonry structures – a state-of-the-art review," *Composites Part B: Engineering*, vol. 38, no. 5–6, pp. 509–522, 2007.
- [5] R. P. Burrell, H. Aoude, and M. Saatcioglu, "Response of SFRC columns under blast loads," *Journal of Structural Engineering*, vol. 141, no. 9, article 04014209, 2015.
- [6] J. E. Crawford, "State of the art for enhancing the blast resistance of reinforced concrete columns with fiber-reinforced plastic," *Canadian Journal of Civil Engineering*, vol. 40, no. 11, pp. 1023–1033, 2013.
- [7] E. David, C. Djelal, and F. Buyle-Bodin, *Repair and Strengthening of Reinforced Concrete Beams Using Composite Materials*, [Ph.D. thesis], 2nd International PhD Symposium in Civil Engineering, Budapest, Hungary, 1998.
- [8] H. M. Elsanadedy, T. H. Almusallam, H. Abbas, Y. A. Al-Salloum, and S. H. Alsayed, "Effect of blast loading on CFRP-retrofitted RC columns – a numerical study," *Latin American Journal of Solids and Structures*, vol. 8, no. 1, pp. 55–81, 2011.
- [9] K. Fujikake and P. Aemlaor, "Damage of reinforced concrete columns under demolition blasting," *Engineering Structures*, vol. 55, pp. 116–125, 2013.
- [10] M. Jumaat, M. Kabir, and M. Obaydullah, "A review of the repair of reinforced concrete beams," *Journal of Applied Science Research*, vol. 2, no. 6, pp. 317–326, 2006.
- [11] J. Y. Lee, D. B. Kim, T. Yuan, and Y. S. Yoon, "Effect of blast local damage on flexural strength of RC beams and blast resistance according to variation of shear rebar placement," *Journal of Korean Society of Hazard Mitigation*, vol. 15, no. 2, pp. 71–77, 2015.
- [12] J.-Y. Lee, D.-S. Jang, K.-Y. Kwon, and Y.-S. Yoon, "Evaluation of local damages and residual performance of blast damaged RC beams strengthened with steel fiber and FRP sheet," *Journal of the Korea Concrete Institute*, vol. 26, no. 5, pp. 627–634, 2014.
- [13] J.-Y. Lee, H.-O. Shin, D.-Y. Yoo, and Y.-S. Yoon, "Structural response of steel-fiber-reinforced concrete beams under various loading rates," *Engineering Structures*, vol. 156, pp. 271–283, 2018.
- [14] C. A. Ross, M. Purcell, and E. L. Jerome, "Blast response of concrete beams and slabs externally reinforced with fiber reinforced plastics (FRP)," in *Building to Last: ASCE*, pp. 673–677, American Society of Civil Engineers, 1997.
- [15] P. F. Silva and B. Lu, "Improving the blast resistance capacity of RC slabs with innovative composite materials," *Composites Part B: Engineering*, vol. 38, no. 5–6, pp. 523–534, 2007.
- [16] C. Wu, D. J. Oehlers, M. Rebertost, J. Leach, and A. S. Whittaker, "Blast testing of ultra-high performance fibre and FRP-retrofitted concrete slabs," *Engineering Structures*, vol. 31, no. 9, pp. 2060–2069, 2009.
- [17] K. C. Wu, B. Li, and K. C. Tsai, "Residual axial compression capacity of localized blast-damaged RC columns," *International Journal of Impact Engineering*, vol. 38, no. 1, pp. 29–40, 2011.
- [18] K. Xu and Y. Lu, "Numerical simulation study of spallation in reinforced concrete plates subjected to blast loading," *Computers and Structures*, vol. 84, no. 5–6, pp. 431–438, 2006.

- [19] J. Yu, T. Rinder, A. Stolz, K. H. Tan, and W. Riedel, "Dynamic progressive collapse of an RC assemblage induced by contact detonation," *Journal of Structural Engineering*, vol. 140, no. 6, p. 04014014, 2014.
- [20] C. F. Zhao and J. Y. Chen, "Damage mechanism and mode of square reinforced concrete slab subjected to blast loading," *Theoretical and Applied Fracture Mechanics*, vol. 63-64, pp. 54-62, 2013.
- [21] M. Saatcioglu, T. Ozbakkaloglu, N. Naumoski, and A. Lloyd, "Response of earthquake-resistant reinforced-concrete buildings to blast loading. This article is one of a selection of papers published in the Special Issue on Blast Engineering," *Canadian Journal of Civil Engineering*, vol. 36, no. 8, pp. 1378-1390, 2009.
- [22] S.-H. Cho, K.-H. Min, Y.-J. Kim, and Y.-S. Yoon, "Impact resistance evaluation of RC beams strengthened with carbon FRP sheet and steel fiber," *Journal of the Korea Concrete Institute*, vol. 22, no. 5, pp. 719-725, 2010.
- [23] J. H. Ha, N. H. Yi, J. K. Choi, and J. H. J. Kim, "Experimental study on hybrid CFRP-PU strengthening effect on RC panels under blast loading," *Composite Structures*, vol. 93, no. 8, pp. 2070-2082, 2011.
- [24] L. Li, J. Y. Lee, K. H. Min, and Y. S. Yoon, "Evaluating local damages and blast resistance of RC slabs subjected to contact detonation," *Journal of the Korea Institute for Structural Maintenance and Inspection*, vol. 17, no. 1, pp. 37-45, 2013.
- [25] L. J. Malvar, J. E. Crawford, and K. B. Morrill, "Use of composites to resist blast," *Journal of Composites for Construction*, vol. 11, no. 6, pp. 601-610, 2007.
- [26] K. M. Mosalam and A. S. Mosallam, "Nonlinear transient analysis of reinforced concrete slabs subjected to blast loading and retrofitted with CFRP composites," *Composites Part B: Engineering*, vol. 32, no. 8, pp. 623-636, 2001.
- [27] A. Ghani Razaqpur, A. Tolba, and E. Contestabile, "Blast loading response of reinforced concrete panels reinforced with externally bonded GFRP laminates," *Composites Part B: Engineering*, vol. 38, no. 5-6, pp. 535-546, 2007.
- [28] P. Murnal and R. Chatorikar, "Impact resistance of steel fiber reinforced concrete," *International Journal of Research in Engineering and Technology*, vol. 4, p. 13, 2015.
- [29] S. R. Lan, T. S. Lok, and L. Heng, "Composite structural panels subjected to explosive loading," *Construction and Building Materials*, vol. 19, no. 5, pp. 387-395, 2005.
- [30] 318 AC, *Building Code Requirements for Structural Concrete and Commentary (ACI 318-14)*, ACI Committee 318, 2014.
- [31] International A, *ASTM C39 Standard Test Method for Compressive Strength of Cylindrical Concrete Specimens*, ASTM International, 2001.
- [32] International A, *ASTM C1609 Standard Test Method for Flexural Performance of Fiber-Reinforced Concrete (Using Beam with Third-Point Loading)*, ASTM International, 2012.
- [33] M. Yamaguchi, K. Murakami, K. Takeda, and Y. Mitsui, "Blast resistance of polyethylene fiber reinforced concrete to contact detonation," *Journal of Advanced Concrete Technology*, vol. 9, no. 1, pp. 63-71, 2011.

## Research Article

# Bond Behavior of Wet-Bonded Carbon Fiber-Reinforced Polymer-Concrete Interface Subjected to Moisture

Yiyuan Lu , Tao Zhu , Shan Li , and Zhenzhen Liu

School of Civil Engineering, Wuhan University, Wuhan 430072, China

Correspondence should be addressed to Shan Li; [lishan@whu.edu.cn](mailto:lishan@whu.edu.cn)

Received 10 October 2017; Revised 9 January 2018; Accepted 13 February 2018; Published 14 March 2018

Academic Editor: Young Hoon Kim

Copyright © 2018 Yiyuan Lu et al. This is an open access article distributed under the Creative Commons Attribution License, which permits unrestricted use, distribution, and reproduction in any medium, provided the original work is properly cited.

The use of carbon fiber-reinforced polymer (CFRP) composite materials to strengthen concrete structures has become popular in coastal regions with high humidity levels. However, many concrete structures in these places remain wet as a result of tides and wave-splashing, so they cannot be completely dried before repair. Therefore, it is vital to investigate the effects of moisture on the initial and long-term bond behavior between CFRP and wet concrete. This research assesses the effects of moisture (i) during CFRP application and (ii) throughout the service life. Before CFRP bonding, the concrete blocks are preconditioned with a water content of 4.73% (termed “wet-bonding”). Three different epoxy resins are applied to study the bond performance of the CFRP-concrete interface when subjected to moisture (95% relative humidity). A total of 45 double-lap shear specimens were tested at the beginning of exposure and again after 1, 3, 6, and 12 months. All specimens with normal epoxy resins exhibited adhesive failure. The failure mode of specimens with hydrophobic epoxy resin changed from cohesive failure to mixed cohesive/adhesive failure and to adhesive failure according to the duration of exposure. Under moisture conditioning, the maximum shear stress ( $\tau_{\max}$ ) and corresponding slip ( $s_{\max}$ ) of the bond-slip curve first increased and then decreased or fluctuated over time. The same tendency was seen in the ultimate strain transmitted to the CFRP sheet, the interfacial fracture energy ( $G_f$ ), and the ultimate load ( $P_u$ ). Analytical models of  $G_f$  and  $P_u$  for the CFRP-concrete interface under moisture conditioning are presented.

## 1. Introduction

The use of fiber-reinforced polymer (FRP) composites has emerged as one of the most promising techniques in the field of concrete structural strengthening [1–4] due to their well-established advantages, which include a high strength-weight ratio, fatigue resistance, ease of installation, and cost-effectiveness [5–9]. Of the various types of FRP composites, carbon fiber-reinforced polymer (CFRP) is used extensively for rehabilitation of concrete structures. It has shown outstanding performance when used for strengthening concrete structures, providing improvement of load carrying capacity, stiffness, or ductility. Although CFRP composites provide an effective method to strengthen concrete structures, the effectiveness of strengthening system mainly depends on the durability of adhesive bond between CFRP and concrete substrate [10–12].

In coastal regions such as southern China, Hong Kong, many concrete structures are wet at the time of repair and

the CFRP-strengthened systems are subjected to moisture, under the influence of tides and wave-splashing. Therefore, the performance of CFRP in strengthening wet concrete should be well recognized for further application, and various methods have been studied. Zhou and Lucas [13] revealed that water sorption could modify the mechanical properties of epoxy resins. Tatar and Hamilton [14] reported that moisture had a negative effect on the adhesion properties of epoxy resin. Choi et al. [15] studied the CFRP bond capacity under hygrothermal exposure using a new three-point bend beam test. The results suggested that CFRP-concrete bond systems using different epoxies showed significant differences in durability, although the same type of fibers and the same type of concrete specimens were used. Tuakta and Büyükcöztürk [16] conducted cyclic moisture conditioning tests and found that the adhesive bond cannot regain its original bond strength after successive wet-dry cycles at both room and high temperatures. Wan et al. [17] used modified double cantilever beam (MDCB) specimens to study the effects of water on

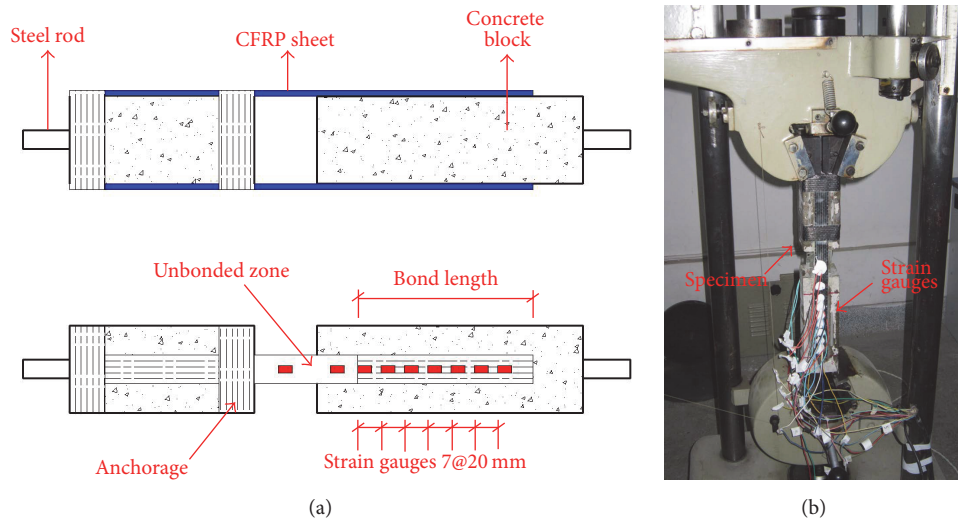


FIGURE 1: Test arrangement: (a) details of specimen; (b) photograph of test setup.

the CFRP-concrete bond during CFRP application and after CFRP curing. The results indicated that the presence of water during primer application caused a significant decrease in the bond quality. When a water-tolerant primer was applied, the bond strength increased, but it was not comparable to that of a dry-bonded specimen using the normal primer. The bond performance continued to degrade with exposure. The presence of water also changed the mode of failure from cohesive within the concrete to adhesive along the concrete-to-primer interface. Dai et al. [18] studied the effects of moisture on the initial and long-term bonding behavior of the CFRP-concrete interface using various primers and concluded that moisture strongly influenced the bond performance and that the application of an appropriate primer can eliminate the effects of concrete surface moisture on short-term interfacial bond performance. The failure mode changed from cohesive failure to interfacial failure, and the bond strength continued to degrade with moisture exposure. However, previous research studies have focused on the performance and duration of concrete members strengthened with conventional CFRP composites. Recently, a few studies have been conducted on the use of high modulus CFRP to strengthen concrete structures. Richardson [19] investigated the use of high modulus CFRP plate to strengthen damaged reinforced concrete beams. The results showed that the 400 GPa CFRP of reinforcement ratio 0.17% increased the ultimate strength of concrete beam by up to 51% and enhanced flexural stiffness in the elastic and plastic ranges by 8% and 12%. He also developed an analytical model to predict the performance of high modulus FRP-strengthened slender RC columns. Sadeghian and Fam [20] introduced a technique that aims at controlling second-order lateral deflection using longitudinal high modulus bonded reinforcement. Therefore it was encouraging to investigate the duration of high modulus CFRP-strengthened concrete structures.

This paper presents the experimental results from a series of high modulus CFRP-concrete double-lap specimens

with the following purposes: (i) characterize the debonding process using mechanical parameters after moisture conditioning and (ii) provide reference for the establishment of relative strengthening codes. Three ambient-cured epoxy resins obtained from different suppliers, two conventional types (WSX [represented by A] and MA [represented by B]) and a hydrophobic type (CH-3 [represented by C]), are used in this study. Epoxy resin WSX is popularly used for dry concrete substrate and epoxy resin MA can be used for dry and wet concrete substrate, whereas epoxy resin CH-3 is particularly formulated for use in wet, damp, or moist concrete substrates and is used to verify whether the hydrophobic epoxy resin can better cope with moisture at the CFRP-concrete interface over both short and long terms. Comparisons are presented on failure modes, bond-slip relationships, interfacial fracture energy, and ultimate loads.

## 2. Experimental Program

**2.1. Test Specimen.** The 45 conditioned specimens were mechanically tested to failure in standard laboratory conditions. The duration of exposure to moisture was the only variable that was changed during the experiment. Because three different epoxy resins were used, these specimens were divided into three main groups. Each group was conditioned for 0, 1, 3, 6, and 12 months. All double-lap shear specimens are named in the form of RH-*x*-*y*-*z*. For example, RH-A-6-2 is specimen number 2 with epoxy resin A subjected to 95% relative humidity (RH) for 6 months before testing.

**2.2. Preparation of Specimen.** Figure 1(a) shows a schematic view of the CFRP-concrete double-lap shear specimen. The 25 mm CFRP sheet is centered along the longitudinal axis of the 75 mm concrete block, leaving two 25 mm shoulders on the side of the bond to remove edge effects. The bond length is 150 mm, and a 35 mm unbonded zone is left to avoid the loss of a concrete chunk by shearing near the loaded end

TABLE 1: Material properties of CFRP coupon and epoxy resin.

Material	Young's modulus (GPa)	Ultimate strength (MPa)	Shear strength (MPa)	Failure strain (%)
CFRP	245	3870	—	1.74
CFRP-A	266	3933	—	1.48
CFRP-B	268	3968	—	1.48
CFRP-C	292	4428	—	1.52
Epoxy A	2.4	33	21	1.40
Epoxy B	2.7	45	22	1.84
Epoxy C	4.5	48	26	1.65

Note. CFRP-A: CFRP coupon using epoxy resin A; CFRP-B: CFRP coupon using epoxy resin B; CFRP-C: CFRP coupon using epoxy resin C.

[21, 22]. The concrete blocks are cast using wooden molds, demolded after 24 hours, and cured for 28 days. Afterwards, all concrete blocks are submerged in salt water for 1 year so that the concrete's compressive strength remains stable during moisture exposure. The bonding sides of the concrete blocks are then sandblasted with a hand grinder to provide appropriate rough surfaces for bonding, and any debris, grease, laitance, and loose material at the surface are cleaned with acetone using a cotton cloth. To investigate the effects of the presence of water before bonding the CFRP sheets, the concrete substrate surfaces are preconditioned to simulate the construction conditions that may be encountered in a moist environment. All concrete blocks are submerged in deionized water for 3 days, removed, and wiped to measure the absorbed water. The difference in the weight of the concrete before and after conditioning represents the moisture mass uptake. In this process, the measured average moisture content of the concrete is 4.73%. After measurement of moisture, the fully saturated CFRP sheet is carefully placed on the designed region of the concrete block upon which epoxy has been applied. A roller is used to squeeze out excessive epoxy until a uniform bonding layer is formed. In a similar manner, two 30 mm-wide CFRP hoops with the fibers oriented in the transverse direction are wrapped to provide sufficient anchorage so that failure takes place at the bonded zone. All specimens are then cured in the laboratory for 1 week at ambient temperatures. It should be noted that, in the wet-layup system, epoxy resin is used to bond the CFRP sheet to concrete and at the same time serves as saturation resin for the CFRP sheet.

**2.3. Moisture Conditioning.** All specimens are conditioned at  $20^{\circ}\text{C} \pm 1^{\circ}\text{C}$  and  $95\% \pm 3\%$  RH inside a conditioning chamber in a laboratory with moisture control. At each target exposure duration (i.e., 0, 1, 3, 6, and 12 months), three randomly chosen specimens for each epoxy resin are removed periodically for testing.

**2.4. Material Properties.** The concrete blocks are made from grade 42.5 Portland cement and aggregates with a maximum size of 15 mm. The blocks are cast and cured following GB50010-2010 [23]. The average concrete cube strength after 1 year of immersion is 33.5 MPa, determined with three  $150 \times 150 \times 150$  mm concrete cubes. The CFRP sheet with

a thickness of 0.167 mm is "NG" brand and supplied by Wuda Jucheng, a company in China. Table 1 presents its material properties according to the product data sheet. The properties of flat coupons made with different epoxy resins are determined from tensile tests in accordance with ASTM D3039 [24] and are shown in Table 1. CFRP coupons are made using the wet lay-up process. First, the CFRP sheets are brushed with mixed epoxy resin. Second, the CFRP sheets are cut into 15 mm wide  $\times$  250 mm long sections after 7-day curing at ambient temperature. Third, CFRP tabs and aluminum tabs are bonded at the two ends. Each coupon is tested using a universal testing machine at a speed of 1 mm/min, with a strain gauge adopted on the center. The three commercial two-part epoxy resins chosen for the current program, both as CFRP matrices and as adhesives, are (1) WSX epoxy resin (represented by A), (2) MA epoxy resin (represented by B), and (3) CH-3 epoxy resin (represented by C). Table 1 summarizes their material properties according to the material data sheet supplied by their manufacturers.

**2.5. Test Setup and Instrumentation.** Before testing, all specimens are fitted with nine quarter-bridge strain gauges bonded to the CFRP's outer surface. Seven strain gauges in the bonded zone with a spacing of 20 mm are used to measure the strain distribution along the CFRP sheet at various loading levels, and the other two in the unbonded zone are used to record the tensile load. Strain measurement is recorded by an electronic acquisition system. The double-lap shear tests are carried out in standard laboratory conditions with a universal hydraulic testing machine (capacity of 100 kN) displacement controlled at 0.5 mm/min. After the specimen is rigidly clamped by steel rods at both ends, preliminary testing is conducted to carefully adjust the alignment of two symmetric CFRP sheets and clamps so the load can be transferred uniformly into the CFRP-concrete interface. The specimen is then tested individually in direct tension until the CFRP sheets are entirely pulled off (as shown in Figure 1). It should be noted that, for this double-lap specimen, the CFRP sheets of two sides would be peeled off in sequence. After one side is peeled off, the total load is suddenly applied eccentrically on the opposite side. Therefore, only the strain measurements of the first failure side are reported in this study.

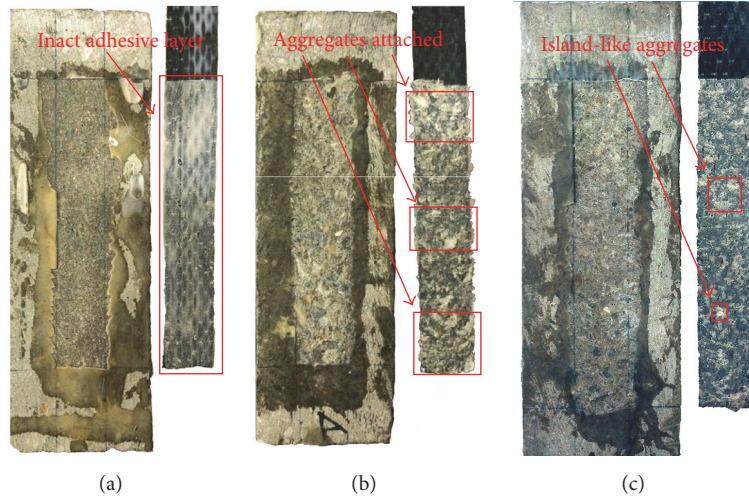


FIGURE 2: Typical failure modes: (a) adhesive failure; (b) cohesive failure; (c) mixed cohesive/adhesive failure.

### 3. Experimental Results

**3.1. Failure Mode.** Three predominant failure modes were observed: adhesive failure, cohesive failure, and mixed cohesive/adhesive failure. Adhesive failure occurs between the epoxy and the concrete substrate, with or without loose concrete remaining on the CFRP sheet. Cohesive failure occurs inside the concrete block near the epoxy-concrete contact surface, and many particles of coarse and fine aggregate are attached to the surface that failed. Mixed cohesive/adhesive failure is a combination of cohesive failure and adhesive failure. Table 2 summarizes the failure modes of all specimens, and Figure 2 presents selected images of failed specimens (the left part shows substrates after peeling, and the right part shows peeled CFRP sheets).

When the concrete substrates are wet, specimens RH-A-0-z and RH-B-0-z are representative of adhesive failure (Figure 2(a)). The peeled part consists of the CFRP sheet and an almost-intact adhesive layer without adhering aggregates. This failure mode differs from that observed in other studies when concrete is dry [25, 26], which indicates that the initial wet concrete substrate has a negative effect on the bond between epoxy resin and concrete because the hydrogen bonds between the epoxy and the concrete substrate may be disturbed by the presence of water molecules at the interface [27]. With the increase in moisture exposure, all series RH-A-y-z and RH-B-y-z specimens show adhesive failure. This means that the effectiveness of mechanical bond was weakened. And it can be contributed to the residual water within concrete surface and the degradation properties of epoxy resins [28, 29].

In contrast, most samples with hydrophobic epoxy specimens exhibit various degrees of cohesive failure (Figure 2(b)). The failure begins near the loaded end and then cracks kinks into the concrete substrate and propagates parallel to the interface until CFRP sheets are pulled off. Many aggregates are attached to the CFRP sheet. Nevertheless, after 3 months of exposure, one conditioned specimen displays

a mixed cohesive/adhesive failure in the concrete, with a relatively small amount of island-like residual aggregates remaining (Figure 2(c)). Fewer aggregates are attached on the CFRP sheet as the duration of exposure increases. When conditioning up to 12 months, the failure of specimen RH-C-12 is characteristic of adhesive failure. The negligible amount of mortar or fine aggregate bonded on the CFRP sheet is indicative of the poor bond between the epoxy and the concrete. This result indicates that, after long exposures, moisture could greatly influence the durability of the epoxy-concrete interface. The failure shift is thought to be due to (i) the possibility of resin degradation because of moisture reaction or chain scission and (ii) the reduction of interface bonding caused by water presence via water absorption or moisture diffusion. Therefore, for long exposures, this deterioration renders the epoxy-concrete interface the weakest link of the CFRP-strengthened system, resulting in adhesive failure between the epoxy and the concrete.

**3.2. Bond-Slip Relationship.** Based on the linear elastic assumption and Hook's law, the average bond shear stress between two adjacent strain gauges ( $\tau_{av}$ ) can be obtained via strain measurement along the CFRP sheet by the following equation:

$$\tau_{av} = \frac{E_f t_f (\varepsilon_i - \varepsilon_{i-1})}{\Delta x} \quad i \in (2, \dots, 7), \quad (1)$$

where  $E_f$  and  $t_f$  are the elastic modulus and thickness of the CFRP sheet and  $\varepsilon_i - \varepsilon_{i-1}$  is the axial strain difference between adjacent CFRP strains at locations  $i$  and  $i-1$ , which are separated by a distance  $\Delta x$ .

Neglecting the concrete strain, the relative slip ( $s_i$ ) at gauge location  $i$  can be written as

$$s_i = \frac{\Delta x}{2} \left( \varepsilon_1 + 2 \sum_{j=2}^{i-1} \varepsilon_j + \varepsilon_i \right) \quad i \in (2, \dots, 7), \quad (2)$$

TABLE 2: Test results of all specimens.

Specimen ID	Exposure (month)	$\tau_{\max}$ (MPa)	Average $\tau_{\max}$	$S_{\max}$ (mm)	Average $S_{\max}$	$G_f$ (N·mm/mm <sup>2</sup> )	Average $G_f$	$P_u$ (kN)	Average $P_u$	Failure mode
RH-A-0-1		5.464		0.034		0.229		3.619		AD
RH-A-0-2	0	5.875	5.670	0.041	0.038	0.348	0.277	4.508	4.364	AD
RH-A-0-3		5.670		0.039		0.254		4.964		AD
RH-A-1-1		7.422		0.057		0.625		5.255		AD
RH-A-1-2	1	6.337	6.021	0.033	0.043	0.375	0.406	4.462	4.786	AD
RH-A-1-3		4.304		0.038		0.219		4.641		AD
RH-A-3-1		4.999		0.066		0.363		3.931		AD
RH-A-3-2	3	7.475	6.036	0.048	0.051	0.493	0.395	4.657	4.468	AD
RH-A-3-3		5.636		0.037		0.328		4.817		AD
RH-A-6-1		4.640		0.045		0.262		3.639		AD
RH-A-6-2	6	5.709	5.103	0.040	0.038	0.320	0.274	4.324	4.023	AD
RH-A-6-3		4.960		0.027		0.240		4.105		AD
RH-A-12-1		5.057		0.039		0.253		3.887		AD
RH-A-12-2	12	3.315	4.192	0.036	0.035	0.164	0.206	4.311	3.898	AD
RH-A-12-3		4.204		0.031		0.200		3.497		AD
RH-B-0-1		5.521		0.039		0.252		3.820		AD
RH-B-0-2	0	6.179	5.685	0.041	0.042	0.324	0.287	4.587	4.179	AD
RH-B-0-3		5.355		0.044		0.285		4.130		AD
RH-B-1-1		5.215		0.049		0.404		4.666		AD
RH-B-1-2	1	5.649	5.491	0.038	0.043	0.336	0.350	4.111	4.453	AD
RH-B-1-3		5.609		0.041		0.311		4.582		AD
RH-B-3-1		6.144		0.039		0.397		4.734		AD
RH-B-3-2	3	5.708	6.249	0.036	0.040	0.267	0.376	4.417	4.667	AD
RH-B-3-3		6.894		0.044		0.463		4.850		AD
RH-B-6-1		5.084		0.052		0.366		4.671		AD
RH-B-6-2	6	4.913	5.598	0.035	0.046	0.286	0.365	4.451	4.590	AD
RH-B-6-3		6.797		0.051		0.443		4.649		AD
RH-B-12-1		3.560		0.036		0.224		4.127		AD
RH-B-12-2	12	5.478	4.519	0.037	0.037	0.263	0.243	4.141	4.134	AD
RH-B-12-3		—		—		—		—		AD
RH-C-0-1		7.819		0.048		0.499		5.307		CO
RH-C-0-2	0	9.841	8.842	0.053	0.050	0.710	0.572	6.532	5.662	CO
RH-C-0-3		8.865		0.050		0.507		5.146		CO
RH-C-1-1		8.172		0.056		0.850		7.148		CO
RH-C-1-2	1	10.495	9.600	0.056	0.058	0.864	0.887	6.562	6.725	CO
RH-C-1-3		10.132		0.062		0.948		6.464		CO
RH-C-3-1		8.067		0.057		0.517		5.345		CO
RH-C-3-2	3	5.895	7.163	0.049	0.063	0.368	0.554	4.997	5.747	C/A
RH-C-3-3		7.528		0.082		0.776		6.900		CO
RH-C-6-1		5.868		0.051		0.563		5.941		AD
RH-C-6-2	6	7.778	7.492	0.088	0.064	0.671	0.611	6.145	6.212	C/A
RH-C-6-3		8.830		0.054		0.597		6.551		C/A
RH-C-12-1		9.332		0.050		0.471		5.601		AD
RH-C-12-2	12	—	8.182	—	0.051	—	0.487	—	5.586	AD
RH-C-12-3		7.032		0.052		0.504		5.571		AD

Note. AD: adhesive failure; CO: cohesive failure; C/A: mixed cohesive/adhesive failure.

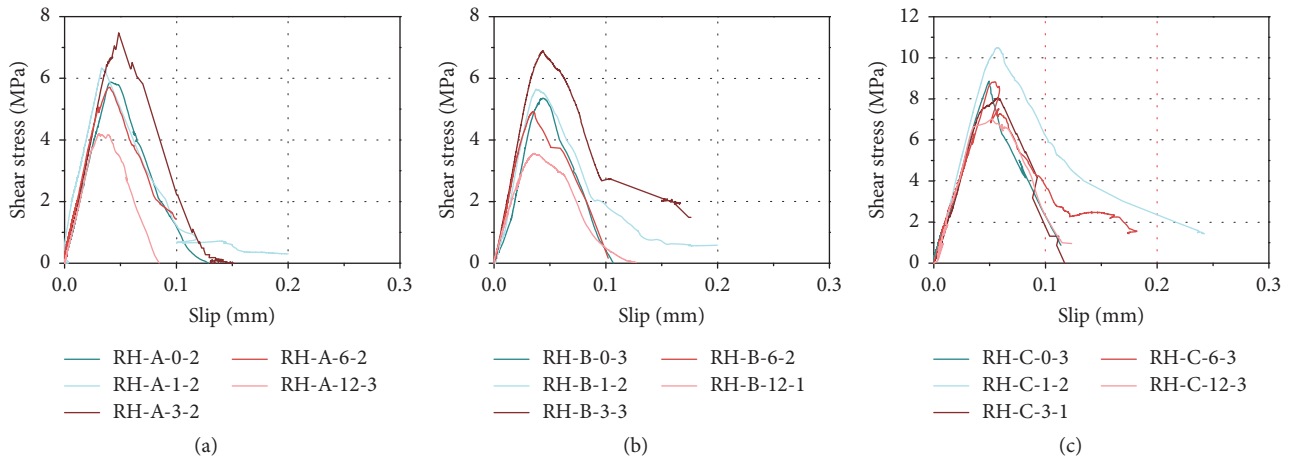


FIGURE 3: Representative bond-slip curves at the loaded end: (a) RH-A- $y$ - $z$  specimens; (b) RH-B- $y$ - $z$  specimens; (c) RH-C- $y$ - $z$  specimens.

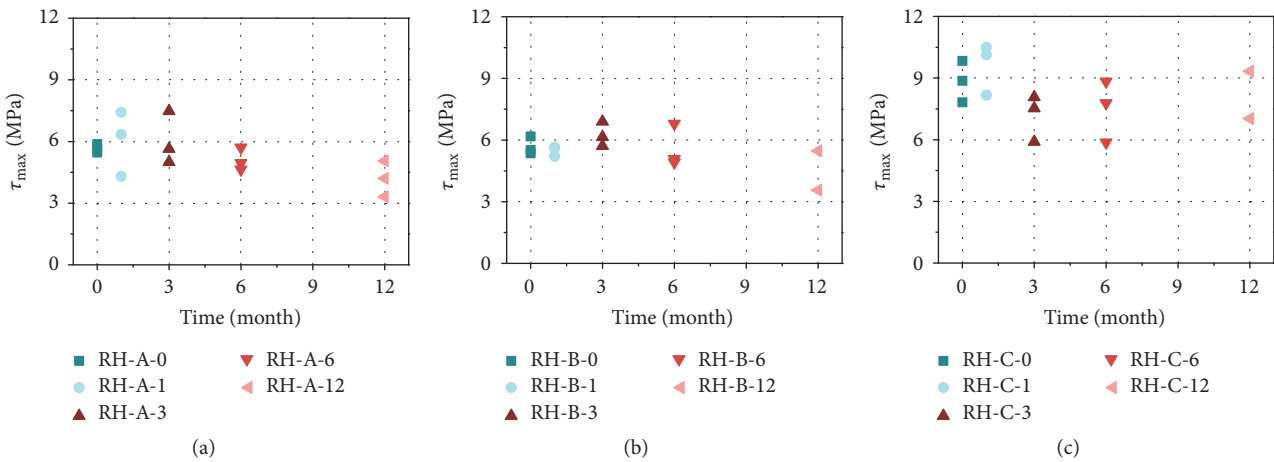


FIGURE 4: Comparison of  $\tau_{\max}$  for specimens: (a) RH-A- $y$ - $z$  specimens; (b) RH-B- $y$ - $z$  specimens; (c) RH-C- $y$ - $z$  specimens.

where  $\varepsilon_1$  is the strain at the free end of the CFRP sheet;  $\varepsilon_j$  is the strain of  $j$ th gauge attached to the CFRP sheet; and  $\varepsilon_i$  is the strain at the loaded end of the CFRP sheet. Combining (1) and (2) yields the  $\tau$ - $s$  curve along the CFRP-concrete interface.

Plotting all of the curves in one figure may result in overlapping, so it is difficult to characterize the effects of moisture. For simplicity, therefore, only one representative curve for specimens at each target exposure time is presented in Figure 3, in which all  $\tau$ - $s$  curves exhibit a bilinear shape. It is found that the exposure has little effect on the initial stiffness of the upward section, but it significantly influences the maximum shear stress ( $\tau_{\max}$ ), the corresponding slip ( $s_{\max}$ ), and the area under the curve. To characterize the effects of moisture exposure, all values of  $\tau_{\max}$  and  $s_{\max}$  are plotted in Figures 4 and 5, respectively. For the RH-A- $y$ - $z$  specimens, a synchronous change of  $\tau_{\max}$  and  $s_{\max}$  is observed, increasing in the first 3 months and decreasing with longer exposure. For the RH-B- $y$ - $z$  specimens, after a slight inverse variation at 1 month of exposure,  $\tau_{\max}$  and  $s_{\max}$  increase at 3 months and then decrease gradually. For the RH-C- $y$ - $z$  specimens,  $\tau_{\max}$  reaches a maximum at 1 month of exposure and then fluctuates over time, whereas  $s_{\max}$  shows

progressive growth up to 6 months with a final drop at 12 months. The values increase in the first few months because the postcuring effect of adhesive layer enhances the interfacial bonding even in a moist environment. However, due to the different properties of these three epoxy resins, the highest  $\tau_{\max}$  and  $s_{\max}$  values are achieved after different exposure durations, because the mechanical properties of CFRP sheet remain almost unaffected under accelerated conditioning [30, 31] and the concrete compressive strength is almost unchanged. One possible reason for the decreasing trend is that the absorbed water, acting as a plasticizer, usually reduces both mechanical and adhesion properties of epoxy resin during conditioning [17]. This phenomenon would increase the porosity and flaws within the epoxy resin, which in turn would have a detrimental effect on the interfacial shear strength.

Figure 6 compares the CFRP strain distribution along the bond length with some representative examples. In general, all specimens behave similarly, showing a more or less exponential trend in the strain distribution profile. The strain initially transfers within 20 mm of the loaded end and then transfers towards the free end. Generally, the strain of the

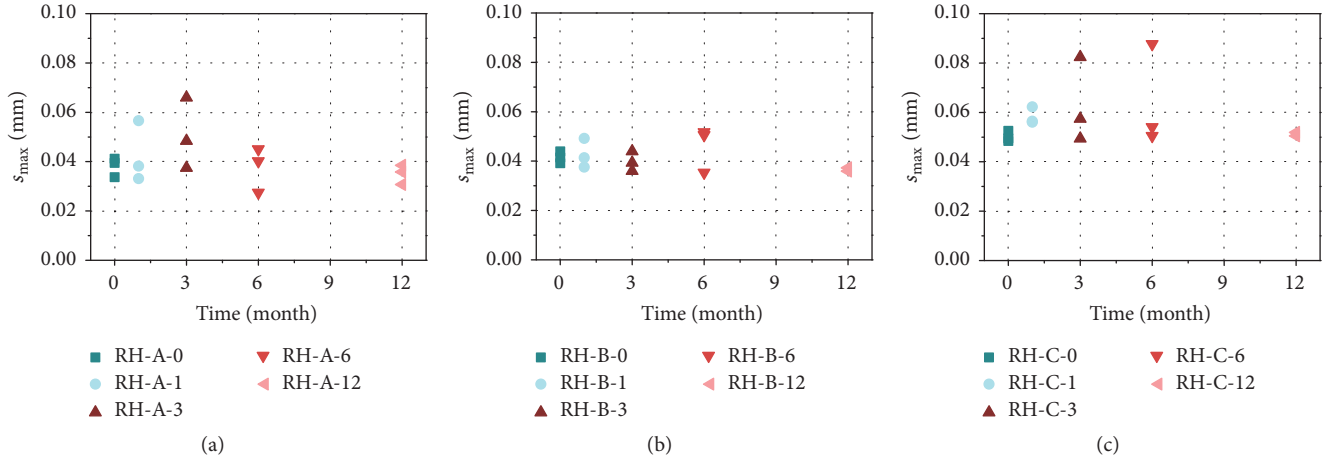


FIGURE 5: Comparison of  $s_{\max}$  for specimens: (a) RH-A- $y$ - $z$  specimens; (b) RH-B- $y$ - $z$  specimens; (c) RH-C- $y$ - $z$  specimens.

CFRP sheet decreases with an increase in the distance from the loaded end.

With the increase in the applied load, the longitudinal strain of the CFRP sheet increases. However, when the applied load reaches the failure load, the ultimate strain of the CFRP sheet is lower than  $6000 \mu\epsilon$ , which is less than half of the elongation of CFRP sheet. This means that the tensile capacity of the CFRP sheet in the CFRP-to-concrete joint cannot be fully used.

With the increase in the exposure time, almost all the longitudinal strains of the CFRP sheet beyond 80 mm from the loaded end are very limited, implying that the exposure time on the transfer length is limited. However, the specimens' ultimate strains show various trends. The ultimate strain of specimens RH-A- $y$ - $z$  achieves the highest value at 1 month and then decreases over time. The ultimate strain of specimens RH-B- $y$ - $z$  reaches the maximum at 3 months and then drops. The ultimate strain of RH-C- $y$ - $z$  fluctuates within a range of  $3500 \mu\epsilon$  to  $5500 \mu\epsilon$  and does not show the trend of monotonic change.

**3.3. Interfacial Fracture Energy.** Figure 7 presents the values of interfacial fracture energy ( $G_f$ ) in a moist environment. For RH-A- $y$ - $z$  specimens,  $G_f$  increases rapidly in the first month and remains almost unchanged until 3 months and then decreases sharply over time. For RH-B- $y$ - $z$  specimens,  $G_f$  increases until 6 months and then decreases. For RH-C- $y$ - $z$  specimens,  $G_f$  peaks at 1 month, and the general trend over the next few months is decreasing-increasing-decreasing. With respect to the maximum value of  $G_f$ , +31.77%, 0.00%, -2.71%, -32.51%, and -49.26% variation for RH-A- $y$ - $z$  specimens; +23.67%, +6.91%, +0.00%, -2.93%, and -35.37% variation for RH-B- $y$ - $z$  specimens; and +35.51%, 0.00%, -37.54%, -31.12%, and -45.10% variation for RH-C- $y$ - $z$  specimens are observed. This phenomenon could be explained by (i) the solidification of epoxy resins in the first few months and (ii) the reduction of the mechanical and adhesion properties of epoxy resin caused by water infiltration and diffusion through microcracks and voids with longer exposure. According to the variation trend shown in Figure 7, a Gaussian function

that relates the interfacial fracture energy after conditioning ( $G_{f,\text{moisture}}$ ) to the exposure time ( $t$ , months) is obtained by curve fitting:

$$G_{f,\text{moisture}} = \left( A + \frac{B}{C\sqrt{\pi/2}} e^{-2((t-t_c)^2/C^2)} \right) G_f, \quad (3)$$

where  $A$  is the residual factor,  $B$  and  $C$  are constants,  $t_c$  is the time when the highest fracture energy is attained, and  $G_f$  is the interfacial fracture energy of the 0-month specimens. For the RH-A- $y$ - $z$  specimens,  $A$ ,  $B$ ,  $C$ , and  $t_c$  achieved by regression analysis are 0.84, 2.70, 3.37, and 3.19, respectively. For the RH-B- $y$ - $z$  specimens,  $A$ ,  $B$ ,  $C$ , and  $t_c$  are 0.83, 5.78, and 4.24, respectively. For the RH-C- $y$ - $z$  specimens,  $A$ ,  $B$ ,  $C$ , and  $t_c$  are 0.85, 3.23, 4.32, and 2.56, respectively.

**3.4. Ultimate Load.** Figure 8 shows the values of the ultimate load ( $P_u$ ) under moisture conditioning. The average  $P_u$  of the RH-A- $y$ - $z$  specimens increases in the first month and then decreases progressively. The average values of RH-A-0- $z$  (4.364 kN), RH-A-3- $z$  (4.468 kN), RH-A-6- $z$  (4.023 kN), and RH-A-12- $z$  (3.898 kN) vary by +8.82%, -6.64%, -15.94%, and -18.55%, respectively, from that of RH-A-1- $z$  (4.786 kN). For the RH-B- $y$ - $z$  specimens, the  $P_u$  values show similar variation, and the maximum value occurs at 3 months (4.677 kN). With the duration of exposure,  $P_u$  of RH-B-6- $z$  (4.590 kN) and RH-B-12- $z$  (4.134 kN) decrease by 1.65% and 11.42%, respectively. For the RH-C- $y$ - $z$  specimens, cohesive failure inside the concrete substrate results in the highest  $P_u$ . However,  $P_u$  shows a different trend, attaining its maximum value after 1 month and then fluctuating over time. The decrease in strength is associated with a change in the failure mode from cohesive failure to mixed cohesive/adhesive failure or adhesive failure. When the duration of exposure reaches 12 months, about 16.94% loss of the ultimate load associated with adhesive failure is observed.

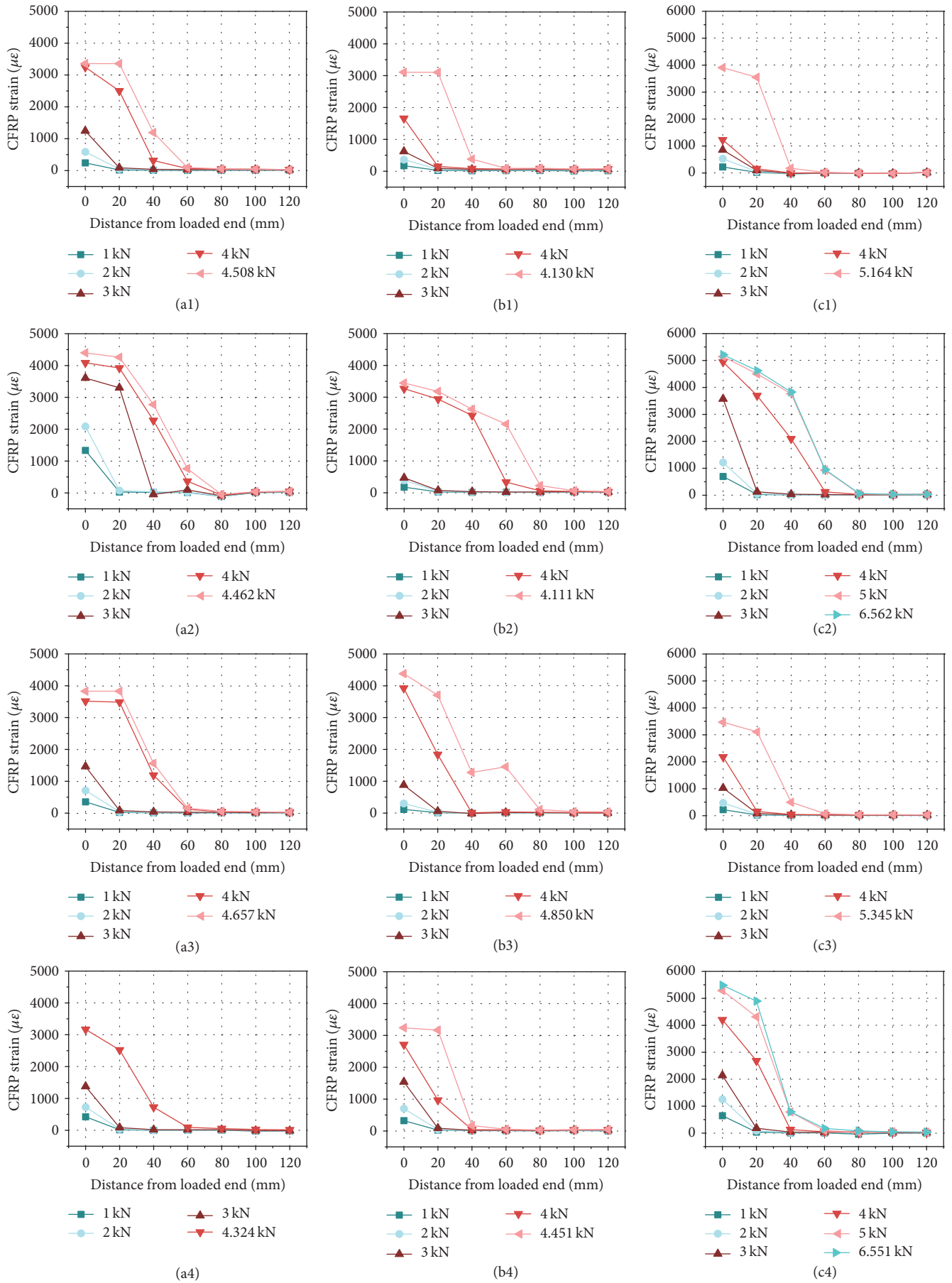


FIGURE 6: Continued.

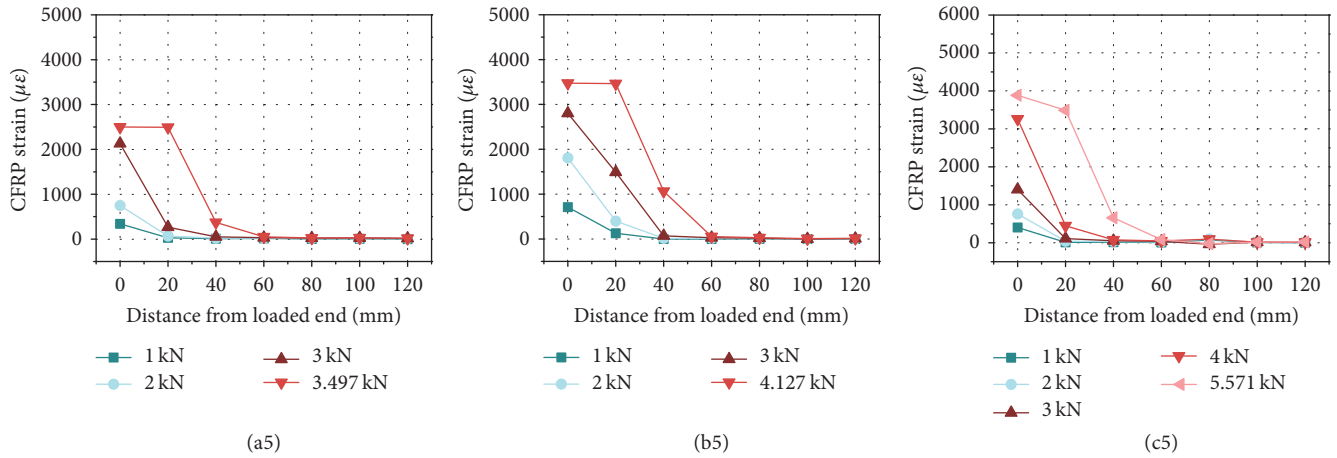


FIGURE 6: Representative CFRP strain distribution along the bonded length: (a1) RH-A-0-2; (b1) RH-B-0-3; (c1) RH-C-0-3; (a2) RH-A-1-2; (b2) RH-B-1-2; (c2) RH-C-1-2; (a3) RH-A-3-2; (b3) RH-B-3-1; (c3) RH-C-3-1; (a4) RH-A-6-3; (b4) RH-B-6-2; (c4) RH-C-6-3; (a5) RH-A-12-1; (b5) RH-B-12-1; (c5) RH-C-12-3.

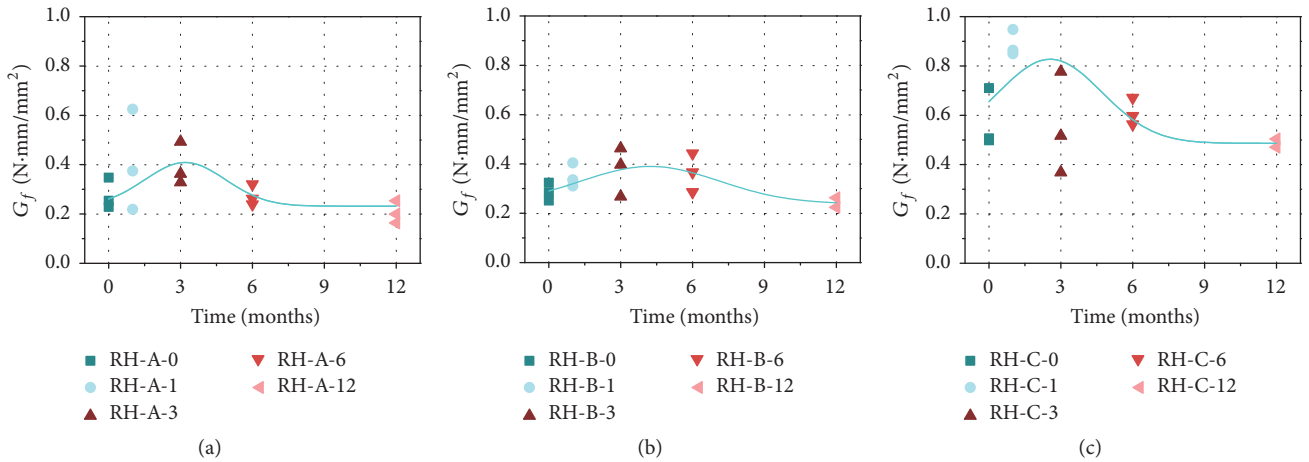


FIGURE 7: Comparison of  $G_f$  for specimens: (a) RH-A- $y$ - $z$  specimens; (b) RH-B- $y$ - $z$  specimens; (c) RH-C- $y$ - $z$  specimens.

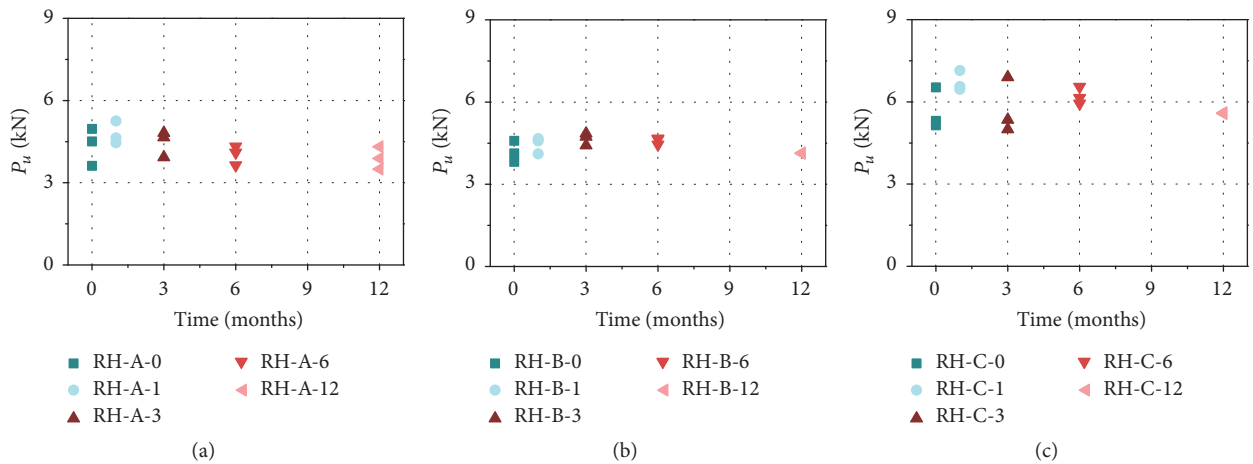


FIGURE 8: Comparison of  $P_u$  for specimens: (a) RH-A- $y$ - $z$  specimens; (b) RH-B- $y$ - $z$  specimens; (c) RH-C- $y$ - $z$  specimens.

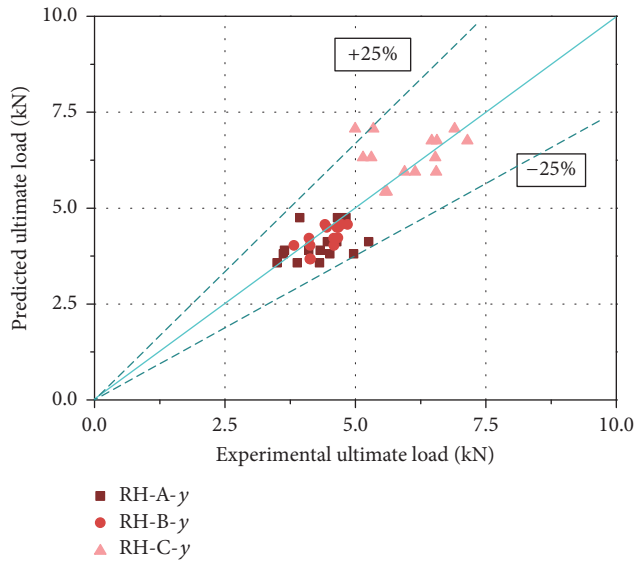


FIGURE 9: Comparison of  $P_u$  between prediction and experiments.

This phenomenon could be explained by the relationship between  $P_u$  and  $G_f$ . According to mode in [32, 33], the ultimate load is given by

$$P_u = b_f \sqrt{2E_f t_f G_f}. \quad (4)$$

Because  $E_f$  of the CFRP sheet is nearly unchanged after moisture conditioning in this study (as well as  $t_f$  and  $b_f$ ), the variation of  $P_u$  is similar to that of  $G_f$ , as discussed in Section 3.3.

Figure 9 plots a comparison of the ultimate load determined by (4) and the average value obtained experimentally for each exposure duration. The results demonstrate satisfactory agreement, with deviations of less than 25%.

#### 4. Conclusions

An experimental study was conducted with 45 wet-bonded specimens fabricated by three different epoxy resins to investigate the effects of moisture on the initial and long-term interface behavior. The following conclusions are reached within the scope of this study.

- (1) All RH-A- $\gamma$ - $z$  and RH-B- $\gamma$ - $z$  specimens exhibited an adhesive failure mode, but, for RH-C- $\gamma$ - $z$  specimens, the failure mode was obviously affected by moisture exposure. It likely changed over time from cohesive failure to mixed cohesive/adhesive failure and to adhesive failure.
- (2) A bond-slip relationship was obtained from strain reading. The CFRP-concrete interface under moisture conditioning increased during the first few months and then decreased or fluctuated over time in terms of  $\tau_{\max}$  and  $s_{\max}$ .
- (3) Moisture exposure tended to increase the ultimate strain of specimens initially, followed by a progressive decrease or fluctuation.

- (4) The interfacial fracture energy increased first and then decreased gradually or fluctuated over time. The ultimate load exhibited a similar trend of variation. Models are proposed to predict the interfacial fracture energy and ultimate load for specimens.

#### Conflicts of Interest

The authors declare that there are no conflicts of interest.

#### Acknowledgments

The tests reported herein were made possible by the financial support from the National Natural Science Foundation of China (51578428) and Special Project on Technical Innovation of Hubei (no. 2016AAA025). The authors wish to thank the technicians of School of Civil Engineering of Wuhan University for their help throughout the test process.

#### References

- [1] L. C. Hollaway, "A review of the present and future utilisation of FRP composites in the civil infrastructure with reference to their important in-service properties," *Construction and Building Materials*, vol. 24, no. 12, pp. 2419–2445, 2010.
- [2] Y. W. Zhou, Y. F. Wu, J. G. Teng, and A. Y. T. Leung, "Parametric space for the optimal design of compression-yielding FRP-reinforced concrete beams," *Materials and Structures/Materiaux et Constructions*, vol. 43, no. 1-2, pp. 81–97, 2010.
- [3] J.-G. Dai, Y.-L. Bai, and J. G. Teng, "Behavior and modeling of concrete confined with FRP composites of large deformability," *Journal of Composites for Construction*, vol. 15, no. 6, pp. 963–973, 2011.
- [4] W.-W. Wang, J.-G. Dai, and K. A. Harries, "Performance evaluation of RC beams strengthened with an externally bonded FRP system under simulated vehicle loads," *Journal of Bridge Engineering*, vol. 18, no. 1, pp. 76–82, 2013.
- [5] J. G. Teng, J. F. Chen, S. T. Smith, and L. Lam, *FRP strengthened RC structures*, Wiley, Chichester, UK, 2002.
- [6] Y. J. Kim, C. Shi, and M. F. Green, "Ductility and cracking behavior of prestressed concrete beams strengthened with prestressed CFRP sheets," *Journal of Composites for Construction*, vol. 12, no. 3, pp. 274–283, 2008.
- [7] S. Li, T. Zhu, Y. Lu, and X. Li, "Effect of Temperature Variation on Bond Characteristics between CFRP and Steel Plate," *International Journal of Polymer Science*, vol. 2016, Article ID 5674572, 2016.
- [8] Y.-W. Zhou, Y.-F. Wu, and Y. Yun, "Analytical modeling of the bond-slip relationship at FRP-concrete interfaces for adhesively-bonded joints," *Composites Part B: Engineering*, vol. 41, no. 6, pp. 423–433, 2010.
- [9] Y. Y. Lu, W. J. Li, S. Li, X. Li, and T. Zhu, "Study of the tensile properties of CFRP strengthened steel plates," *Polymer*, vol. 7, no. 12, pp. 2595–2610, 2015.
- [10] J. Tatar and H. R. Hamilton, "Bond durability factor for externally bonded CFRP systems in concrete structures," *Journal of Composites for Construction*, vol. 20, no. 1, Article ID 04015027, 2016.
- [11] M. I. Kabir, B. Samali, and R. Shrestha, "Fracture Properties of CFRP-Concrete Bond Subjected to Three Environmental

- Conditions,” *Journal of Composites for Construction*, vol. 20, no. 4, Article ID 4016010, 2016.
- [12] Z. Y. Ouyang, *Durability of bond between FRP and concrete in moist environments: Experimental, numerical and analytical study [Ph.D. thesis]*, 2007.
- [13] J. Zhou and J. P. Lucas, “Hygrothermal effects of epoxy resin. Part I: the nature of water in epoxy,” *Polymer Journal*, vol. 40, no. 20, pp. 5505–5512, 1999.
- [14] J. Tatar and H. R. Hamilton, “Effect of moisture exposure on the adhesive bond under direct shear,” in *Proceedings of the Proc. 7th Int. Conf. on FRP Composites in Civil Engineering (CICE 2014, International Institute for FRP in Construction (IIFC)*, Vancouver, Canada, 2014.
- [15] S. Choi, A. L. Gartner, N. V. Etten, H. R. Hamilton, and E. P. Douglas, “Durability of concrete beams externally reinforced with CFRP composites exposed to various environments,” *Journal of Composites for Construction*, vol. 16, no. 1, pp. 10–20, 2012.
- [16] C. Tuakta and O. Büyüköztürk, “Conceptual model for prediction of FRP-concrete bond strength under moisture cycles,” *Journal of Composites for Construction*, vol. 15, no. 5, pp. 743–756, 2011.
- [17] B. L. Wan, M. F. Petrou, and K. A. Harries, “The effect of the presence of water on the durability of bond between CFRP and concrete,” *Journal of Reinforced Plastics and Composites*, vol. 25, no. 8, pp. 875–890, 2006.
- [18] J. G. Dai, H. Yokota, M. Iwanami, and E. Kato, “Experimental investigation of the influence of moisture on the bond behavior of FRP to concrete interfaces,” *Journal of Composites for Construction*, vol. 14, no. 6, pp. 834–844, 2010.
- [19] T. Richardson, “Strengthening Damaged Reinforced Concrete Beams and Slender Columns Using Ultra-High Modulus CFRP Plates [M.S. Thesis],” Tech. Rep., 2013.
- [20] P. Sadeghian and A. Fam, “Strengthening slender reinforced concrete columns using high-modulus bonded longitudinal reinforcement for buckling control,” *Journal of Structural Engineering (United States)*, vol. 141, no. 4, Article ID 04014127, 2015.
- [21] C. Au and O. Büyüköztürk, “Peel and shear fracture characterization of debonding in FRP plated concrete affected by moisture,” *Journal of Composites for Construction*, vol. 10, no. 1, pp. 35–47, 2006.
- [22] K. Gamage, R. Al-Mahaidi, and B. Wong, “Fe modelling of CFRP-concrete interface subjected to cyclic temperature, humidity and mechanical stress,” *Composite Structures*, vol. 92, no. 4, pp. 826–834, 2010.
- [23] *Codes for design of concrete structures*, The Standardization Institute of Chinese Construction, China Planning Press, Beijing, China, 2010, GB 50010-2010.
- [24] *Standard Test Method for Tensile Properties of Polymer Matrix Composite Materials*, ASTM, West Conshohocken, PA, USA, 2008, ASTM D3039-07.
- [25] Y. Pan, G. Xian, and M. A. G. Silva, “Effects of water immersion on the bond behavior between CFRP plates and concrete substrate,” *Construction and Building Materials*, vol. 101, pp. 326–337, 2015.
- [26] K. Benzarti, S. Chataigner, M. Quertant, C. Marty, and C. Aubagnac, “Accelerated ageing behaviour of the adhesive bond between concrete specimens and CFRP overlays,” *Construction and Building Materials*, vol. 25, no. 2, pp. 523–538, 2011.
- [27] E. H. Immergut and H. F. Mark, “Principles of plasticization,” in *Plasticization and plasticizer processes*, N. A. J. Platzer, Ed., vol. 48 of *Advances in Chemistry*, pp. 1–26, American Chemical Society, Washington DC., USA, 1965.
- [28] J. Shrestha, T. Ueda, and D. Zhang, “Durability of FRP concrete bonds and its constituent properties under the influence of moisture conditions,” *Journal of Materials in Civil Engineering*, vol. 27, no. 2, Article ID A4014009, 2015.
- [29] J. Shrestha, D. Zhang, and T. Ueda, “Durability performances of carbon fiber-reinforced polymer and concrete-bonded systems under moisture conditions,” *Journal of Composites for Construction*, vol. 20, no. 5, Article ID 04016023, 2016.
- [30] H. Saadatmanesh, M. Tavakkolizadeh, and D. Mostofinejad, “Environmental effects on mechanical properties of wet lay-up fiber-reinforced polymer,” *ACI Materials Journal*, vol. 107, no. 3, pp. 267–274, 2010.
- [31] S. Li, J. Hu, and H. Ren, “The combined effects of environmental conditioning and sustained load on mechanical properties of wet lay-up fiber reinforced polymer,” *Polymer*, vol. 9, no. 7, article no. 244, 2017.
- [32] J. G. Dai, T. Ueda, and Y. Sato, “Development of the non-linear bond stress-slip model of fiber reinforced plastics sheet-concrete interfaces with a simple method,” *Journal of Composites for Construction*, vol. 9, no. 1, pp. 52–62, 2005.
- [33] J. Dai, T. Ueda, and Y. Sato, “Unified analytical approaches for determining shear bond characteristics of FRP-concrete interfaces through pullout tests,” *Journal of Advanced Concrete Technology*, vol. 4, no. 1, pp. 133–145, 2006.